Experimental and Numerical Study of Ductile Metal Auxetic Tubular Structures

Muhammad Ali

Thesis submitted to the faculty of Virginia Polytechnic Institute and State University

in partial fulfillment of the requirements for the degree of

Master of Science

in

Civil Engineering

Eric Jacques

Matthew R. Eatherton

Ioannis Koutromanos

May 20, 2020

Blacksburg, Virginia

Keywords: Auxetic, Ductile Metal, Tubular, Steel, Aluminum, Energy Dissipation, Energy Absorption

Experimental and Numerical Study of Ductile Metal Auxetic Tubular Structures

Muhammad Ali

ABSTRACT

Methods to mitigate the risk posed by seismic and blast loads to structures are of high interest to researchers. Auxetic structures are a new class of metamaterials that exhibit counterintuitive negative Poisson's ratio (NPR) behavior based on their geometric configuration. Cellular auxetics are light-weight and cost-effective materials that have the potential to demonstrate high strength and resilience under axial forces. Existing research on metallic auxetics is scarce and based mostly on analytical studies. Apparent NPR behavior of auxetics has also been linked to enhanced energy absorbing potential. A pilot study was undertaken to investigate and understand auxetic behavior in tubes constructed using ductile metals commonly found in structural applications i.e. steel and aluminum. The main objective was to establish whether performance enhancements could be obtained through auxetic behavior in ductile metal tubes. In addition, any potential benefits to auxetic performance due to base material plasticity were studied. These objectives were fulfilled by conducting an experimental and analytical investigation, the results of which are presented in this thesis.

The experimental program consisted of establishing a design methodology, manufacturing, and laboratory testing for tubular metallic specimens. A total of eight specimens were designed and manufactured comprising five steel and three aluminum. For each base metal, three different geometric configurations of cells were designed: one with a rectangular array of circular voids and two with void geometries based on the collapsed shape of circular cells in a design tube under uniaxial compressive stress. A parameter called the Deformation Ratio (DR) was introduced to quantify cell geometry. Designed tubes were manufactured via a six-axis laser cutting process. A custom-made test assembly was constructed and specimens were tested under reverse-cyclic uniaxial loading, with one exception. Digital Image Correlation (DIC) was used to acquire experimental strain data. The performance of the auxetic and non-auxetic tubular structures was

evaluated based on the axial load-deformation characteristics, global deformations, and the specific energy absorption of the test specimens.

The experimental test results confirmed that ductile metal tubes with special collapsed cell geometries were capable of demonstrating auxetic behavior under the applied elastic and inelastic uniaxial strains; both tensile and compressive. Base material plasticity was observed to have an insignificant effect on the auxetic response. Experimental results suggested that the unique deformation mechanism precipitated by the auxetic cell geometries resulted in more stable deformed shapes. Stability in global deformed shapes was observed to increase with an increase in DR value. In addition, the unique auxetic mechanism demonstrated an ability to distribute radial plastic strains uniformly over the height of the auxetic pattern. As a result, plastic strains were experienced by a greater fraction of auxetic tubes; this enhanced the energy-dissipating properties of auxetic specimens in comparison to the tested non-auxetic tubes. Tubes with cell geometries associated with higher DR values exhibited greater energy absorption relative to the non-auxetic specimen. For the same base metal, auxetic specimens exhibited greater axial strength and effective strain range, when compared to their non-auxetic counterparts. The increased strength was partially attributed to the increased cell wall thickness of the auxetic specimens. However, the increased strain range was attributed to the rotation in unit cells induced by the unique auxetic geometry.

Experimental test data was used to validate the finite element (FE) and simplified macromechanical modeling approaches. These methods were adopted to develop design tools capable of replicating material performance and behavior as well as accurately predicting failure loads. Load-deformation response and effective Poisson's ratio behavior was established using FE models of as-built specimens, while simplified macromechanical equations were derived based on the equilibrium of forces to compute failure loads in tension. These equations relied on pattern geometry and measured experimental unit cell deformations. It was established that the manufacturing process had a detrimental effect on the properties of the aluminum specimens. Accordingly, empirical modifications were applied to the aluminum material model to capture this effect. FE models accurately replicated load-deformation behavior for both non-auxetic and auxetic specimens. Hence, the FE modeling approach was shown to be an effective tool for predicting material properties and response in ductile metal tubes without the need for

experimental testing. The simplified strength equations also described material failure with reasonable accuracy, supporting their implementation as effective design tools to gauge tube strength. It is recommended that FE models be refined further through the addition of failure criteria and damage accumulation in material models.

The result of this study established that auxetic behavior could be induced in ductile metal tubes through the introduction of unique cell geometry, thereby making them highly tunable and capable of exhibiting variable mechanical properties. Owing to their deformation mechanism and NPR behavior, auxetic tubes demonstrated geometric stability at greater deformations, which highlighted their potential for use as structural elements in systems designed to deform while bearing extreme loads e.g. earthquakes and blast events. Additionally, the capability of auxetic geometries to distribute strains uniformly along their length was linked to the potential development of energy-dissipating structural components. It was suggested that new knowledge acquired in this study about auxetic behavior in ductile metals could support the development of new structural systems or methods of structural control based on NPR behavior. Finally, recommendations for future research were presented, based on the expansion of research to study the effects of multiple loading regimes and parametric changes on auxeticity as well as additional mechanical characteristics e.g. shear resistance.

Experimental and Numerical Study of Ductile Metal Auxetic Tubular Structures

Muhammad Ali

GENERAL AUDIENCE ABSTRACT

Special structures known as Auxetics have been studied that exhibit counterintuitive behavior based on their geometric configuration. The novel shapes and architecture of these structures allow them to deform such that they expand laterally in tension and contract laterally in compression; a property known as negative Poisson's ratio (NPR) which is rarely observed in naturally-occurring materials. Auxetic materials demonstrate mechanical properties such as high resilience, indentation resistance, and energy-absorption. An experimental and analytical study was undertaken to explore the beneficial properties of auxetic behavior, along with the effect of inelastic deformations in ductile metal auxetics. To this end, tubular test specimens, made with steel and aluminum, were designed and manufactured. To achieve auxetic behavior, a unique array of collapsed cells was cut out from metal tubes using a laser cutting process. Subsequently, specimens were tested in the laboratory under cyclic and monotonic loads. Experimental results indicate that tubes with auxetic geometries exhibited NPR behavior and a unique deformation mechanism based on the rotation of the unit cells. Owing to this mechanism, auxetic specimens possessed greater geometric stability under applied axial deformations, when compared to the tested non-auxetic specimens. The deformation mechanism was also responsible for a uniform distribution of strains along the length of the auxetic geometry which was linked to relatively better energy absorbing capacity than the non-auxetic tubes. Developed finite element (FE) models captured the response and behavior of all specimens with good accuracy. Derived simplified strength equations were also able to calculate the ultimate tensile failure loads for all specimens accurately. Both numerical methods demonstrated the potential to be utilized as design and evaluation tools for predicting material properties. Finally, recommendations to expand research, based on metal auxetic structures, were presented to further our understanding of auxetic behavior in ductile metals and to explore its benefits under varying loading regimes. Results from this research can be used to support the design of new structural systems or methods to control existing structures by exploiting NPR properties of ductile metal auxetics. Furthermore, energy-dissipating

properties of metal auxetic materials may prove to be beneficial for structural applications under extreme loading conditions such as earthquakes and blasts.

Acknowledgments

I extend my deepest gratitude to my advisor Dr. Eric Jacques for his guidance, patience and constructive criticism throughout the course of this research. Using his invaluable experience and knowledge, he has helped me become a better thinker, writer and researcher.

To all my teachers at the University, I owe great thanks for imparting their knowledge to me. Special thanks to the wonderful staff at Patton Hall who made this experience so enjoyable.

I wish to thank the staff at the Murray Structures Lab for their help with experimental testing. I also extend my gratitude to Samuel Sherry for his continuous help and guidance with the use of the Digital Image Correlation (DIC) equipment.

I am deeply grateful to the Advanced Research Computing (ARC) division of Virginia Tech. for their help in conducting simulations.

Finally, I would like to thank my parents for their undying love, encouragement and support. This would not have been possible without their patience and sacrifice. To them, I dedicate this thesis.

Table of Contents

List of Figures

List of Tables

Notations and Symbols

Acronym		Definition
2D	=	Two-Dimensional
3D	=	Three-Dimensional
ASEA	=	Areal Specific Energy Absorption
DIC	=	Digital Image Correlation
DR	=	Deformation Ratio
EBM	=	Electron Beam Melting
FE	=	Finite Element
HAZ	=	Heat Affected Zone
MSEA	=	Mass Specific Energy Absorption
NPR	=	Negative Poisson's Ratio
PPR	=	Positive Poisson's Ratio
PR	=	Poisson's Ratio
PSF	=	Pattern Scale Facto
PTFE	=	Polytetrafluoroethylene
SEBM	=	Selective Electron Beam Melting
UHMWPE	=	Ultra-High Molecular Weight Polyethylene

Symbol	Definition
A_0	Effective Cross-sectional Area
C	Kinematic Hardening Modulus
C_g	Geometric Centroid
D_0	Tube Outside Diameter
DR	Deformation Ratio in %
E	Elastic Modulus
EA	Energy Absorption
G	Shear Modulus
H	Manufactured Tube Height
H_G	Tube Gauge Height
h_L	Height of Cell Layer
M_1	Moment Capacity of Primary Hinges
M_2	Moment in Secondary Hinge
M_u	Ultimate Flexural Capacity
m_A	Areal Mass
n	Number of Cells in Horizontal Layer
R	Tube Outer Radius
T	Total Tensile Load Capacity of Tube
T_i	Vertical Axial Force in Unit Cell
T_e	Experimental Tensile Failure Load

T_p^{FEA}	Tensile Failure Load Prediction by Finite Element Analysis
T_p^{STR}	Tensile Failure Load Prediction by Strength Equation
T_u	Ultimate Tensile Capacity
t_w	Tube Wall Thickness
w_r	Cell Wall Width
α	Initial Angle of Incline with Vertical Axis
Δ_0	Expected Yield Displacement
ΔH_G	Change in Tube Gauge Height
Δh_L	Change in Layer Height
Δ_m	Expected Maximum Displacement
ΔR	Change in Tube Outer Radius
ΔX	Tube Deformation Along Axis X
ΔZ	Tube Deformation Along Axis Z
ε	Vertical Axial Strain in Unit Cell
ε_A	Average Vertical Strain
ε_{AL}	Layer Vertical Strain
ε_a	Axial Strain
ε_E	Engineering Strain
ε_R	Mid-height Radial Strain
ε_T	True Strain
ε_t	Transverse Strain
ε_u	Final Elongation
γ	Plasticity Factor
μ	Ductility
μ_ϕ	Curvature Ductility of Auxetic Cell Wall
v	Poisson's Ratio
v_{MH}	Mid-height Layer Poisson's Ratio
v_T	Tube Poisson's Ratio
φ	Tube Porosity
ϕ	Strength Modification Factor
ϕ_y	Yield Curvature
ρ	Material Bulk Density
σ_E	Engineering Strain
σ_T	True Strain
σ_u	Failure Stress
σ_y	Yield Stress
θ_c	Unit Cell Rotation
θ_c^{exp}	Experimental Angular Rotation of Unit Cell

Chapter 1. Introduction

1.1. General

Natural and man-made phenomenon such as earthquakes and blasts impart massive amounts of unwanted energy to civil infrastructure. Novel structural systems are therefore designed and implemented in an effort to maintain structural integrity and minimize damage caused by this sudden release of energy. A large fraction of energy-dissipation assemblies exploit the mechanical properties of structural metals to resist high loads while demonstrating sufficient deformation capacity. Seismic and blast energy is concentrated towards these sacrificial energy-dissipating elements that are designed to exhibit controlled failure in the form of a ductile mechanism.

Permanent energy-dissipating systems such as eccentrically (Popov and Engelhardt 1988) and concentrically (Khatib et al. 1988) braced frames are common in structural applications. New structural systems with replaceable elements known as "structural fuses" have also been designed and employed to dissipate energy under seismic loading (Shoeibi et al. 2017; Tehranizadeh 2001; Malakoutian et al. 2012). Systems such as steel plate shear walls (Roberts 1995), ring-shaped shear walls (Philips and Eatherton 2018) and butterfly-shaped hysteretic dampers (Farzampour and Eatherton 2019) have been shown to demonstrate energy dissipation capacity. All these systems take advantage of high Yield modulus (E), Shear modulus (G) and ductility (μ) of structural steels depending on the designed failure mode. The maximum attainable limits for these properties are dependent on molecular structure and have almost been achieved, therefore new ways to enhance mechanical behavior are needed while limiting the weight and size of structures.

Mechanical properties of an isotropic elastic solid are controlled by another dimensionless property known as the Poisson's ratio (v). Defined by the negative ratio between the transverse strain (lateral deformation) to the axial strain (longitudinal deformation), the value for v typically lies in the positive domain for most bulk materials. For instance, values lie between *0.27-0.30* for steel, *0.1-0.2* for concrete, while gases and cork have a Poisson's ratio of *0*. A mathematical definition for Poisson's ratio is as follows,

$$\nu = -\frac{\varepsilon_t}{\varepsilon_a} \tag{1}$$

where ε_t represents transverse strain and ε_a is the axial strain in the material.

While our intuitive understanding of deformation of a material under an axial stress state leads us to expect expansion in the direction perpendicular to the principal stress, there exists a special class of material that behaves counterintuitively by contracting in the transverse direction instead (Figure 1.1). These materials have a negative value for the Poisson's ratio and are known as "auxetics" (Evans 1991). Materials such as these fall under the class of "metamaterial", meaning that they possess properties not inherently found in the naturally-occurring constituent material (Kshetrimayum 2005). In the case of auxetics, these properties are engineered through a precise geometric arrangement at a smaller finite scale which results in an apparent negative Poisson's ratio (NPR) behavior in the global structure.

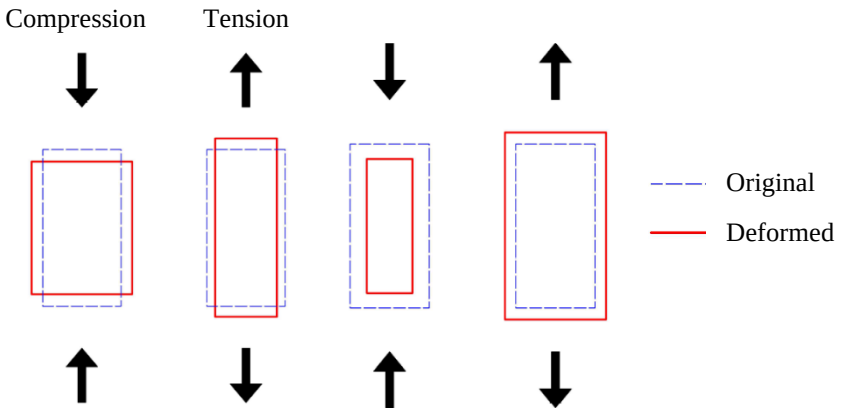

Figure 1.1: Deformation mechanisms for positive and negative Poisson's ratio materials.

The existence of auxetic materials does not contradict the classical theory of elasticity, which predicts possible Poisson's ratio as low as -1 and as high as $+0.5$ (Fung 1965). Auxetic behavior has been reported on the molecular level in crystalline solids such as iron pyrite monocrystals (Voigt 1882) and most cubic elemental metals (Baughman et al. 1998). Studies have also shown the presence of auxetic behavior in biomaterials such as cancellous bone (Williams and Lewis 1982), cat skin (Veronda and Westman 1970) and cow teat skin (Lees et al. 1991).

However, synthesized auxetics are of greater interest as their counterintuitive behavior provides a way to achieve enhancements in other mechanical properties not found in naturally-occurring materials. The theory of elasticity postulates that mechanical constants for an elastic material are interdependent. Consider the shear modulus $G = \mathrm{E}/2(1 + \mathrm{v})$, which is directly proportional to the ratio $1/(1 + v)$, meaning that, keeping the elasticity modulus (E) constant, a material engineered to exhibit a $v = -1$ could potentially demonstrate an infinite resistance to shear deformations. Out-of-plane deflection (Evans 1991), fracture toughness and indentation resistance (Figure 1.2) (Alderson et al. 1994) have been shown to be proportional to $(1 - v^2)$, which implies that negative values of v can lead to enhancements in these properties for isotropic materials. Lastly, enhanced volumetric strain energy dissipation is dependent on $(1 - 2v)$ (Alderson n.d.), hence enhancement can be achieved with negative values of Poisson's ratio. Currently, experimental research in auxetics is primarily focused on additively manufactured elastomeric cellular structures. However, a very limited body of knowledge in regards to ductile metal auxetics corroborates very beneficial properties such as energy absorption and dissipation (Lakes and Elms 1993; Qi et al. 2017; Imbalzano et al. 2018). Additionally, despite a reduction in mechanical properties such as strength and Young's modulus caused by removal of material to activate auxetic response, metallic auxetic structures have been shown to demonstrate higher specific (per weight) strength than their non-auxetic counterparts (Yang et al. 2012). Moreover, there also exists analytical evidence that suggests that auxeticity is present and even more pronounced when a material deforms in the plastic domain (Dirrenberger et al. 2012). Therefore, the use of ductile metals in auxetic structures could benefit from material non-linearity, enhancing energy absorption and dissipation characteristics, taking advantage of the enhanced deformation capacity in metals over higher strains. If proven to be practical and beneficial, auxetic materials could potentially replace conventional materials in structural applications.

However, there is effectively no research investigating potential structural applications of auxetics as load bearing or energy absorbing elements using typical structural materials. Large-scale testing of metal auxetics is also limited by the manufacturing processes employed e.g. Electron Beam Melting (EBM). However, established manufacturing techniques such as subtractive manufacturing offer a solution to the constraints in large scale production and can pave the way for the development and testing of auxetic elements.

Figure 1.2: Enhancement in Indentation Resistance with Negative Poisson's Ratio (Evans and Alderson 2000).

Auxetics also have a huge potential for use in other fields. They can offer ballistic protection in military and blast-safety applications. They can also be used in the medical industry as foldable stents and rings. They have tremendous potential for use in personal protective devices (Yang et al. 2018) owing to their lightweight nature and energy-absorbing capabilities. The physical and geometric properties of auxetics can be tuned for optimal performance as filters (Alderson et al. 2007; Rasburn et al. 2001). Shoe companies have employed auxetic patterns in their designs due to the thin-and-light nature of the product which also provides a higher degree of comfort (Ren et al. 2018).

The scarcity of auxetics research incorporating ductile metals leaves the field open for further research. Investigating the mechanical properties of metallic auxetic geometries could potentially pave the way for developing structures with superior mechanical properties by incorporating these special geometries. The optimization of auxetic geometries can lead to enhanced strength and efficient energy dissipation while maintaining and even reducing structural weight.

1.2. Research Objectives

The objective of this thesis is to study the performance of auxetic tubular structures fabricated from ductile metals to identify what performance enhancements in auxetic behavior could be obtained if the base material is permitted to yield and undergo plastic deformations. The objective is achieved by studying the behavior of steel and aluminum tubes containing auxetic topologies under uniaxial cyclic load reversals and comparing the results against tubes constructed

with non-auxetic topologies. The use of steel and aluminum were governed by the fact that these metals are commonly used in structural applications. The results will be used to quantify the effect of auxetic geometries on material performance as well as the effect of base metal plasticity on auxeticity. Data will be used to validate numerical and analytical models to predict load deformation response of auxetic and non-auxetic tubes.

1.2.1 Experimental Program

The experimental research involves the design, construction, and testing of a total of eight steel and aluminum tubes, with and without auxetic topologies, subjected to reversed cyclic uniaxial loading. The test series includes five steel tubes and three aluminum tubes constructed using one non-auxetic topology and two variations of auxetic topologies, derived using a cellular collapse design procedure. Two different base metals have been utilized in the study to study the dependence of auxetic behavior on base material properties.

1.2.2 Analytical Modeling

The analytical modeling involves finite element and simplified micromechanical modeling aimed at predicting the response of the auxetic and non-auxetic topologies studied during the experimental phase. This is achieved by generating hysteretic load-deformation predictions for auxetic and non-auxetic tubes using finite element analysis and the development of simplified macro-mechanical models to predict the ultimate strength of the tubes.

1.3. Thesis Organization

This thesis consists of six primary chapters, summarized in Figure 1.3:

- Chapter 1 introduces the objective of the research and presents a literature review on auxetic structures. Some potential applications of metal auxetics are also presented;
- Chapter 2 summarizes the details of the experimental program, including design of the auxetic topologies, specimen fabrication, material properties, instrumentation, and test procedure;
- Chapter 3 presents the experimental results for the eight ductile metal auxetic and non-auxetic tubes tested in the experimental program;

- Chapter 4 discusses and evaluates the experimental results to examine the influence of auxeticity on performance and material nonlinearity on auxetic response;
- Chapter 5 presents two analytical studies aimed at predicted the load-deformation response of the tube specimens under uniaxial loads. Test results are compared against predictions generated using finite element analyses and simplified analysis techniques, alongside a discussion on variation between the results;
- Chapter 6 concludes the thesis with a summary of the research and its' key findings, as well as providing some recommendations for future research directions.

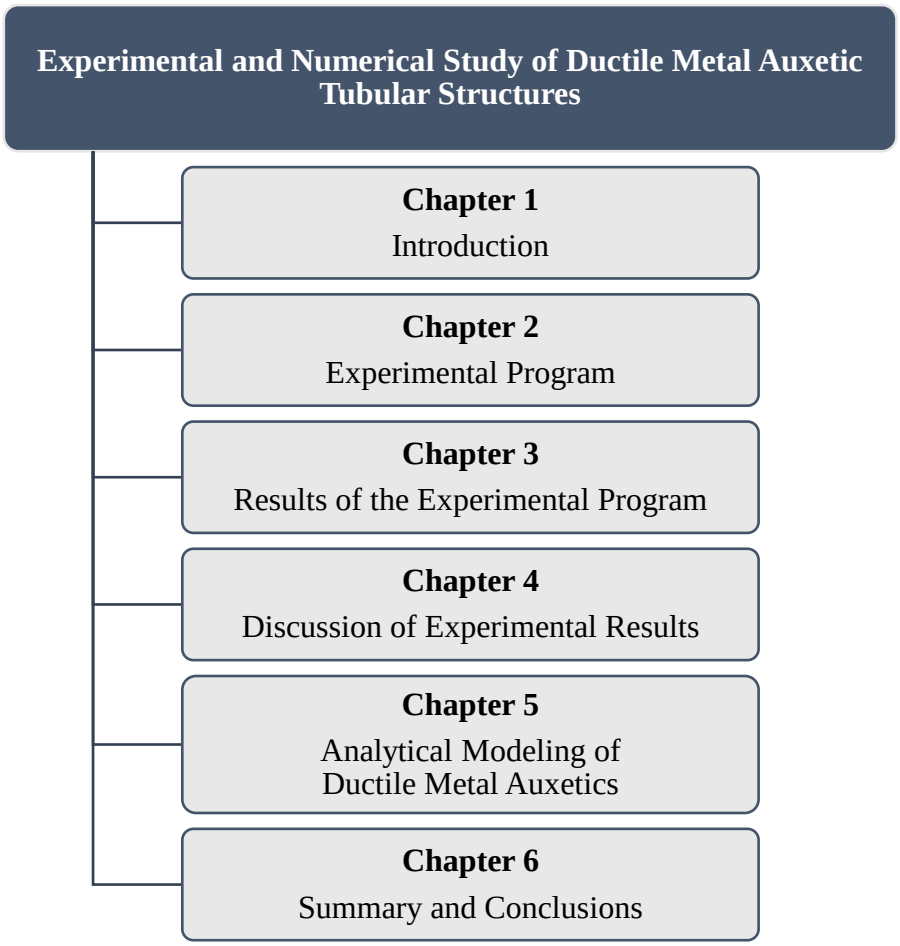

Figure 1.3: Thesis outline.

1.4. Literature Review

A comprehensive review of auxetics is presented below, based on cellular models and geometries. Naturally occurring auxetics are discussed followed by a detailed summary of literature involving auxetic materials and structures. Metallic auxetic structures are discussed. Properties of auxetics are illustrated in detail before shedding light on their potential and current applications as presented in literature. Lastly, the advantages, disadvantages and challenges identified are presented to describe the state-of-the-art in the manufacture and implementation of ductile metal auxetics.

Materials that behave counterintuitively under applied force have been known to exist naturally since 1944 when A. E. H Love described the atypical behavior of naturally occurring Iron Pyrites to expand axially under tension and contract in compression (Love 1944). Li reported that anisotropic single crystal Cadmium displayed this Negative Poisson Ratio (NPR) in some directions (Li 1976). These naturally occurring materials had this innate property owing to their molecular structure.

Lakes was the first researcher to study the effect of geometry on the Poisson ratio of a material (Lakes 1987). Lakes described a manufacturing process to create a re-entrant foam structure that exhibited negative v values. The procedure involved the use of conventional open-cell polymer foam cuboids, compressed sequentially in each of the three orthogonal directions while being heated to maintain a permanent inward protrusion (re-entrant geometry) of cell ribs. Figure 1.4 shows an idealized re-entrant unit cell produced during the conversion. The resulting re-entrant foams were more resilient in all three orthogonal directions than the conventional foams. The stress-strain behavior was linear up to *40%* strain without abrupt collapse. Reticulated metal foams were prepared by inducing permanent plastic deformations in all orthogonal directions also displayed the re-entrant geometry.

In his pioneering work, Lakes also predicted, theoretically, that this NPR behavior in re-entrant foams would be scale-independent and would result in a material with high indentation resistance, high toughness and synclastic curvature (Lakes 1987).

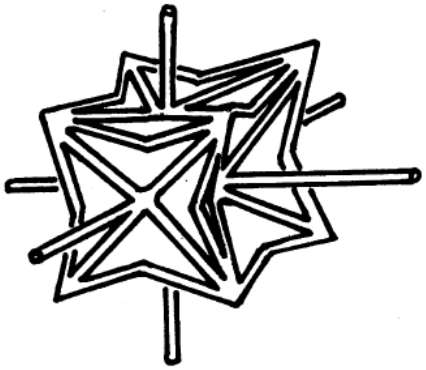

Figure 1.4: Idealized re-entrant unit cell for the collapsed open cell foam (Lakes 1987).

The term 'auxetic' materials was first proposed by in his work on auxetic polymers in which a commercially available form of polytetrafluoroethlene (PTFE) with large NPR value was studied (Evans 1991). The microstructure of the PTFE consisted of a network of fibrils connected to nodules. These fibrils would become taught when a tensile force was applied, pushing the nodules apart and showing auxetic behavior. Though highly anisotropic, NPR values as high as -*12* were recorded.

Over the years, auxetic materials have been proposed and created that make use of unique deformation mechanisms and geometric configurations. These materials can be categorized based on their geometries, parent constitutive materials and dominant deformation mechanisms that generate the auxetic effect.

1.4.1 Naturally Occurring Auxetics

Auxetic materials have been known to exist naturally since as early as 1882 when iron pyrite monocrystal was reported to have negative Poisson's ratio by Voigt (1882). This behavior was reported while conducting experiments on the twisting and bending behavior of mineral rods. Love (1944) corroborated Voigt's findings by proving the existence of iron pyrite monocrystal and estimated a Poisson's ratio value of $-\frac{1}{7}$.

Baughman et al. (1998) presented that NPR behavior is surprisingly common in cubic metals, with *69%* of cubic elemental metals exhibiting a NPR when pulled along the direction shown in Figure 1.5 (a).

Williams and Lewis (1982) investigated the source of anisotropic properties of cancellous bone in the proximal epiphysis of the human tibia (Figure 1.5 (b) shows tested sample). Compression testing showed the presence of NPR.

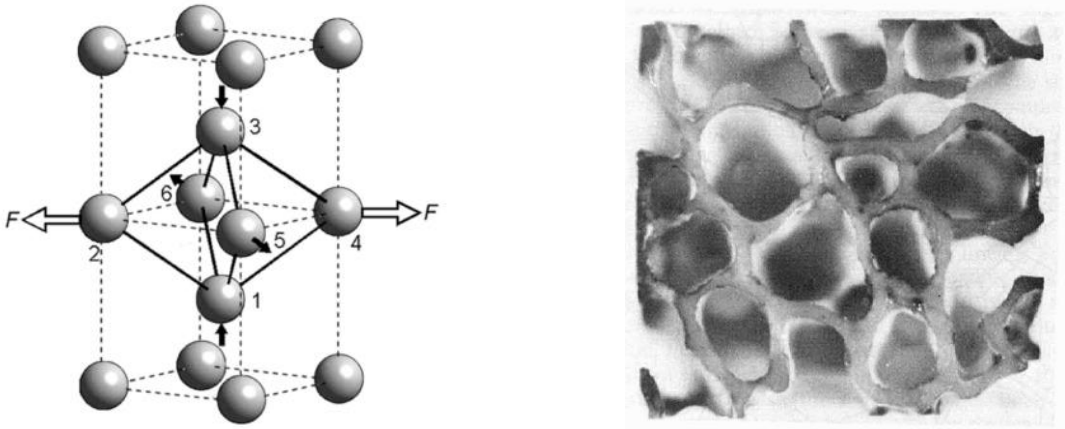

a) b)

Figure 1.5: a) Structural origin of negative Poisson's ratio in rigid-sphere body-centered cubic solid (Baughman et al. 1998); b) Transverse surface of samples cut from proximal epiphysis of the human tibia (Williams and Lewis 1982).

Veronda and Westman (1970) carried out the mechanical characterization of cat skin (shown in Figure 1.6) and found out that the cat skin was auxetic at limited deformations. Cow teat skin was also shown to exhibit NPR by Lees et al. (1991).

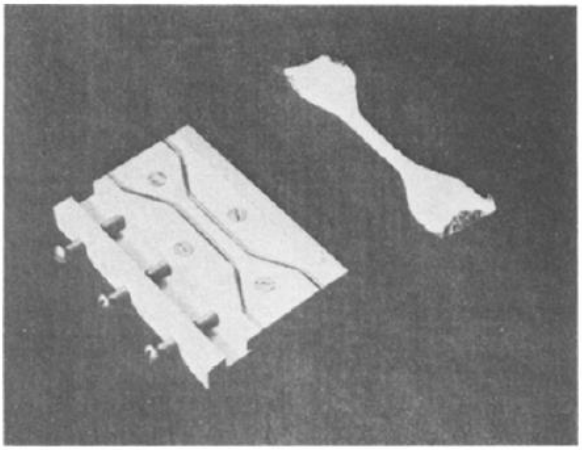

Figure 1.6: Cat skin sample and cutter (Veronda and Westman 1970).

1.4.2 Mechanical Models for Auxetic Materials

Re-entrant Open-Cell

Almgren initially presented a three-dimensional isotropic structure (shown in Figure 1.7) with rigid rods and elastic hinges connected in a re-entrant fashion (Almgren 1985). Appropriate changes to the basic 2-D re-entrant geometry were made to achieve a Poisson's ratio of *-1* and an infinite shear modulus.

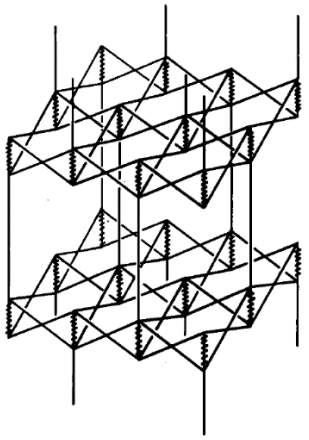

Figure 1.7: 3D auxetic structure with $v = -1$ (Almgren 1985).

Masters and Evans analytically modelled the auxetic behavior of a conventional 2D re-entrant honeycomb structure which is an array of re-entrant structures proposed by Gibson and Ashby (1999) with deformations resulting from axial deformation, flexure and hinging of the cell ribs (Masters and Evans 1996). The auxetic behavior of the honeycomb was dependent on the angle θ, where a negative value results in a conventional honeycomb while an auxetic honeycomb possessed a positive θ. Parametric analysis was conducted to study the effects of the change in rib angle θ, horizontal strut length *h* and vertical strut length *l*, as shown in Figure 1.8 (a). A maximum theoretical NPR of *-1* was deemed possible for the highly anisotropic geometry. It is worth mentioning that Evans et al. (1991) also presented a similar structure.

Choi and Lakes used their proposed unit-cell geometry (see Figure 1.8 (b)) to model auxetic behavior in foams with re-entrant unit cells (Choi and Lakes 1995). Expressions for Poisson's ratio at small strain (elastic), large strain (post plastic hinging) and during elastic-plastic deformation were presented. Experimental results (Choi and Lakes 1992) using copper foam agreed with analytical modeling employing the proposed unit-cell geometry.

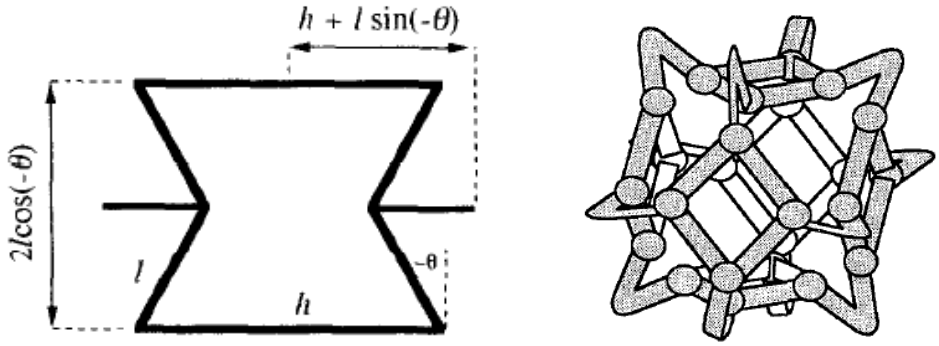

a) b)

Figure 1.8: a) Cell geometry for re-entrant cell (Masters and Evans 1996); b) Idealized re-entrant unit cell (Choi and Lakes 1995).

Rotating Polygons

Grima and Evans (2000) provided an early account of auxetic action as a consequence of the rotation of rigid squares hinged at their vertices. Figure 1.9 (a) shows the geometry employed to demonstrate the NPR behavior with a constant Poisson ratio value of $v = -1$ for the idealized structure.

Adding to their earlier contributions, Grima et al. (2007) examined auxetic behavior of semi-rigid rotating squares. An analytical model for stress-strain behavior, elastic moduli and Poisson's ratio was proposed. It was concluded that the semi-rigid nature of the squares produces $v > -1$, dependent on the ratio relative stiffness between the units and hinges, initial angle between squares and the direction of the applied loading.

Similarly, another case of auxetic deformation was examined by Grima et al. (2004), achieved through rotating rectangles. Equations describing the properties of the system were derived based on side lengths *a* and *b* as well as the angle θ between the rigid units, as shown in Figure 1.9 (b). It was suggested that a given structure could yield both positive and negative v values and therefore the Poisson ratio was strain-dependent.

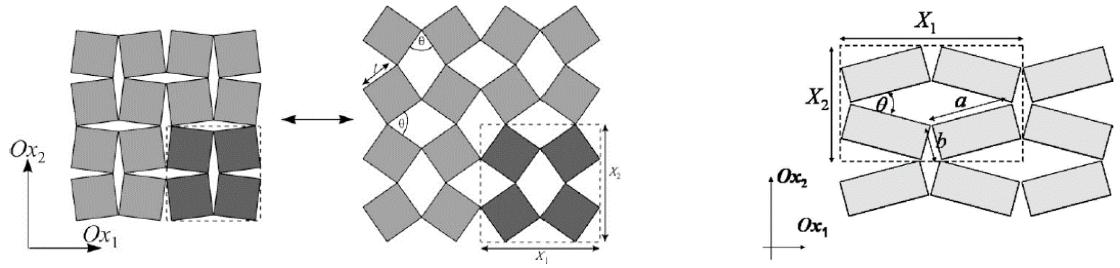

(a) b)

Figure 1.9: a) Geometry of auxetic "rotating squares" structure (Grima and Evans 2000); b) System of rotating rectangles with highlighted unit cell (Grima et al. 2004).

Grima et al. (2010) presented another variant (Figure 1.10) with a combination of squares and rectangles of different size. It was shown that scale-independent auxeticity can be exhibited in certain directions of loading, while Poisson's ratio is a function of the shape, size and relative angle between the constituent polygons.

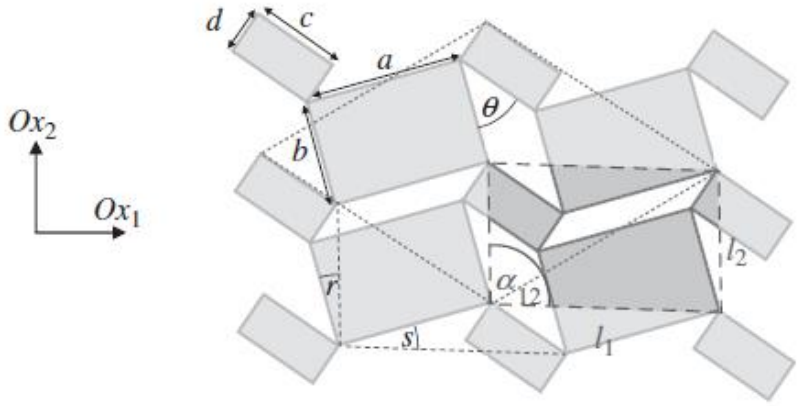

Figure 1.10: System of connected different-sized rectangles (Grima et al. 2010).

In addition to squares and rectangles, a research was extended to 2-D rigid parallelograms and rhombi by Grima et al. (2008). The geometries were divided into *6* distinct categories. Analysis showed that these geometries could exhibit both positive and negative Poisson's ratio with the value dependent upon the shape of the rhombi/parallelograms as well as the angles between each connected element. It was predicted that the Poisson ratio value for a rotating parallelogram reach $v = -30$, given the provided assumptions.

Rotating Triangles

Grima and Evans (2000) initially proposed that a structure with a network of hinging equilateral triangles could exhibit auxetic behavior. The hypothesis was validated via an analytical study conducted to derive the compliance matrix for this hinging triangle structure (Grima and Evans 2006). By idealizing the triangles as rigid bodies, the study showed that the structure would exhibit a constant Poisson's ration of -1, irrespective of the size of triangles used; demonstrating the scale-independent nature of the configuration. The authors also expressed that catering for deformations in the triangles would ultimately reduce the auxetic effect and allow shear deformations in the system.

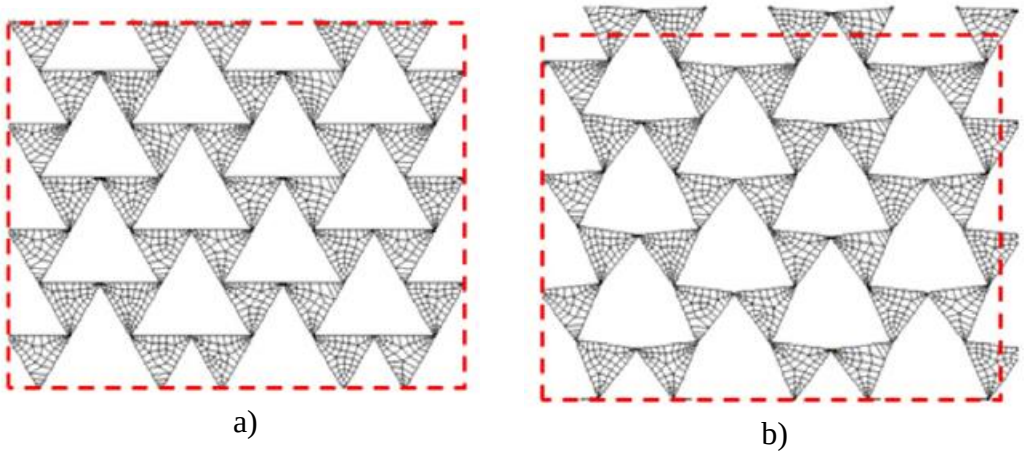

Figure 1.11: a) Undeformed geometry for rotating triangle model; b) Deformed geometry for rotating triangle model. (Grima and Gatt 2010).

FE simulations of sheets made with non-crystalline solids containing triangular and star-shaped perforations (Figure 1.11) were conducted by Grima and Gatt (2010). The study showed that such sheets were capable of auxetic behavior. The triangles were idealized as rotating rigid bodies. A parametric study was subsequently conducted to show that the effective Poisson's ratio could be tailored through altering the shape and density of the perforations in the sheets.

Another analytical study was conducted using rotating rigid scalene triangle (Grima et al. 2011). A Poisson's ratio of -1 was expressed by particular configurations. This generic model (Figure 1.12) also showed a dependency on the shapes and angles of the triangles, thus, was proposed as a way to describe auxeticity in many classes of materials.

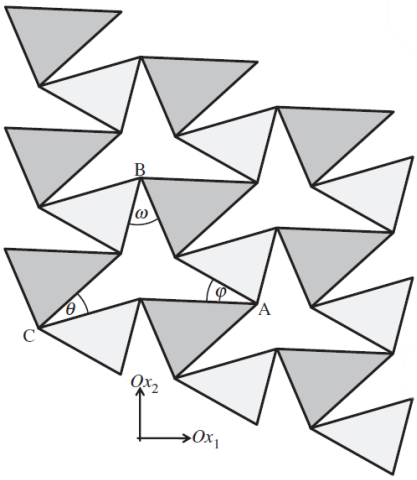

Figure 1.12: Auxetic generic rotating triangle model. (Grima et al. 2011).

To model deformations in auxetics foams more accurately, a model with semi-rigid triangles was proposed by Chetcuti et al. (2014) which allows for the relative rotation of the joints (hinges), different amount of material in the joints and deformations in the joints themselves. These added deformations were shown to reduce the amount of auxeticity, resulting in more dependable predictions for the properties of auxetic foams e.g. Poisson's ratio.

Missing Rib models

Smith et al. first proposed a missing rib model to determine elastic properties of elastic foams (Smith et al. 2000). It was named thus, as the idealized microstructure for the model was derived from a conventional structure with certain ribs removed (Figure 1.13). While the conventional shape had an in-plane positive Poisson's ratio, the missing rib configuration was auxetic. Expressions for the elastic moduli were derived for the geometry. Elastic angular deformation between ribs was the mode of deformation without a change in rib length allowed. True stress vs true strain behavior was predicted and results compared with experimental tests. It was concluded that the 2D hexagonal model proposed by Masters and Evans (1996) was invalid for describing the strain-dependent behavior of auxetic foams; i.e. the missing rib model was a good representative of the actual cell geometry.

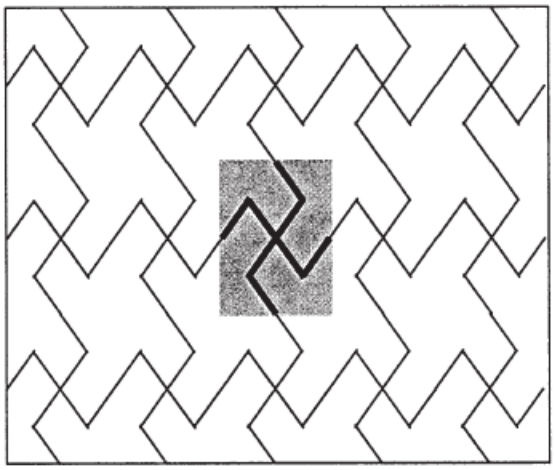

Figure 1.13: Missing rib model with highlighted unit cell (Smith et al. 2000).

This work was continued by Gaspar et al. (2005) who tested auxetic geometries shown in Figure 1.14. Experimental data was acquired and Poisson's ratio for the intact and missing rib geometries was plotted. The work confirmed the presence of auxetic behavior in missing rib structures.

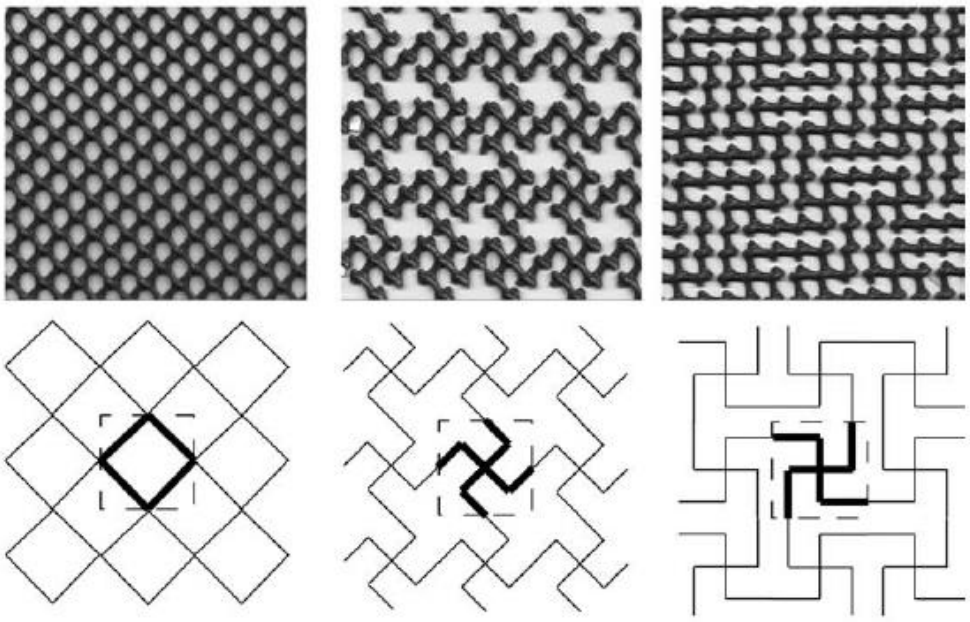

Figure 1.14: Conventional and missing rib geometries with corresponding unit cells (Gaspar et al. 2005).

After observing both conventional and auxetic foams under a microscope, Lim et al. (2013) concluded that the re-entrant structure commonly adopted for modeling auxetic structures was

incorrect. From the microscopic image, a new and highly-ordered model, based on a hexagonal structure with missing ribs was proposed. The proposed model was designed to conserve isotropic behavior and replicate the initially-observed internal geometry of reticulated foams.

Chiral and anti-chiral lattices:

The chiral lattice model represents another example of a geometry that induces auxetic behavior in a structure. Figure 1.15 shows a chiral unit cell comprises of a circular central rigid ring to which six tangential ligaments are attached in a pattern that maintains rotational symmetry (Spadoni and Ruzzene 2012). It is evident that an in-plane compressive force causes an anti-clockwise rotation of the central rings, causing the entire network to shrink inward; an auxetic response.

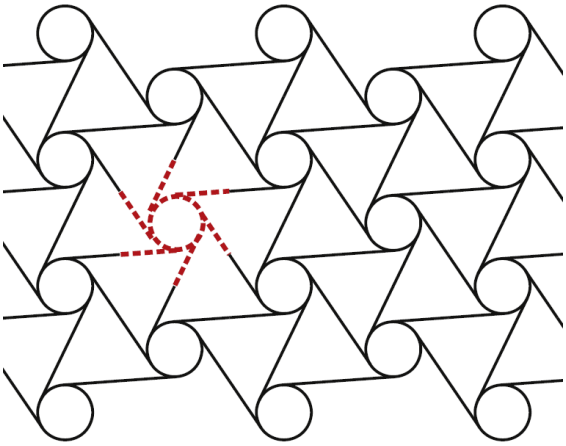

Figure 1.15: Hexagonal chiral lattice geometry with highlighted unit cell (Spadoni and Ruzzene 2012).

Lakes introduced this model as an anisotropic 'noncentrosymmetric' hexagonal structure that displays negative Poisson's ratio (Lakes 1991). The model had nodes capable of rotation about their central and flexible ligaments.

Prall and Lakes carried out an experimental and theoretical investigation of a 2D chiral honeycomb that has an in-plane Poisson's ratio $v = -1$ (Prall and Lakes 1997). In contrast to other materials of an auxetic nature, the NPR property could be sustained over a higher range of strain for chiral structures. An expression for the in-plane Young's modulus was derived based on the

Young's modulus of the bulk material. A similar expression was derived by Gibson and Ashby (1999).

Spadoni and Ruzzene (2012) used two separate models to establish constitutive relationships in chiral models with rigid and deformable nodes. An analytical approach was adopted for the rigid model while complexity in obtaining analytical expressions necessitated the use of and FE models to develop a correlation between strains states and the applied displacements/rotations. Expressions for Young's modulus, Poisson's ratio and shear modulus were presented as a result.

Using a similar approach, the auxetic properties of chiral and anti-chiral lattices like those shown in Figure 1.16 were studied (Alderson et al. 2010). Additionally, investigations for other chiral and anti-chiral models were performed (Grima et al. 2008; Alderson et al. 2010; Gatt et al. 2013).

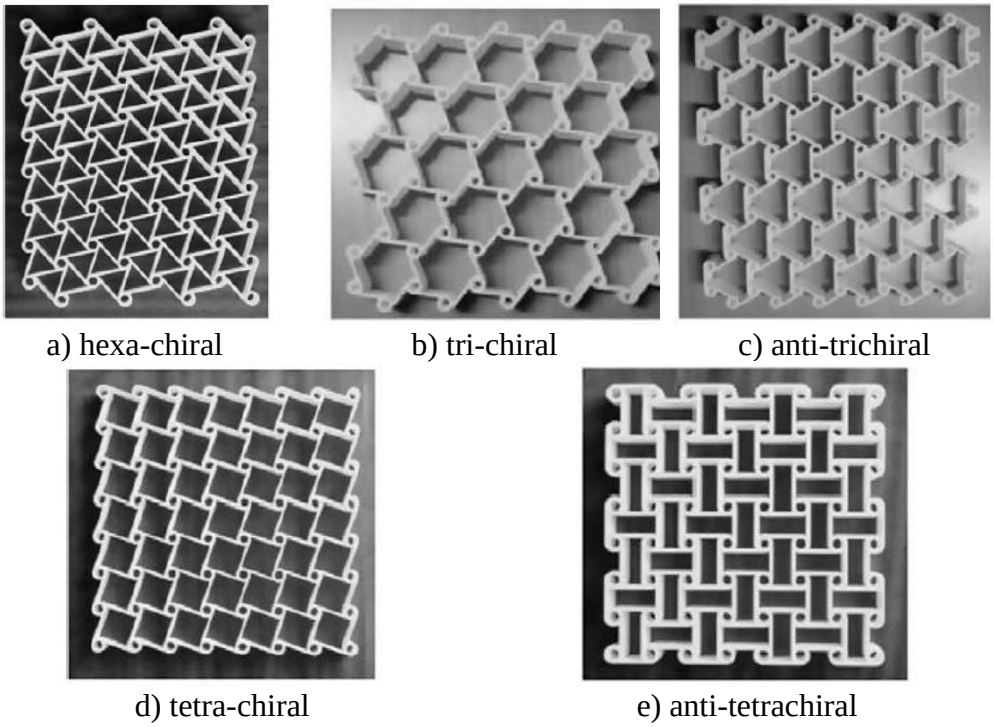

Figure 1.16: Rapid prototype honeycomb specimens (Alderson et al. 2010).

An auxetic anti-tetrachiral model was examined both analytically and using the finite element method by Chen et al. (2013). Results present that large variations in the in-plane NPR values can be expected by changing the length of ligaments in the orthogonal directions.

By using finite element simulation, Pozniak and Wojciechowski (2014) determined the Poisson's ratio of disordered anti-chiral structures assembled on rectangular lattices. A stochastic distribution of circular node radii was the source of disorder. The studied models were parameterized by circular radii, rib thickness, and lattice anisotrophy. Three approaches were employed for analysis: one representing the exact behavior of the system using triangular elements and the other two approximating behavior using Timohshenko beam elements. It was concluded that the structures could have NPR values lower than $v = -1$ with lower values corresponding to thin-walled elements. Additionally, it was noted that the use of Timoshenko beam elements is only valid for thin-walled elements.

Nodule-Fibril Microstructure

Alderson and Evans proposed a nodule-fibril microstructural model, focusing on fibril hinging, fibril flexure and fibril stretching induced deformations individually (Alderson and Evans 1995). Referring to Figure 1.17, the idealized nodule was rectangular in shape with length 'a' in the major axis and length 'b' in the minor axis. The fibril geometry is characterized by length 'l' and angle with the x-axis 'α'. A tensile stress results in fibril hinging, reducing angle 'α' thus, leading to auxetic behavior in the structure. Expressions for the Young's modulus and Poisson's ratio were obtained for all three deformation mechanisms.

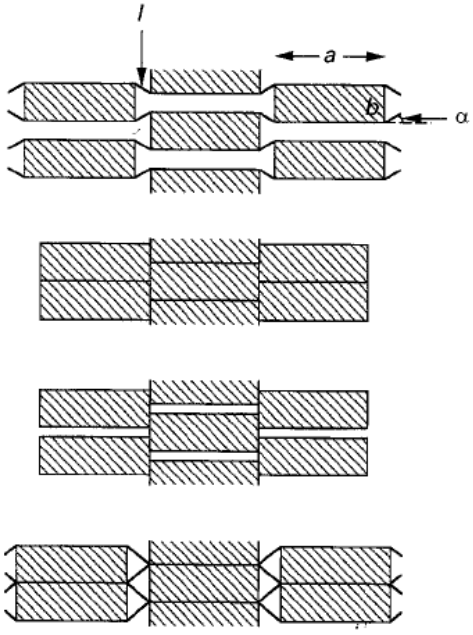

Figure 1.17: Schematic diagram for the Nodule Fibril model (Alderson and Evans 1995).

Experiments were carried out on microporous auxetic materials (Caddock and Evans 1988; Alderson and Evans 1993; Neale et al. 1993), composed of polytetrafluoroethylene (PTFE) and ultra-high molecular weight polyethylene (UHMWPE). Presented analytical expressions showed agreement with experimental results. Fibril stretching was found to be the dominant mechanism as angle 'α' approached a value of *0*. It was also found that calculated values for Young's modulus and Poisson's ratio using fibril flexure and hinging models gave the exact same values.

1.4.3 Auxetic Materials and Properties

Auxetic Foams

Conventionally, foams are known to exhibit positive Poisson ratio unless they are processed in a particular manner to impart auxetic properties to them. Lakes (1987) proposed such a conversion for convectional foams to auxetic foams via a process of heated triaxial compaction followed by cooling that resulted in a permanent inward (re-entrant) protrusion of the cell ribs. An optimum compression factor of *1.4-4* was found, for polyester foams to obtain an NPR. Reticulated ductile metal foams were also converted to auxetic foams via a process of plastic deformation in all three principal directions at room temperature. These auxetic foams were found to be more resilient than conventional foams. High material fracture toughness, synclastic curvature and indentation resistance for NPR materials was also predicted. The scale-independence of auxetic behavior in foams was also mentioned in this work.

An identical manufacturing process was employed in the work of Friis et al. (1988) to evaluate the mechanical and structural behavior of re-entrant foams composed of polymers and copper. Low volume fraction of materials was preferred such that buckling-induced deformations of the ribs may occur to produce the NPR effect. Mechanical testing showed that re-entrant foams had reduced elastic moduli than conventional foams but had a higher resilience. Plastic hinge formation as well as plastic buckling of ribs in the re-entrant copper foams were identified as the deformation mechanisms. Figure 1.18 show SEM images of conventional and re-entrant copper foam.

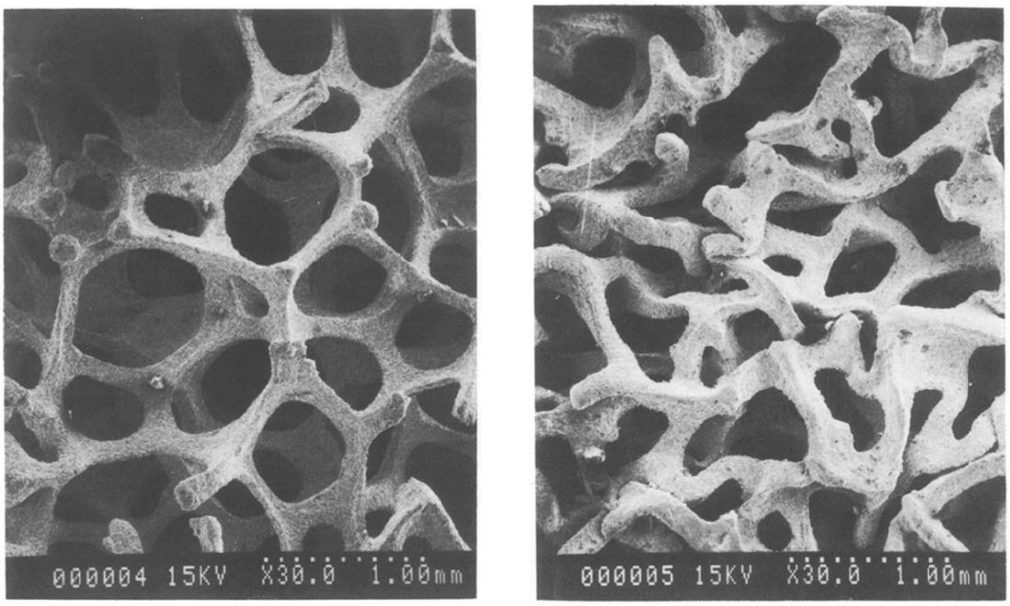

a) Conventional b) Re-entrant

Figure 1.18: Scanned electron micrographs of copper foam (Friis et al. 1988).

Choi and Lakes (1992) determined the non-linear stress-strain relationship for conventional and re-entrant polymeric foams i.e. Scott and Gray foam. This relationship was found to be reliant on the initial volumetric compression ratio for the re-entrant foams with an optimum compression ratio between *3.3-3.7.* The variation in Poisson's ratio with the strain was observed.

Results indicated NPR at small strains, high material toughness as well as resilience in the re-entrant arrangement. Folding and unfolding of cell-ribs was identified as the deformation mechanism for the auxetic foams.

Choi and Lakes (1992) also conducted a similar study focusing on re-entrant copper foams made through a series of uniaxial plastic deformations. Testing showed the strain-dependence of the Poisson's ratio for the material where the minimal value was obtained over a smaller range than the polymeric foams. A v value as small as *-0.8* was achieved for a near-zero strain value. Strain hardening behavior was absent in the re-entrant configuration. Despite the ductile nature of the constituent metal, a brittle failure was observed. The re-entrant foam showed increased toughness. Higher elastic moduli than conventional foam was recorded with an increase compressive strength but a reduced tension strength owing to the formation of plastic hinges from the initial compressive deformations.

Choi and Lakes (1995) also conducted an analytical study on the stiffness of open-cell solids; conventional and re-entrant NPR foams. They idealized the unit cell as a regular tetrakaidekahedron (14-sided polygon) for conventional foams (see Figure 1.8 (b)) where kinks added inwards in the ribs gave rise to the NPR in the re-entrant model. Analytical predictions were in agreement with experimental results mentioned in their previous research. Re-entrant foams were predicted to have a linear elastic behavior over a larger range than conventional foams. A change to a concave geometry from a convex one was credited for the differences in mechanical behavior between conventional and re-entrant foams.

Chan and Evans (1998) studied indentation properties of conventional and re-entrant polyurethane foams. Ball and cylinder indentation tests were carried out on 10ppi and 30ppi polyether urethane foams with both conventional and re-entrant structure. Results showed an increase in indentation resistance with the decrease in the Poisson ratio value (more negative value) for re-entrant foams, demonstrating the importance of and NPR value in increasing resilience. A more extensive area of indentation for the re-entrant geometry was observed, implying a lower value of shear strain in auxetic foams.

Auxetic Composite Sandwich Panels

Yang et al. (2013) studied various sandwich panel structures fabricated in a titanium alloy through the electron beam melting (EBM) process. Specimens, show in in Figure 1.19 were subjected to bending tests to characterize their mechanical characteristics. Different failure mechanisms for the sandwich panels were observed. Auxetic sandwich structures displayed a more uniform distribution of deflections and stresses. Auxetic panels demonstrated higher overall structural ductility and high resilience to bending. In terms of energy absorption, for a similar peak response force, the auxetic design absorbed approximately *100%* more energy than its counterparts. Similarly, for the same energy absorption level, the auxetic structures had a considerably smaller reaction force than the other designs.

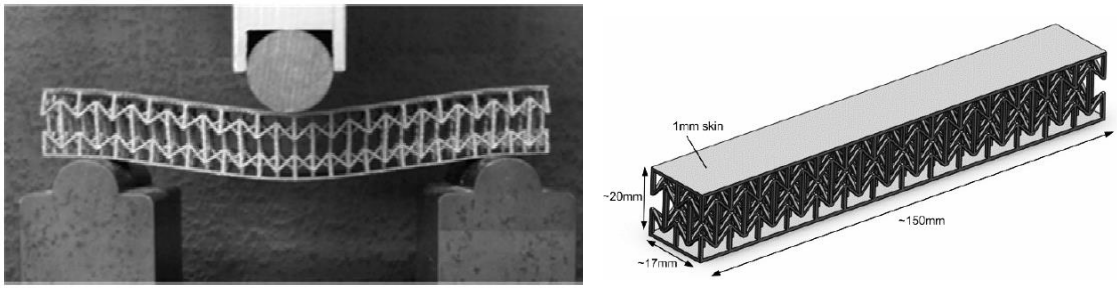

a) Specimen under bending b) FEA model of specimen

Figure 1.19: Titanium auxetic core sandwich panel (Yang et al. 2013).

Yang et al. (2013) carried out a numerical and experimental study concerning the ballistic resistance of sandwich panels with aluminum foam and auxetic honeycomb cores. Sandwich panels with aluminum face sheets and cellular cores of varying thicknesses and densities, respectively, were modeled using LS-DYNA (LSTC 2018) and impacted with a hemispherical-nosed cylindrical projectile. Figure 1.20 (a) shows an FE model used for simulations. Foam-cored FE models were validated using results from literature while quasi-static tests (Figure 1.20 (b)) were conducted to validate the auxetic core panel models. Validated models were tested against projectile at multiple impact velocities. Auxetic honeycomb cored showed higher energy absorption. Furthermore, the auxetic configuration did not show any energy enhancement with increasing projectile velocities, rather energy absorbed decreased as the velocities were increased. Additionally, the auxetic panels showed a larger effected area, larger tunnel diameters and substantially lower residual velocities which led to a larger delamination area of the back face. Higher core densities were shown to have a greater impact on the ballistic limits of the auxetic panels.

Imblazano et al. (2016) presented a numerical study about auxetic composite panels under blast loading. The performance of sandwich panels with auxetic cellular cores and metal facets (Figure 1.20 (a)) was studied numerically under impulsive loading and rate-dependent effects were accounted for. To evaluate the performance of different design, parameters were varied in the FE models and results compared to an equivalent monolithic panel. Effects of a change in core material were also studied. Under blast loading, the auxetic core resulted in enhanced performance with reduced back facet displacement, velocity and plastic dissipated energy when compared to the monolithic panels. The change in core material did not have any significant effects on the panel performance against blast loading.

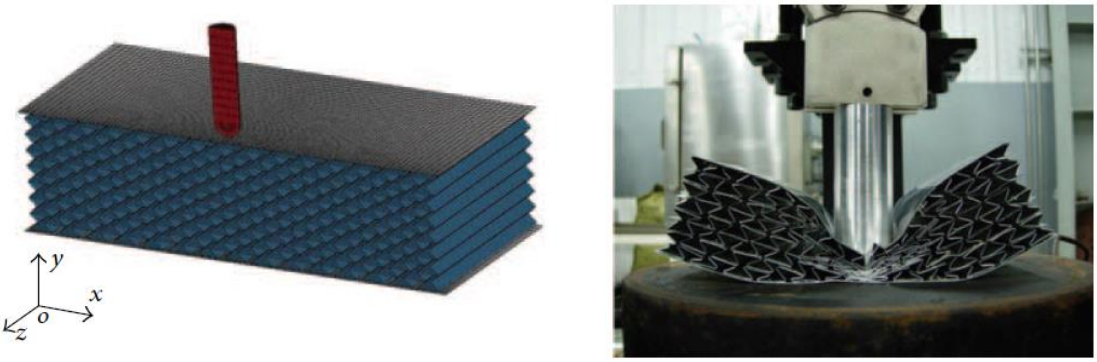

a) FE model of sandwich panel and projectile b) Quasi-static test

Figure 1.20: Ballistic resistance testing of auxetic honeycomb core sandwich panels (Yang et al. 2013).

Imbalzano et al. (2018) compared the performance of honeycomb and auxetic cores in sandwich panels in another numerical study. The dynamic behaviors of these panels were investigated and the effects of parametric changes to effective Poisson's ratio, transmitted forces and peak stresses were recorded to quantify performance. Numerical analysis showed that the auxetic material exhibits a material densification effect under impulse loading; the back-face reaction forces showed gradual increase with core crushing. For a similar reaction force, the auxetic panels developed a lower back-face stress due to densification; the larger the value of effective Poisson's ratio, the lower the back-face stress. The study indicated that increasing the layers of cells for the auxetic panel directly increased the overall energy dissipation while decreasing the back-face stresses.

Qi et al. (2017) studied the shock mitigation properties of auxetic honeycomb-cored sandwich panels against close-in and contact detonations. Field blast tests, drop weight tests and numerical FE modeling was carried out to quantify the blast-resistance of the panels compared to conventional steel protective plates. Tested specimens and assemblies are shown in Figure 1.21. Drop weight impact tests showed more impact force and higher energy absorption for the auxetic design. A material concentration effect was observed in both simulations and experiments which led to a higher load level and uniform load distribution. Blast tests and simulations using the close-in detonation of a cylindrical charge showed a significantly high energy absorption in the cover plate and core for the auxetic panel than the reference steel plate, which resulted in no damage to the shielded concrete panel. Even though both conventional and auxetic cores enhanced the energy absorption capabilities of the protective panel, the auxetic design absorbed *19.1%* more energy

than its conventional counterpart. The auxetic configuration also showed higher areal specific energy absorption (ASEA) which was defined as follows:

$$ASEA = \frac{EA}{m_A} \qquad (2)$$

where m_A was the areal mass of the protective structure and EA was the blast energy absorption.

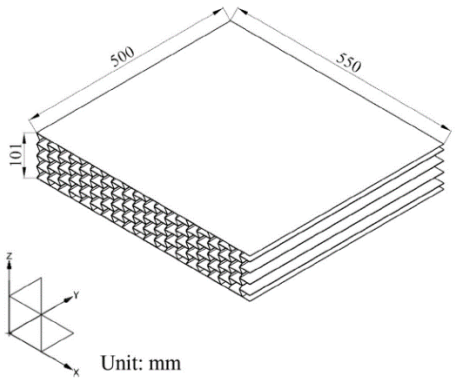

a) Geometry and dimensions

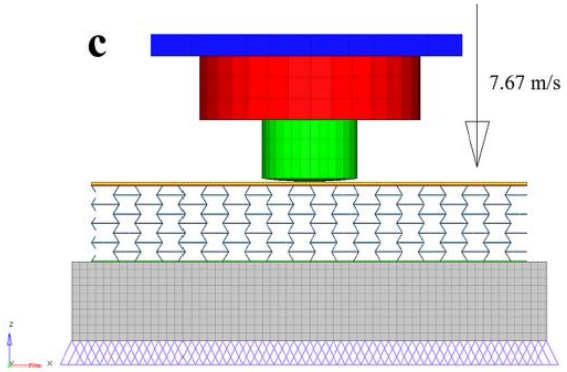

b) FE model of drop weight impact test

c) Field blast test set-up

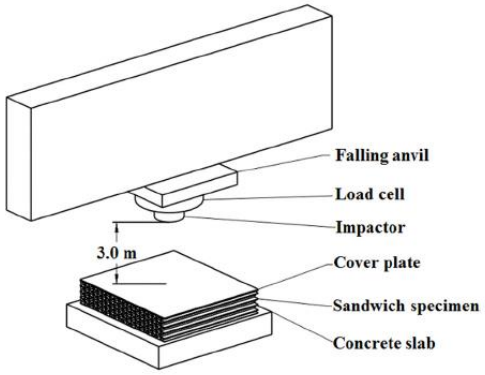

d) Drop weight impact test set-up

Figure 1.21: Auxetic core sandwich panel specimens and assemblies (Qi et al. 2017).

Periodic Auxetic Structures

Compliant mechanisms

Compliant mechanisms take advantage of localized elastic deformations to transfer either loads or deformations from one point in a structure to another. 3D compliant porous structures were designed and analyzed analytically and numerically using finite elements (Kim and Ju 2015). The proposed compliant cellular material showed extremely high and low Poisson's ratios (± 30).

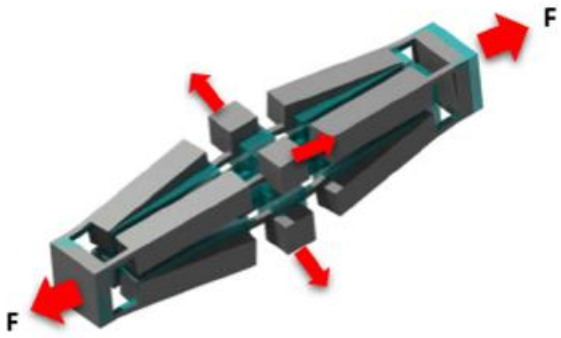

Figure 1.22: 3D auxetic compliant porous structure (Kim and Ju 2015).

Other studies focused on the design of auxetic compliant materials via topology optimization with different approaches. Auxetic compliant mechanisms were designed using evolutionary-hybrid algorithms (Kaminakis and Stavroulakis 2012), micropolar material models (Bruggi et al. 2016) and polygonal finite elements (De Lima and Paulino 2019).

Low Porosity periodic structures

Grima and Gatt (2010) showed numerically that sheets made with conventional isotropic rubber materials containing diamond or star shaped perforations (shown in Figure 1.23 (a)) displayed negative Poisson's ratio in both tension and compression. A model was created based on rotating rigid units to describe the deformation mechanism. However, the model only holds true for small strains. The effect was stated to be scale-independent.

An experimental and numerical analysis of the perforation geometries in 2D metal sheets was conducted by Taylor et al. (2013). A decreasing value for Poisson's ratio was observed with an increase in the aspect ratio of an alternating pattern of perforations (samples shown in Figure 1.23 (b)). Experiments were carried out using thin aluminum plates. An agreement between

experimental and numerical results was seen. The authors concluded that the effective Poisson's ratio can be tuned by adjusting the aspect ratio of the alternating pattern of elliptical voids.

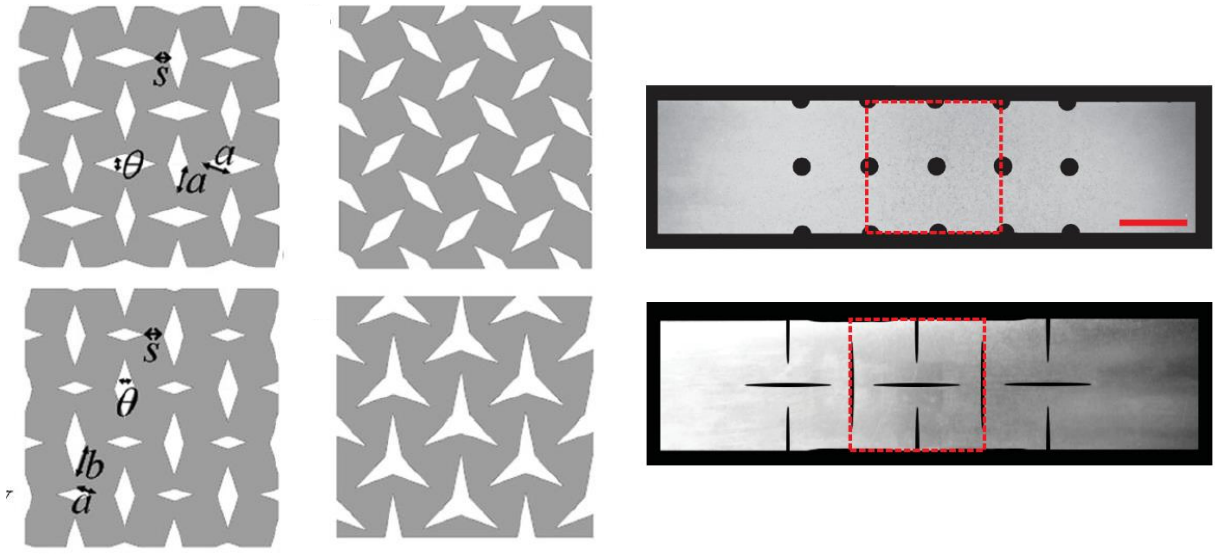

a) b)

Figure 1.23: a) Examples of perforated sheets with NPR behavior (Grima and Gatt 2010); b) Aluminium samples with arrays of circular and elliptical perforations (Taylor et al. 2013).

The effects of an introduction of slit perforations into a sheet material were studied by Mizzi et al. (2015). Multiple slit geometries were designed and analyzed using FE models using an elastomeric material. Results show that all simulated systems exhibited auxetic behavior with some systems exhibiting large NPR values lower than *-4*.

A similar 2D porous material was proposed by Carta et al. (2016) with a hexagonal periodic distribution of slits as shown in Figure 1.24. Both experimental and numerical tests were performed to quantify auxetic performance. Additionally, a parametric study on the effect of geometrical changes to the perforations was presented. The structure possessed isotropic auxetic behavior which was determined to be scale-independent.

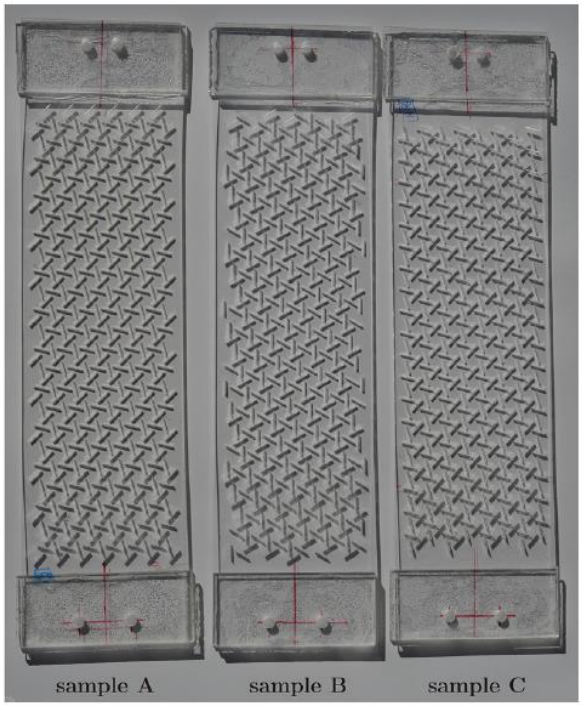

Figure 1.24: Specimens of porous auxetic material (Carta et al. 2016).

2-D Cellular Solids

Bertoldi et al. (2008) conducted an experimental and numerical investigation regarding the deformation characteristics and mechanics of periodic 2D elastomeric sheets. Square and diagonal lattices with circular voids rectangular lattices with ellipsoidal voids were studied. Figure 1.25 shows the initial and final deformed geometries. A 'pattern switch' during deformation was observed as the applied compressive strains exceeded elastic limits for the material. The mechanism for the switch was attributed to local elastic instability which caused a robust and repeatable deformation. Post-pattern formation deformations a further pronounced with increasing strain; a constant stress value was observed past the onset of pattern switching. Conducted eigenvalue analysis also suggested that alternative transformation patterns can be achieved given the suppression of initial deformation modes. Although the effect was replicated experimentally on the millimeter scale, numerical analysis would not inhibit the reproduction of the studied behavior in the micro or nano scale.

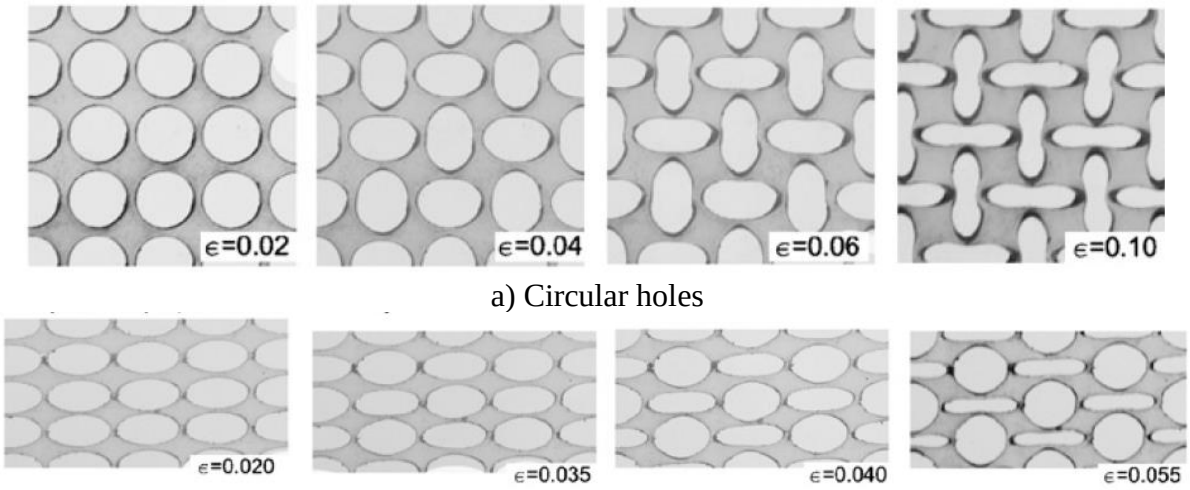

a) Circular holes

b) Elliptical holes

Figure 1.25: Experimental images from in-plane compression tests (Bertoldi et al. 2008)

In continuation of their previous work, Bertoldi et al. (2010) observed an auxetic effect in an elastomer-based, two-dimensional periodic structure. Elastic instability in the structure was credited for the pattern transformation observed; confirmed during testing owing to the likeness of the produced deformation pattern with the first eigenmode for the geometry. An initial imperfection was introduced to achieve the first mode pattern deformation, which led to uniaxial NPR behavior of the material in compression. Samples were observed to undergo a slow, uniform compression until a critical measure of applied strain, beyond which the distinguishable transformation occurred, causing a progressive decrease in the Poisson's ratio. The effect of void ratio in the bulk material was investigated; it showed that a void ratio < *0.34* induced an unwanted macroscopic instability while values > *0.34* gave rise to pattern analogous to those observed in experiments. An NPR value, $\nu = -0.904$ was predicted for a material with a void ratio of *0.70*.

Liu et al. (2016) used FE methods to simulate in-plane dynamic crushing in re-entrant honeycomb structure to test its impact response. Energy absorption of the re-entrant and hexagonal honeycombs was compared using aluminum as the base material. Simulated impact testing (see Figure 1.26 for models) showed that the re-entrant honeycomb absorbs more energy through plastic deformation than the hexagonal honeycomb under an identical strain range. This was attributed to the early densification property of the re-entrant geometry. However, the re-entrant configuration led to higher peak stresses for the same amount of energy absorption as the

hexagonal variety. Moreover, the re-entrant honeycomb stopped the impact plate in a smaller strain and time than the hexagonal honeycomb, for an impact of the same speed.

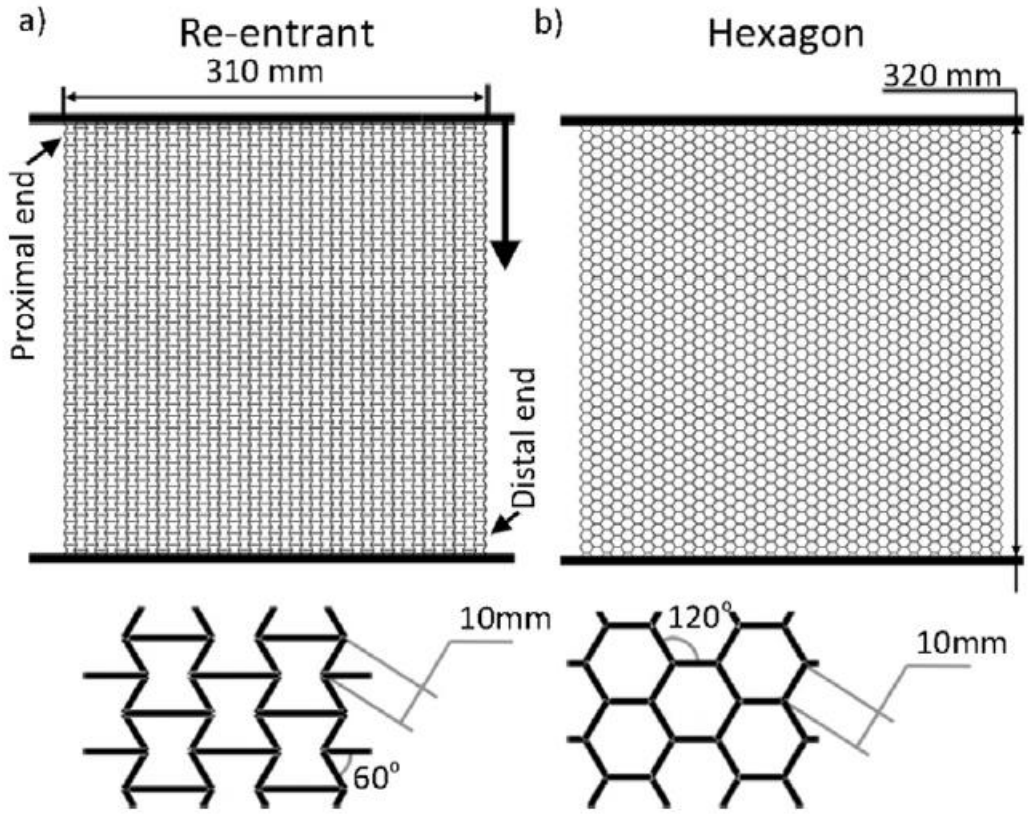

Figure 1.26: FE models for impact response testing (Liu et al. 2016**).**

Zhang and Yang (2016) tested the mechanical properties of auxetic cellular material (Figure 1.27) with a re-entrant honeycomb structure in a numerical and experimental study. Steel was used as the base material. A parametric study was conducted on the effects of Poisson's ratio and relative density on the strength and dynamic performance of the material. Results showed that given a constant Poisson's ratio and relative density, the ultimate bearing capacity for the auxetic material is scale-independent. As a result of dynamic analysis of the auxetic honeycombs, it was observed that when $v < -1.5$, an increase in cell thickness increased the vibration level difference in the auxetic honeycombs. Conversely for $v > -1.5$, a thinner thickness resulted in better dynamic performance.

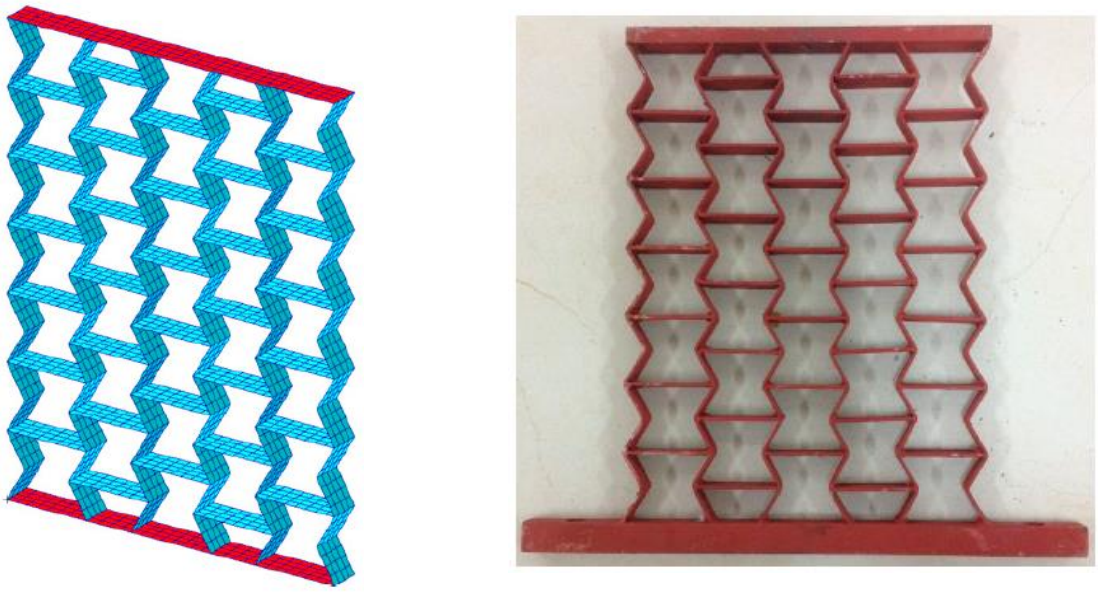

a) FE model b) Test specimen

Figure 1.27: Auxetic cellular material (Zhang and Yang 2016).

Wang et al. (2017) constructed a FE numerical model for micro-structured plates with conventional and re-entrant cells to analyze their effective elastic properties under in-plane deformation. The effective Poisson's ratios for the plates lied between *-1* and *1*. Results showed that the re-entrant angle must exceed *20°* to get a negative v value.

Ingrole et al. (2017) conducted a comparative study for in-plane compressive behavior of various regular and auxetic honeycomb structures (shown in Figure 1.28). Experiments were conducted on 3D printed elastomeric specimens. The failure modes and deformations for each sample was observed. The proposed new auxetic-strut structure showed better performance in uniaxial compression. For instance, a *300%* higher strength than hexagonal honeycomb and *65%* greater than conventional re-entrant honeycomb was observed for the auxetic strut model. The new model also showed a lower value of Poisson's ratio, which was linked to higher energy absorption.

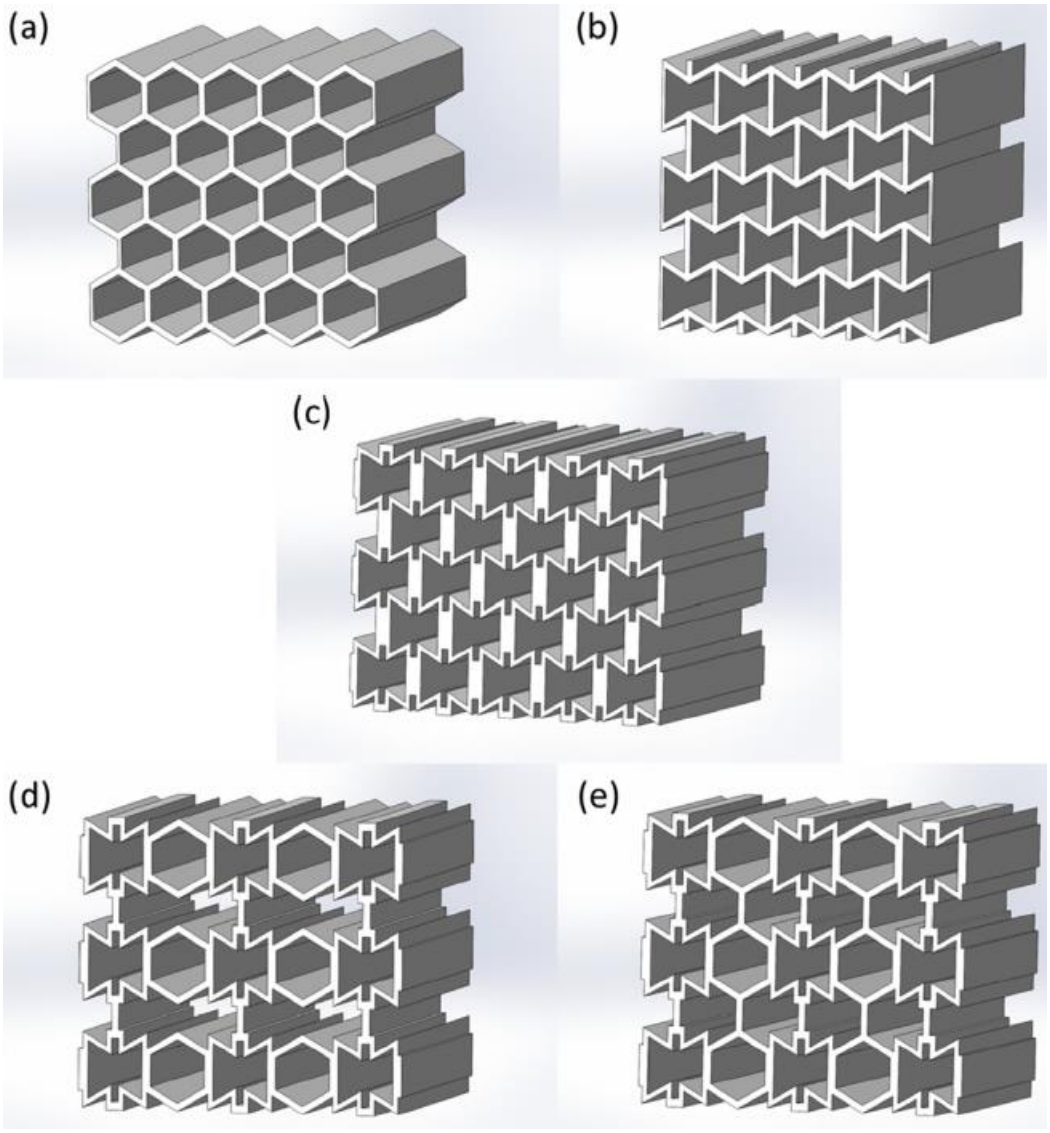

Figure 1.28: Cell design structures (Ingrole et al. 2017):
a) hexagonal honeycomb; b) re-entrant auxetic; c) auxetic-strut; d) auxetic honeycomb1;
e) auxetic honeycom2.

3-D Cellular Solids

Schwerdtfeger et al. (2010) designed and built a 3D auxetic cellular structure using the Selective Electron Beam Melting (SEBM) procedure out of a Titanium alloy (Figure 1.29 (a)). Compression testing was conducted to demonstrate the auxetic nature of the material. Subsequently, another study was conducted to analyze the deformation mechanisms and characterize the mechanical properties of this unique material (Schwerdtfeger et al. 2011). As a

result of numerical and experimental analysis, it was shown that the effective Poisson's ratio of the material was highly dependent on the relative density of the structure which suggested that changing both the internal angles and the relative density is necessary to tailor material response e.g. stiffness of the structure.

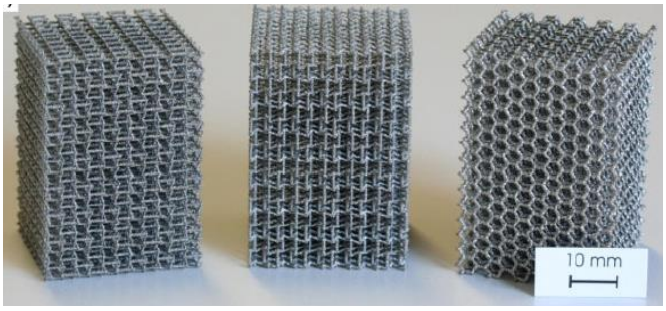

a) (Schwerdtfeger et al. 2010)

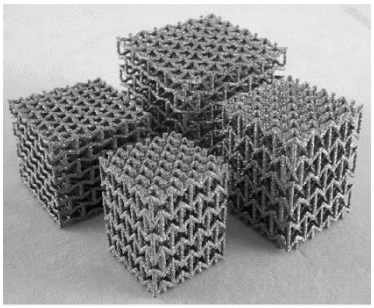

b) (Yang et al. 2012).

Figure 1.29: 3D Titanium auxetic cellular solids.

A similar auxetic material (Figure 1.29 (b)) was designed and constructed out of Titanium alloy by Yang et al. (2012) using the electron beam melting process. Different design configurations were manufactured and tested to reveal two failure modes. The failure modes showed a dependence on the ratio between the vertical and re-entrant strut length. Superior mechanical properties compared to regular foam structures were reported for the re-entrant lattice structure. Yang et al. (2015) also characterized the mechanical properties for the same structure. An analytical model was presented and the results were compared to FE models and experimental results which showed that the proposed model was reliable if manufacturing related factors were incorporated.

Ren et al. (2015) conducted an experimental and parametric investigation on metallic auxetic metamaterials with variable mechanical properties. A 3D buckling-induced auxetic material was designed which was subjected to a buckling analysis to determine deformation modes. After identifying the desirable buckling mode, the shape of the representative volume element was quantified in terms of a Pattern Scale Factor (PSF). The PSF was used as a parameter to alter the initial pre-buckling geometry (Figure 1.30 (a)). Inducing an initial imperfection or altering the initial geometry according to the desired mode made the response continuous under applied axial deformation. The tested models were manufactured with brass as a base material due to its high

ductility. Samples with PSF values of *0%* and *20%* (Figure 1.31 (a)) were tested under uniaxial compression to observe the effect of a change in initial geometry.

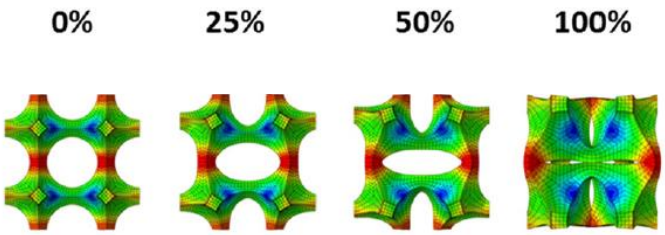

a) Quantification of PSF

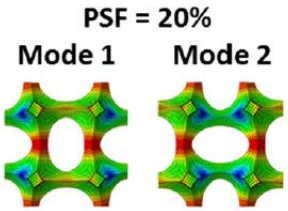

b) Buckling modes of unit cells

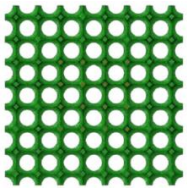

c) Bulk material with PSF = *0%*

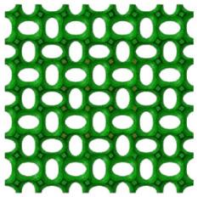

d) Bulk material with PSF = *20%*

Figure 1.30: Design of 3D metallic buckling-induced auxetic material (Ren et al. 2015)

Subsequently, FE models were created and validated against experimental results. The Poisson's ratio for the original, unaltered geometry was positive; showing non-auxetic behavior. However, inducing a *20%* PSF caused an immediate NPR effect with a continuous decrease up to and beyond a nominal strain of *0.34*. When comparing base materials, for the original buckling induced material, there was no auxetic behavior in both FE and experimental results for brass, while the elastomer was auxetic (Figure 1.31 (b) and (c)). This was attributed to the plastic deformation in brass. Meanwhile, there was an immediate auxetic behavior of equal magnitude observed in both rubber and brass materials with a *20%* PSF value; demonstrating that auxetic performance was not dependent on the base material, rather the geometric configuration had a significant effect. A parametric analysis using validated FE models showed that an increase in PSF leads to a higher absolute value for NPR while constricting the effective strain range. Additionally, a strain hardening ratio beyond *0.2* was shown to have negligible effect on auxetic performance. The study established an upper limit for the volume fraction of *34.5%*. Even though a reduction in

volume fraction displayed heightened auxetic behavior, an established range of *25.9-34.5%* mitigated detrimental effects to strength and stiffness due to excessive loss of material.

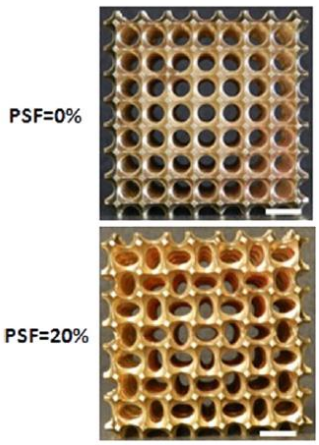

a) Brass specimens

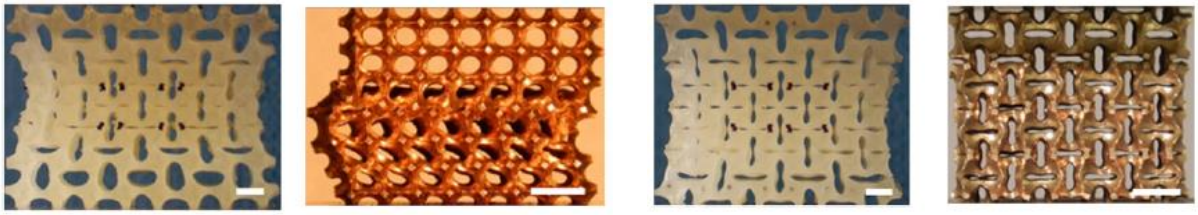

b) Deformed geometry for PSF = *0%* elastomer and brass

c) Deformed geometry for PSF = *20%* elastomer and brass

Figure 1.31: 3D metallic buckling-induced auxetic material (Ren et al. 2015)

Tubular Structures

Scarpa et al. (2008) conducted analytical and numerical research on the mechanical properties of an auxetic tubular structure constructed with re-entrant center-symmetric cells. Expressions for Young's modulus and Eulerian buckling mode were derived. Finite element models of the tubes were also created and parametric analysis was conducted to determine the effects of cell geometry and number of circumferential cells. Analytical models based on simple bending stiffness yielded satisfactory results while the FE analysis showed dependence on hinging and axial deformation in cell ribs. Figure 1.32 shows the model for an auxetic tube.

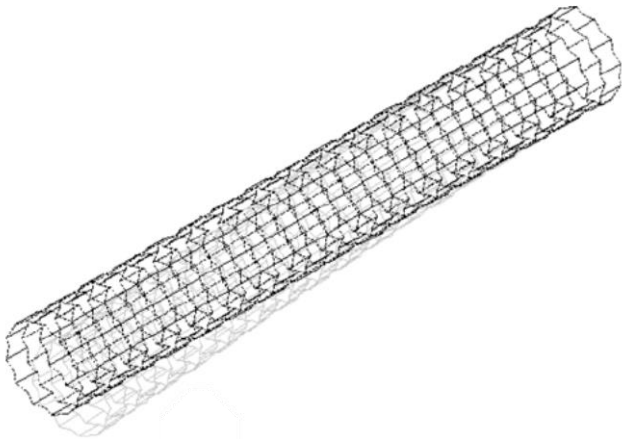

Figure 1.32: Auxetic tube configuration for FE model (Scarpa et al. 2008)

Ren et al. (2016) studied the auxetic performance of a tubular auxetic material with elastic instability inspired by Bertoldi et al. (2008) and Bertoldi et al. (2010). Adopting a similar procedure to their previous work (Ren et al. 2015), a geometry with a void fraction of *0.69* was used and the first buckling mode (Figure 1.33 (c)) was selected for testing because of its regular deformed geometry. Physical and FE models with PSF values of *0%* and *20%* (Figure 1.34 (a) and (b)) were tested in uniaxial compression. While the tubular structure with PSF = *0%* was non-auxetic, the PSF = *20%* material demonstrated NPR behavior with a consistent $v \cong 0.8$ over a large strain range. Research showed a reduced effective strain range for an increase in PSF. Base material had an effect only for the unaltered tubular geometry, as per validated FE models.

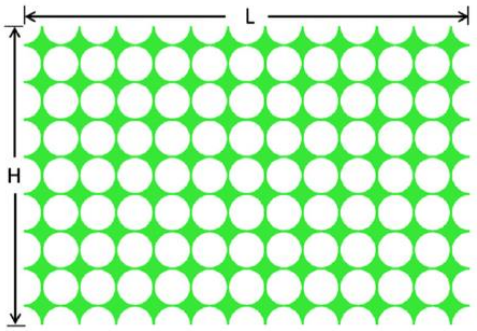

a) Planar geometry

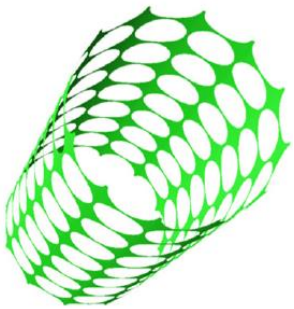

b) Tubular geometry

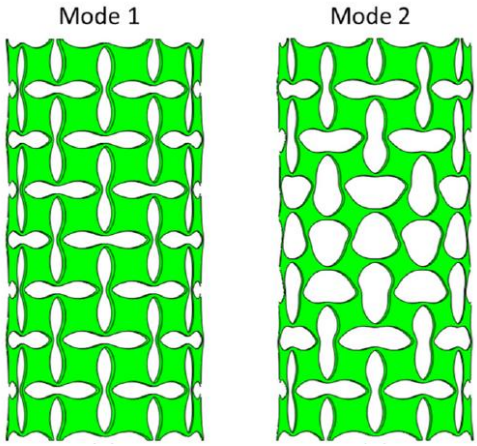

c) Buckling modes of tube structure

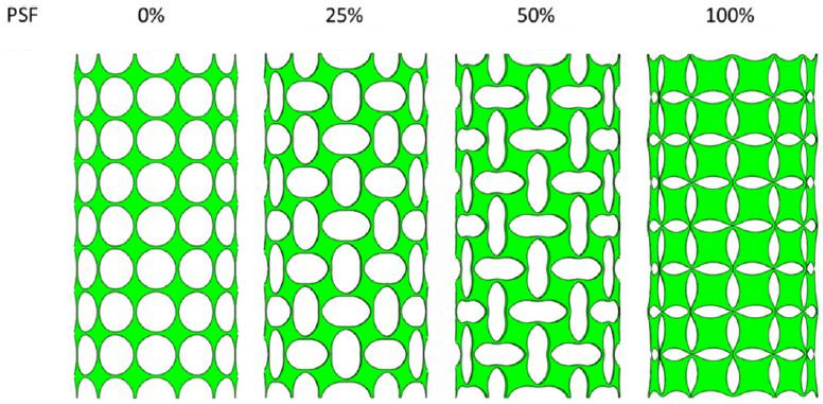

d) Visual representation of PSF

Figure 1.33: Design of 3D metallic buckling-induced auxetic tube (Ren et al. 2016)

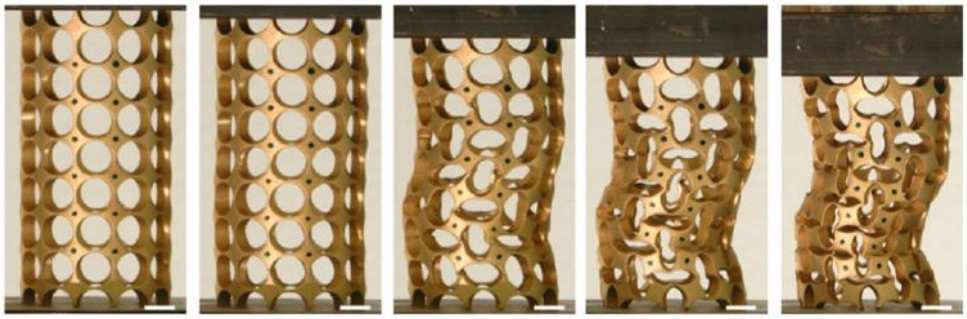

a) Brass specimen with PSF = *0%* under uniaxial compression

b) Brass specimen with PSF = *20%* under uniaxial compression

Figure 1.34: Experimental testing of 3D metallic buckling-induced auxetic tubes (Ren et al. 2016)

The resistance to kinking in auxetic tubes was studied by Karnessis and Burriesci (2013). Collapse of tubes with re-entrant geometry of cells was investigated under pure bending to gauge potential for use as angioplasty stents or annuloplasty rings. Numerical and analytical models were built to determine deformation behavior. Models confirmed that auxetic re-entrant honeycomb structure demonstrated a better resistance to local instability failures under pure bending. A numerical model with a typical deformed shape under bending has been presented in Figure 1.35.

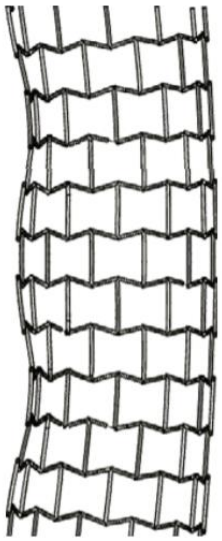

Figure 1.35: Rippled deformed shape for auxetic tubular structure under pure bending (Karnessis and Burriesci, 2013)

In another analytical study conducted by Gatt et al. (2014), The mechanical properties of a tubular auxetic material were derived based on the rotating rigid square methodology. Expressions predicting the Poisson's ratio as well as Young's modulus were derived for a finite 2D planar rigid square model as well as a 3D tubular configuration. Comparison of properties with an infinitely sized system suggested an overprediction of Young's modulus in the infinitely sized system. Use of finite-sized tubular auxetics as esophageal stents was also proposed. The tubular auxetic analyzed has been presented in Figure 1.36

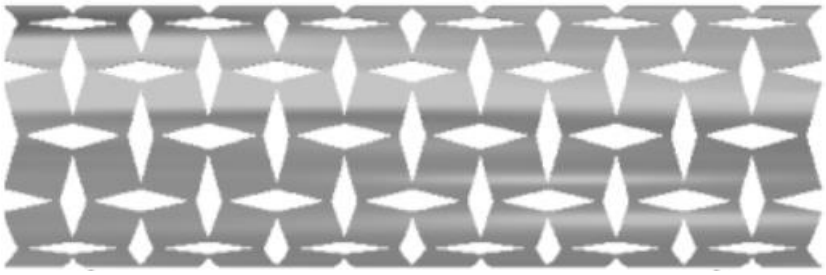

Figure 1.36: Tubular structure constructed with rigid rotating squares (Gatt et al. 2014)

Broeren et al. (2019) presented a spatial pseudo rigid-body model to analyze the behavior of an elastomeric tubular auxetic structure under axial compression. The model quantified deformations based on the rotations of rigid squares connected using torsional springs. Two types of models were presented and the results computed were compared to experimental data for

validation. The models captured the mechanical behavior of the tube and replicated the deformed shape with a high accuracy as illustrated by the photographs in Figure 1.37.

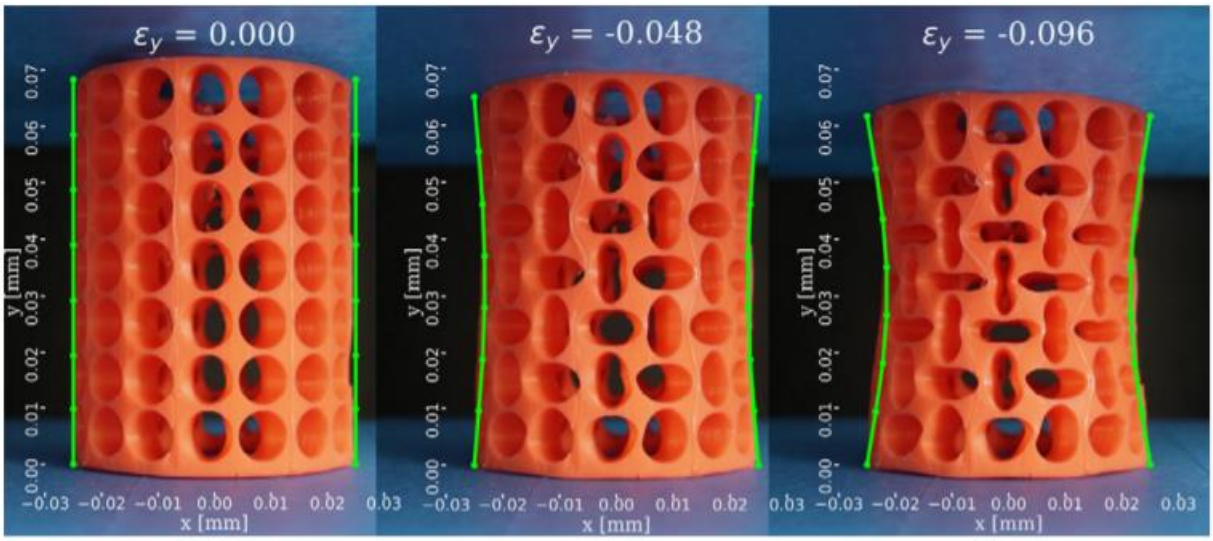

Figure 1.37: Comparison of predicted deformations (green) to experimental results in tubular auxetic under axial compression (Broeren et al. 2019)

The crash worthiness of metallic tubular auxetic structures was studied by Lee et al. (2019). Metal tubes were designed and manufactured using an additive manufacturing process with conventional solid geometry as well as a regular and re-entrant honeycomb geometry. Experimental crash testing and FE analysis was conducted. It was concluded that NPR behavior influenced the deformation mode of the tubes with a radial densification effect only observed in the auxetic configuration. Plastic deformations were homogeneous in the auxetic tubes while buckling was observed in the conventional and regular honeycomb geometries. Densification in the auxetic units led to a higher specific energy absorption. Under low impact conditions, the auxetic tubes exhibited higher specific energy absorption compared to conventional solid tubes despite sustaining lower crash forces. Steady deceleration was observed which led to an enhancement in damping forces. Auxetics demonstrated better energy absorption and damping capabilities in low impact conditions, solidifying their potential in crash-protection applications. A comparison of deformed shapes in FE models have been presented in Figure 1.38.

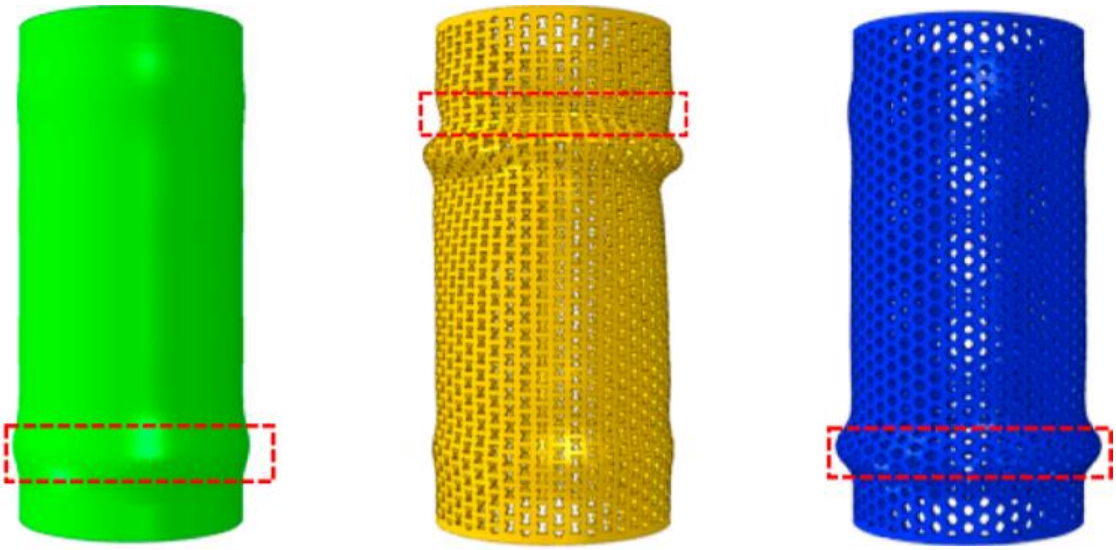

a) Conventional tube b) Auxetic tube c) Honeycomb tube

Figure 1.38: Folding regions in FE models (Lee et al. 2019)

1.5. Conclusions from Literature Review

The following conclusions can be drawn from a review of relevant literature:

1. Auxetics are novel "metamaterials" that have been shown to have enhanced mechanical properties compared with conventional materials, owing to their specific geometric arrangement. As many mechanical properties have been shown to be analytically proportional to the Poisson's ratio v, a negative value is shown to cause enhancement in other mechanical properties such as shear modulus G, out-of-plane deflection, fracture toughness, indentation resistance and volumetric strain energy dissipation.

2. Auxetic behavior in elastic materials is scale-independent as same auxetic configurations with different cell size are shown to exhibit identical Poisson's ratios. However, behavior is fully dependent on the geometry of constituent elements e.g. shape, relative size and orientation of cells walls affect Poisson's ratio. These geometric parameters can be tuned to achieve desired mechanical properties.

3. Most research in auxetics focuses on 3D-printed elastomeric components which do not possess high load-bearing capacities suitable for many infrastructure and mechanical systems applications. There is a limited body of research involving ductile metals.

4. Current experimental research based on metallic auxetics revolves around specimens manufactured with Titanium-Aluminum alloys or Brass; none of which are structural metals.

5. Existing studies focusing on metallic auxetics are limited by the scale of additively manufacturing techniques. Size of manufactured and tested specimens currently sits in the $10\ mm - 100\ mm$ range; built geometries are too small for use as structural components. However, research into large-scale manufacturing techniques can expand applications of metal auxetics into the structural element domain.

6. Ductile metal auxetics have been shown to possess energy-dissipating potential based on their novel deformation behavior. The use of auxetic geometries can potentially lead to components capable of dissipating and absorbing greater amounts of energy while weighing less and occupying the same volume of conventional metal components. These potential applications have not been explored with very limited published research. However, research concerning elastic materials is very encouraging with existing applications in the fields of medicine and footwear.

7. The effects of transition from elastic to inelastic behavior in auxetics is relatively unexplored. Some studies have suggested an enhancement in the auxetic effect due to inelastic deformations but no significant experimental research has been conducted to explore the on Poisson's ratio when a material transitions from elastic to the inelastic domain.

8. The existing body of knowledge does not survey the potential structural, load-bearing applications of ductile metal auxetic structures. While existing research confirms beneficial mechanical properties of auxetics, potential use as elements of a structural system has not been explored.

1.6. Potential Applications for Metal Auxetics

Potential applications of metallic auxetic materials as structural components for load dissipation under seismic, blast and impact loading are discussed in this chapter. If auxetics are proven to demonstrate a high effective strain range and enhanced hysteretic performance, these properties can be leveraged to enhance existing structural elements while auxetic structural elements can also be developed, which would be capable of dissipating high energy under extreme imparted loads. An enhanced energy absorbing capability is also expected to lead to damping characteristics in metal auxetics. Subtractive manufacturing, if possible, may lead to a significant weight reduction in structures while maintaining strength.

Figure 1.39 shows the potential use of a ductile metal auxetic tube as an outer casing for in a composite concrete column. Under axial compression, the inner concrete core would have a tendency to expand outward due to PPR behavior. However, the outer metal auxetic shell can be designed to counter the radial expansion of the concrete thus, effectively applying external confinement to the concrete. This confinement may lead to enhanced strength and ductility. The uniform deformations caused by the NPR behavior of the outer metal tube would also ensure the concentric nature of a purely axial forces, thereby minimizing second order effects and maximizing Euler buckling loads.

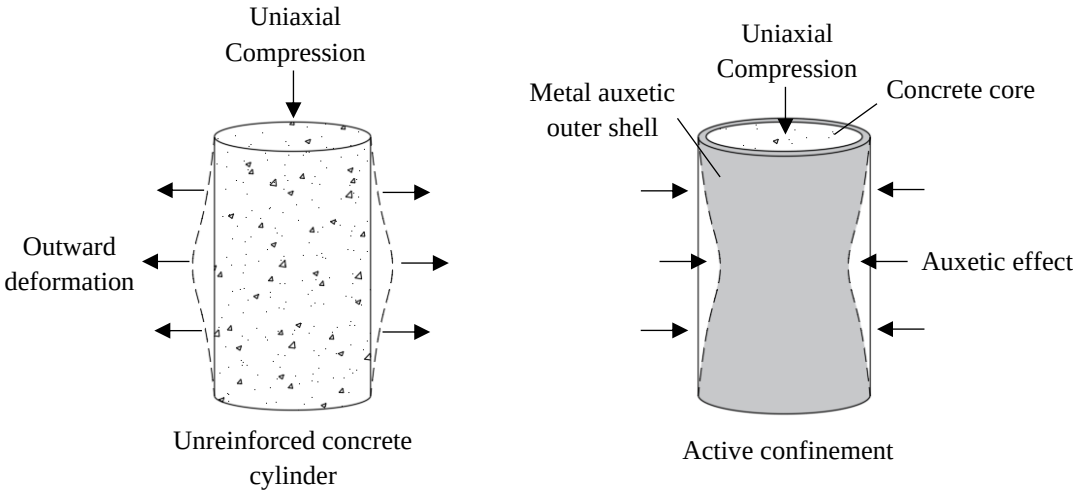

Figure 1.39: Confined concrete cylinder using metal auxetic jacket

Metal tubes are currently used as bracing members in lateral force resisting mechanisms. A ductile mechanism to dissipate energy using a conventional bracing system formed through the

plastic deformations produced by buckling in compression and inelastic yielding in tension. However, the inelastic deformations in both tension and compression are localized at certain locations (usually mid-span) along the length of the tube instead of being uniformly distributed along the length. This makes these ductile mechanisms highly inefficient. A lot of material level ductility is lost in transition to the element level. Deformation modes are also very unstable, especially in compression, unless external buckling resistance is provided which is extremely costly. Contrarily, using ductile metal auxetic tubes can be an extremely efficient way to dissipate energy in a lateral force resisting mechanism, as demonstrated in Figure 1.40. The geometry of voids can easily be tuned to achieve symmetric behavior in both compression and tension, while strength can be maintained by varying material thickness. Due to the stable failure modes of these tubes, plasticity can be distributed along the length of the tube while maintaining concentric axial forces, which would delay second-order effects and instability failures. Auxetic metal braces have the potential to demonstrate high energy dissipation capability while ensuring cost-effectiveness in the process. Removal of material can also reduce the weight of the structure.

Another possible use of ductile metal auxetics in the form of energy absorbing connections has been presented in Figure 1.41. Auxetic metal connections can potentially be utilized as energy absorbers to mitigate the effects of blast loads on structural elements. Coupled with a load distributing element, specially designed energy absorbing connectors can have high yielding loads that do not surpass failure loads of the connected structural element, thereby transferring lower maximum reaction forces to the connected structure. Connection can be designed to have a long, stretched out yield plateau, that would maximize dissipation of energy before reaching failure loads. Additionally, the use of metal foams as filler material to increase energy dissipation can be explored.

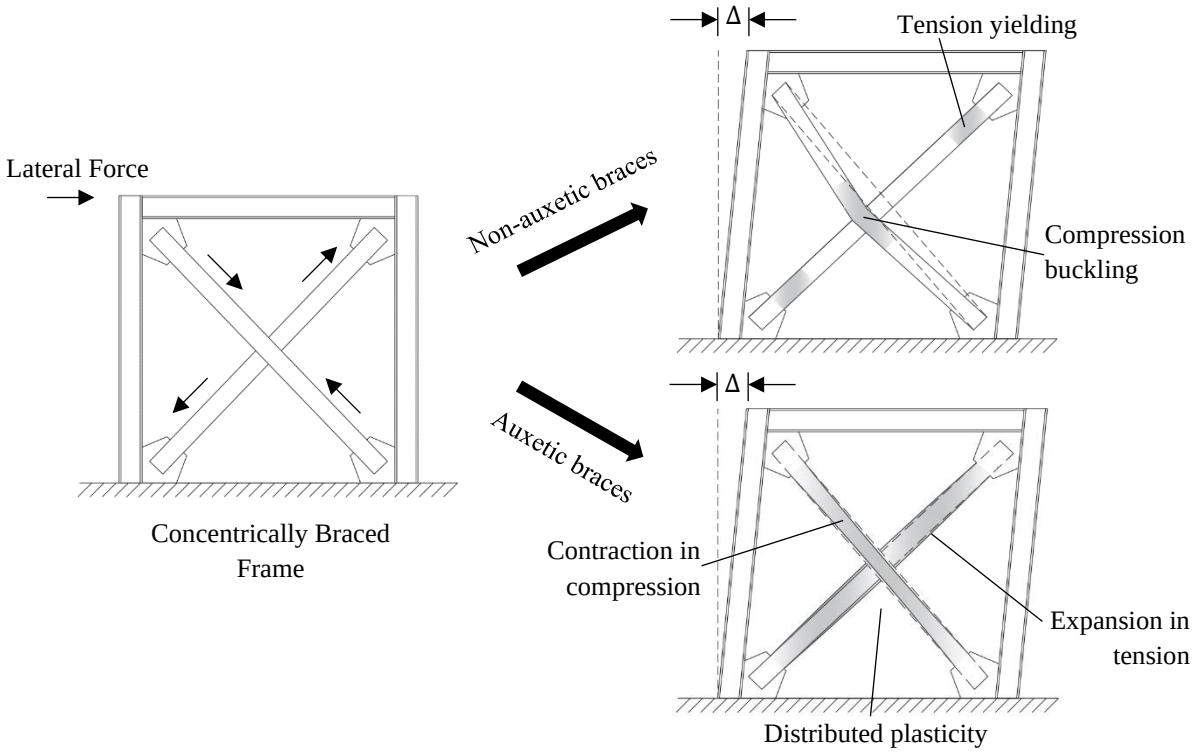

Figure 1.40: Use of tubular auxetics in a structural bracing system.

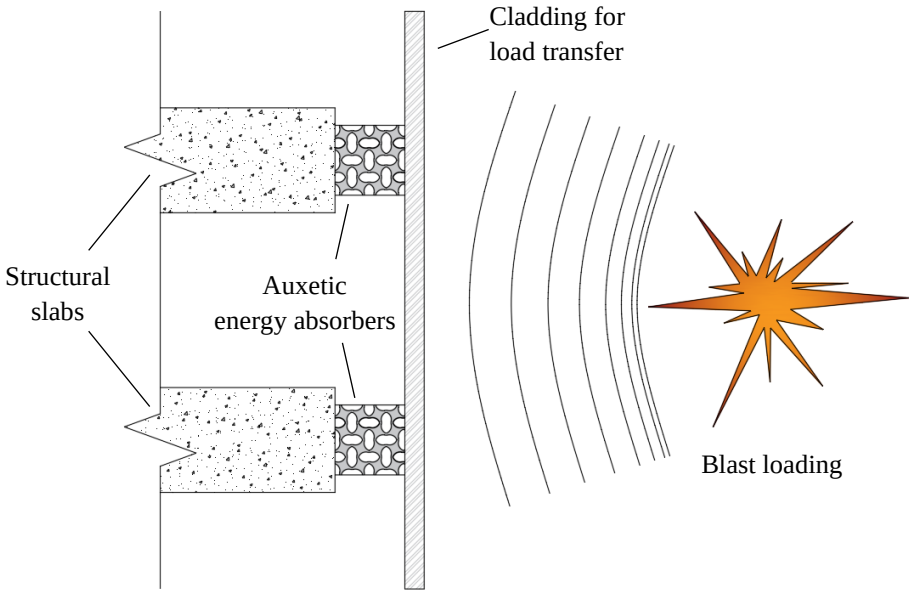

Figure 1.41: Auxetic Energy Absorbing Connectors.

Auxetic dampers can also be utilized in automotive bodies to mitigate the effects of collisions. Crash barriers incorporating auxetic energy absorbers can be designed to withstand high

impact forces while dissipating energy. Both potential applications have been presented in Figure 1.42.

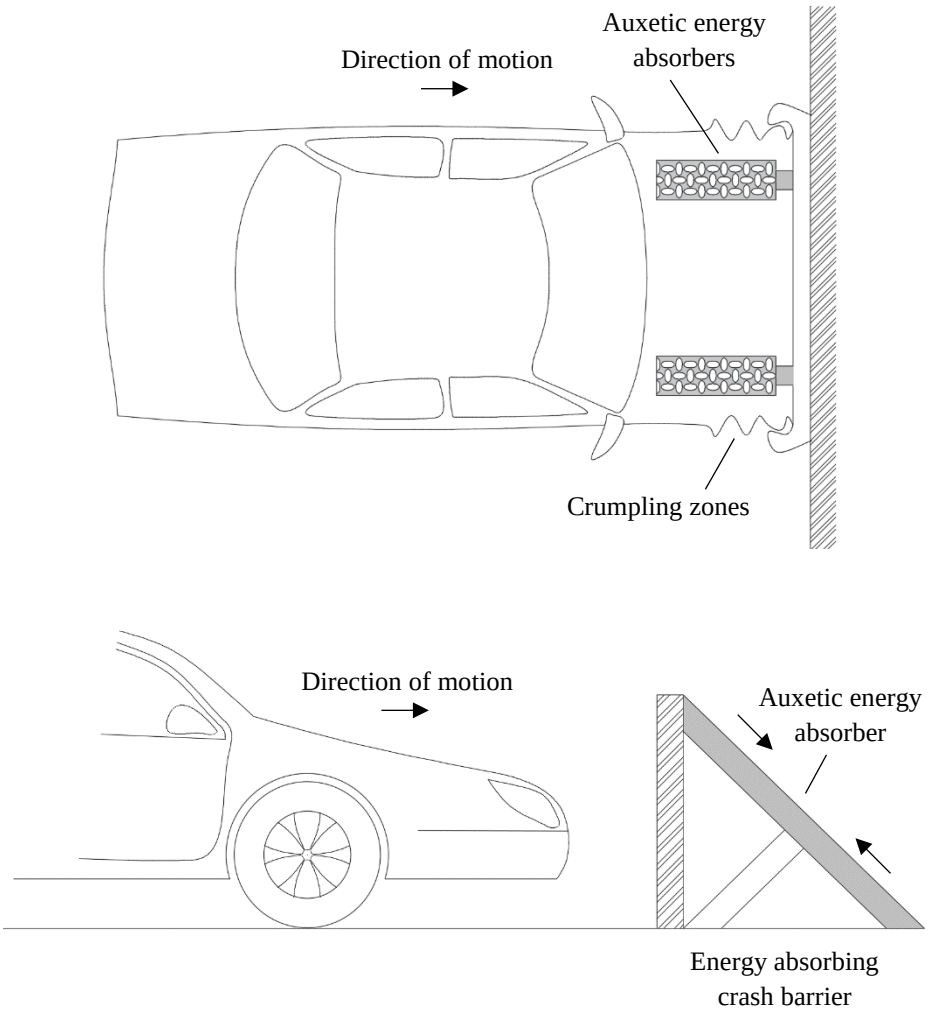

Figure 1.42: Energy Absorption in Collisions.

The radial contraction caused by compressive force can be to produce frictional damping forces using a system similar to the cladding connection designed by (Lu, 2017). As shown in Figure 1.43, a dual cylinder friction system can be designed and incorporated into the existing structural system. Frictional forces are developed by the normal forces applied to the inner cylinder by the outer cylinder under compression, with their magnitude dependent on the applied external loads. A load transfer mechanism can be designed, consisting of an external blast-resistant cladding connected to the actual structural system via the frictional dampers as shown. Laterally acting blast forces are transferred from the external cladding to the outer friction cylinder.

Auxeticity in the cylinder would cause a radial contraction, thereby applying normal forces to the inner fixed cylinder. This normal force would generate frictional damping forces proportional to the applied load thus, reducing the effects of blast forces on the structural system.

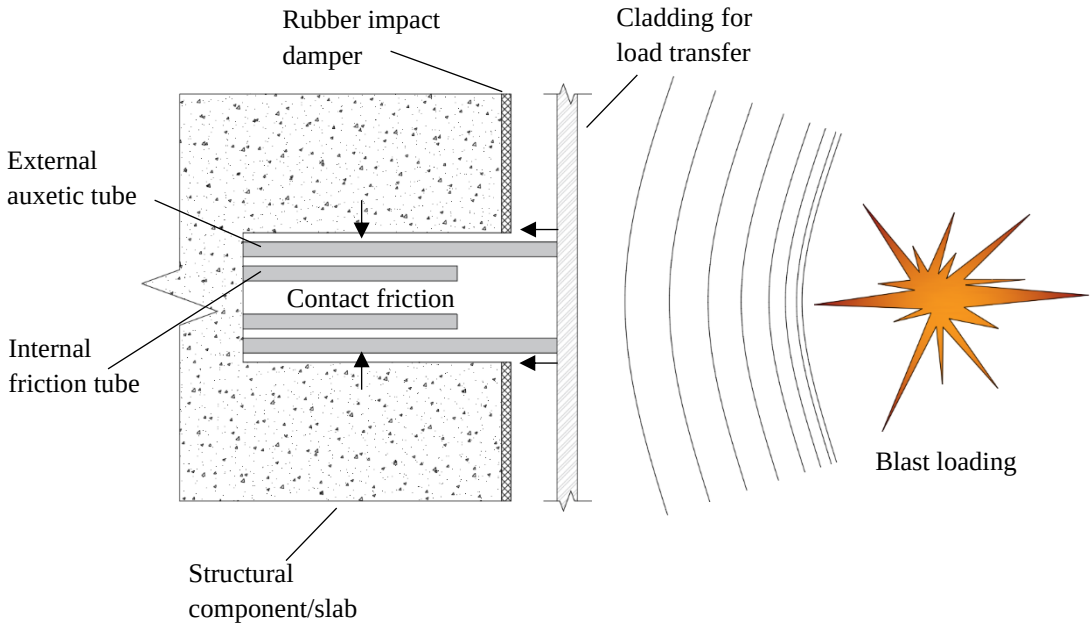

Figure 1.43: Integrated Auxetic Frictional Damping System.

Chapter 2. Experimental Program

2.1. General

This chapter provides an overview of the experimental program developed to study the performance of ductile metal tubes with auxetic topologies cut into the tube walls. The experimental program involves the design, construction, and testing of eight auxetic and non-auxetic tubular specimens. Background information on design of the auxetic topology, material properties, loading protocol, and test configuration are presented in this section.

2.2. Auxetic Unit Cell Design

This project began with the intent to design a planar auxetic test specimen using subtractive manufacturing to cut auxetic geometries in plate steel and aluminum materials. Discussions with local laser and water-jet cutting services indicated that the minimum cell size they could prepare was roughly *250 mm*^{2} each, meaning that a planar specimen with approximately *100* total cells would be too large for readily available uniaxial test equipment to accommodate. Additionally, while planar coupons are well-suited for tensile loading, they are prone to out-of-plane buckling in compression (Timoshenko and Gere 1961). However, if the planar geometry was folded into a tube structure, a similar number of cells could be accommodated in a sample better suited for uniaxial testing. Furthermore, from a manufacturing perspective, 6-axis tube laser cutting machines are better suited to preparing the small, intricate openings required for this research. In regards to previous research, tubular auxetic structures have been reported in the literature, additively manufactured using plastic (Broeren et al. 2019) and brass (Ren et al. 2016) measuring roughly *100 mm x 50 mm* in height and diameter. However, the research described in this thesis represents a substantial divergence from existing research in that there is no background on the performance of auxetics at large geometric length scales using typical materials encountered in civil infrastructure and mechanical systems. Therefore, it was decided to proceed with the design, manufacture, and testing of large-scale tubular specimens to study the effect of auxeticity in ductile metallic structures.

The auxetic unit cell design was based on an initial planar array of circular voids, similar to those studied by Bertoldi et al. (2010) who examined auxeticity in topologies derived from elastic buckling of circular arrays. The initial planar array, illustrated in Figure 2.1 (a), was *147 mm* long by *98 mm* tall with *11.5 mm* diameter openings having a porosity *69%*, selected to maximize NPR behavior (Bertoldi et al. 2010). A coordinate transformation was then used to convert the reference planar geometry into a circular tube. The resulting tubular configuration, illustrated in Figure 2.1 (b), was then scaled up to the (AISC 360-16) standard for a Pipe6STD circular tube using with an outer diameter (D_0) of *168.5 mm* and wall thickness (t_w) of *7.1 mm.* This specification was chosen such that readily available materials could be used to manufacture specimens.

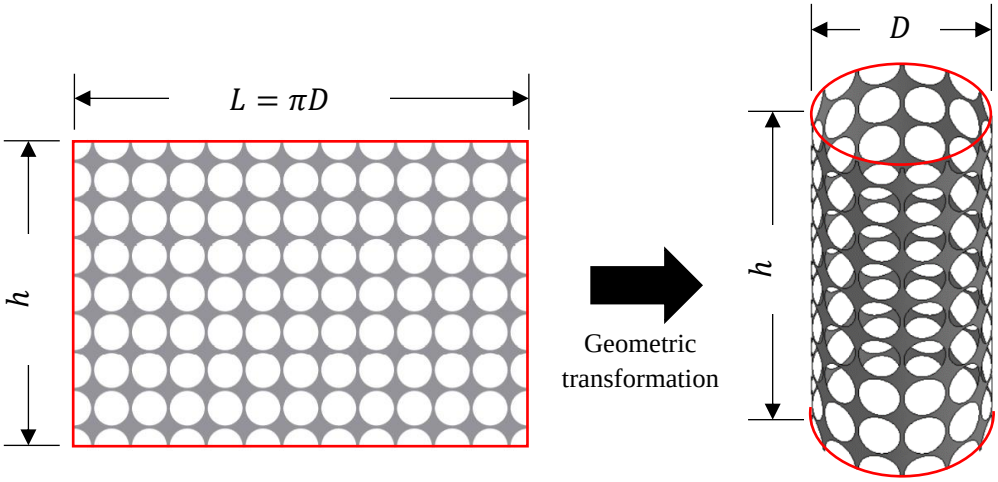

Figure 2.1: Geometric transformation from planar to tubular configuration for auxetic unit cell design.

Ren et al. (2016) demonstrated that the elastic buckling modes of a tube with an initially circular array of voids will exhibit auxetic behavior if new topologies are created from the buckled deformed shape with the degree of auxeticity being controlled by the relative deformed configuration. Using a similar approach, the auxetic topologies proposed in this research were generated by subjecting the baseline Pipe6STD tube with circular voids to progressively increasing monotonic compression using a nonlinear FE model. The results of the compression loading simulation were used to establish the deformed configuration of the cells up to the onset of densification, where complete collapse of the voids caused the cell walls to touch. The degree of deformation in the cells was quantified using a *Deformation Ratio* (DR) defined by the percentage

ratio of the change in diameter of the circular cells to the original diameter. A $DR = 0\%$ referred to the undeformed circular geometry while a $DR = 100\%$ represented complete collapse with opposing cell walls touching. It was predicted that a 0DR tube with fixed ends would be non-auxetic while any DR value greater than *0* would exhibit auxetic behavior due to elastic instability induced by the shape of the cells. Deformed shapes have been displayed in Figure 2.2 with their respective DR values.

The nonlinear finite element model was created using shell elements to represent the Pipe6STD tube with circular voids. The model was meshed using a spacing of *3 mm*. A scaled rendering of the initial circular array model used for auxetic unit cell design is illustrated in Figure 2.2 (a). The boundary conditions of the model used for unit cell design were selected to allow the tube to contract radially and shrink longitudinally. The nodes on the bottom boundary were restrained against vertical (Z) displacements and against rotations about the horizontal (X and Y) axes. In addition, one node at the bottom boundary was restrained against all six degrees of freedom to prevent lateral translation. Nodes at the top boundary were restrained against rotations about the X and Y axes, while vertical compressive displacements about the Z axis were imposed for deformation-controlled loading. The stress-strain material properties of the tube were assumed to be elastic-perfect plastic with properties consistent with ASTM A36 steel (ASTM Int'l 2019) having a modulus of $E_s = 200\ GPa$, a yield strength of $f_y = 248.2\ MPa$, and a Poisson's ratio of $v = 0.26$. The analysis was conducted using LS-DYNA (LSTC 2018) running on the Virginia Tech Advanced Research Computing (ARC) (ARC n.d.) cluster.

As intended, NPR behavior was observed as the diameter of the pipe contracted under vertical compression. The intersection of the initially circular voids was observed to rotate under combined flexural and axial loads, which resulted in plastic hinges to form in the cell walls, thereby causing the unit cell to deform into a rotated elliptical pattern. However, the uniform radial contraction over the entire height of the tubes observed in the simulation was not a realistic deformation mode that could be practically achieved in a relatively short specimen tested in the laboratory. Therefore, it was necessary to modify the boundary conditions in the simulation to provide the high degree of radial restraint at the tube ends expected during laboratory testing. The deformed rotated elliptical patterns obtained from the simulation formed the basis of the auxetic unit cells evaluated in this research. The results of the simulation used for auxetic unit cell design

are shown in Figure 2.2 (a) through (d) which illustrate the deformed shape of Pipe6STD tube with circular array as a function of DR.

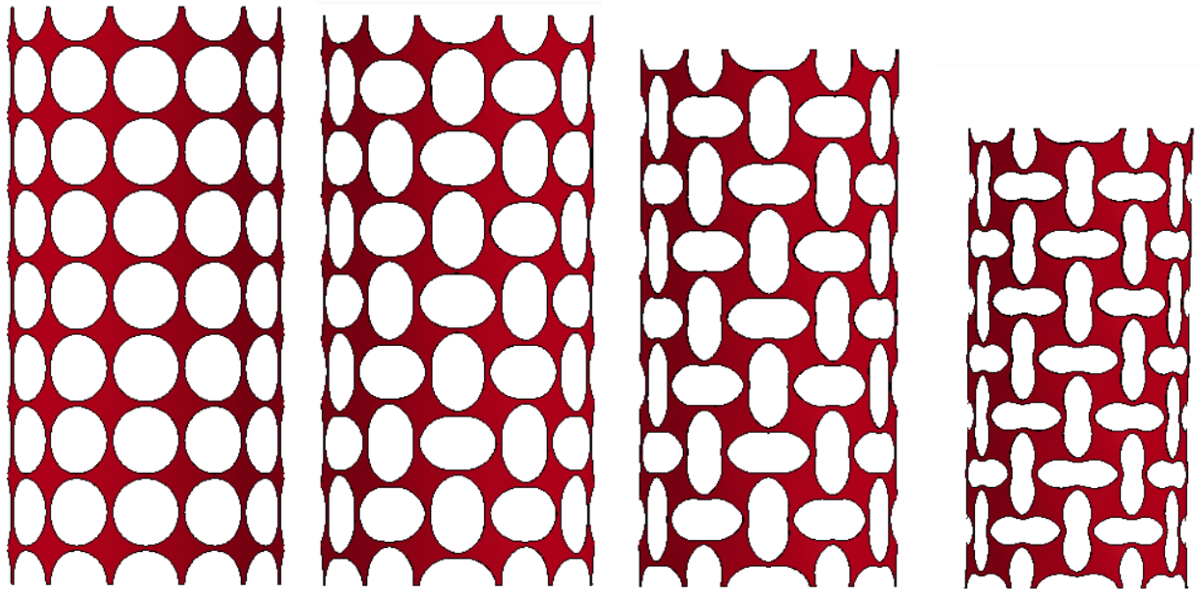

(a) $DR = 0\%$ (b) $DR = 20\%$ (c) $DR = 40\%$ (d) $DR = 60\%$

Figure 2.2: Deformed shape of Pipe 6STD tube with circular array as a function of $\boldsymbol{DR}$.

A tube corresponding to $DR = 20\%$ was modeled and vertical compressive deformation was simulated numerically to test the effect of topology on the transverse deformations. The FE model had the same material parameters, tubular height, diameter, and wall thickness as the initial DR = 0% tube. The $DR = 20\%$ tube, however, had the top and bottom boundary restrained against all degrees of freedom while the top boundary was unrestrained against vertical (Z) deformation only. Figure 2.3 shows the deformations observed in the $DR = 20\%$ tube with realistic boundary conditions. Under vertical compressive deformations, the tube was observed to contract radially as well as vertically, demonstrating NPR behavior. This confirmed the initial hypothesis that auxeticity could be achieved despite having fixed boundary conditions, with auxeticity induced solely due to applied topology. However, the degree of auxeticity was non-uniform over the height of tube with the mid-height layer of cells exhibited the most inward deformation while the layers near the boundaries deformed the least. The degree of non-uniformity is related to the fixed boundary provided at the end of the auxetic pattern.

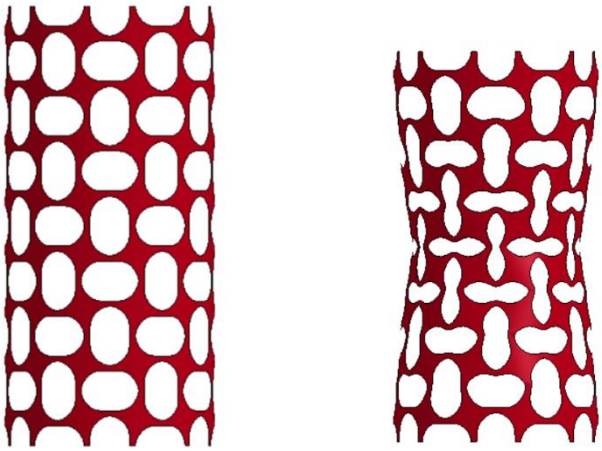

a) Original Shape b) Deformed shape

Figure 2.3: Initial $\boldsymbol{DR = 20\%}$ Tube Analysis.

Final test specimens were designed to have cell geometries that were large enough to engage local buckling instability in cell walls. Topologies with low DR values were favored to maximize the effective strain rate as high DR shapes can only sustain relatively small levels of deformation until contact of the cell walls and material densification occurred. Thus, specimens were designed with cell geometries corresponding to $DR = 20\%$ and 40% to ensure auxetic behavior and a large effective strain range.

The dimensions of the deformed cells from the design tube were scaled down by the ratios of diameters of final tube and the design tube to obtain final cell geometries. Change in the DR value for designed specimens also caused a change in the porosity. This was caused due to the direct scaling of the deformed cell geometry by the ratio of the undeformed radii. In the FE models, the cells contracted along with the tube, maintaining the porosity. As these deformed cells got smaller with an increase in DR, the porosity in the final manufactured specimens increased with DR.

Specimens with geometries corresponding to DR values of *0%*, *20%* and *40%* were designed and tested. The established naming scheme was established is presented in Figure 2.4

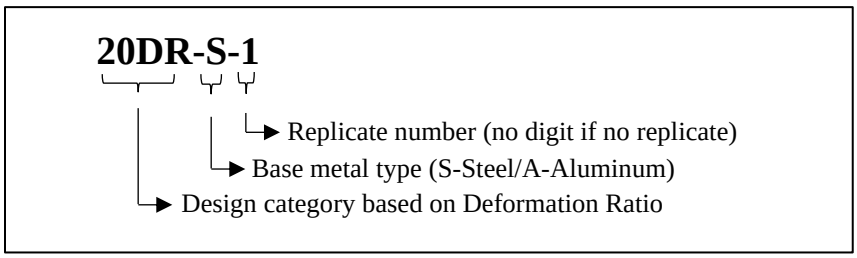

Figure 2.4: Naming scheme for Test Specimens.

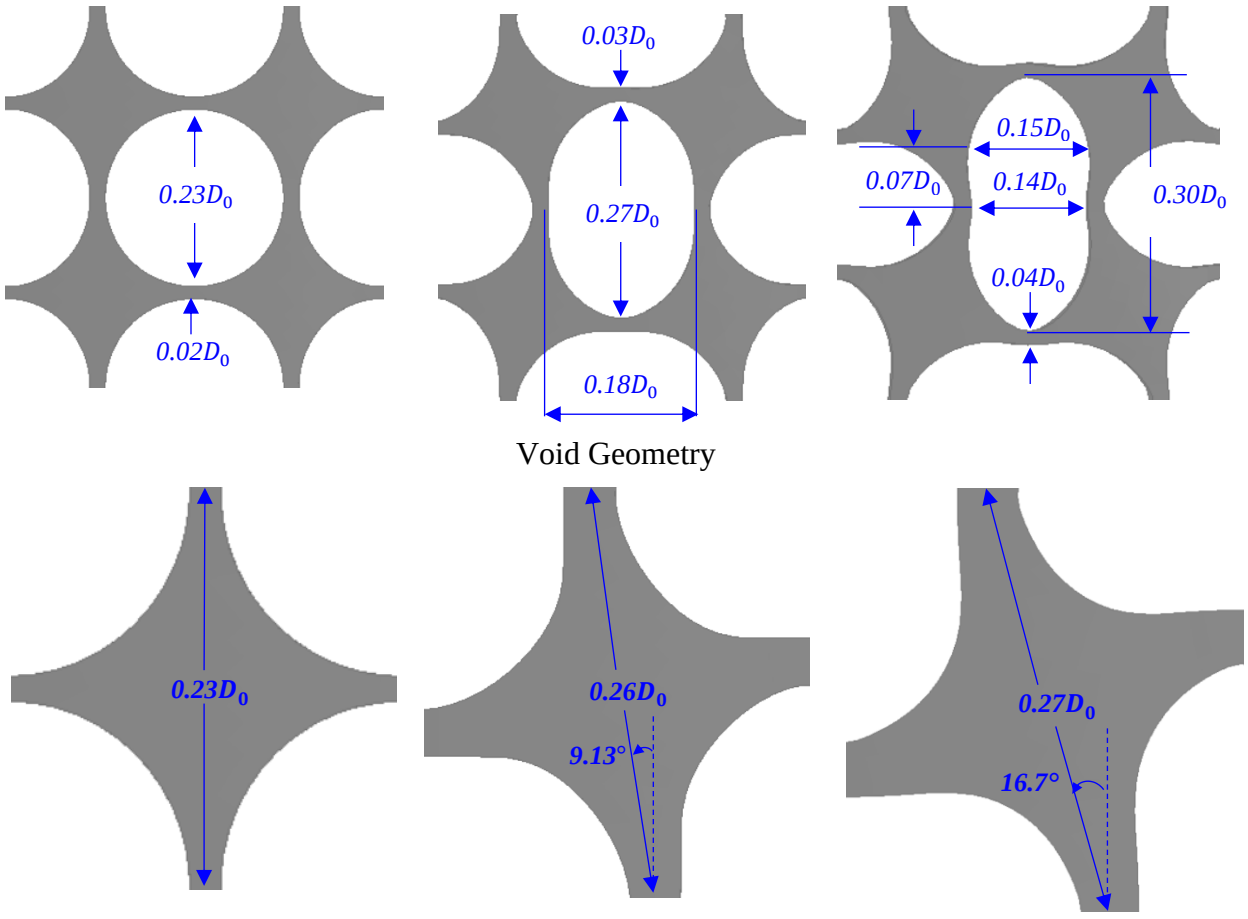

Figure 2.5: Nondimensional cellular configuration of 0DR, 20DR and 0DR unit cells.

The 0DR tubes were intended to be non-auxetic control specimens while positive DR values were expected to be auxetic in nature. Figure 2.5 shows the nondimensional cellular geometry of a cell corresponding to 0DR, 20DR and 40DR in terms of the initial buckling tube diameter, D_O of *168.5*

mm. Final test specimens had cellular arrays with *9* rows of cells having *12* cells in each row; a total of *108* cells.

2.3. Description of Tubular Specimens

A total of eight ductile metallic tubular specimens were manufactured and tested. Table 2-1 presents the test matrix for the tubular specimens. Five specimens were prepared from EN 10025 standard S355JR (DIN 2005) grade steel while the remaining three were prepared from EN AW-6060 grade (DIN 2016) T66 temper aluminum. The material specifications follow European standards as the tubes were prepared by Laser Galicia in Spain with finished samples shipped to Blacksburg, VA for testing. Aluminum and Steel were selected as base metals as they are typical structural materials used in structures, vehicles and aircrafts. The use of different base metals also benefitted in studying the effect of base metal mechanical properties on auxetic behavior.

The overall height of all specimens (H) was *457 mm* while deformations were only observed over a measured gauge height (H_G) of *317.5 mm*. The steel tubes had a wall thickness (t_w) of *4.4 mm* thick and an outside diameter (D_O) of *127 mm*, while the wall thickness and diameter of the aluminum tubes were *5.2 mm* and *125 mm*, respectively. The geometry of the cellular topology for each specimen was scaled using the appropriate nondimensional cellular configuration shown in Figure 2.5 and the specified tube diameter D_o. The effective cross-sectional area of the specimens (A_o), corresponding to the smallest cross-sectional area, was measured at the mid-height of each cellular geometry. The geometries of the test specimens for different values of DR and corresponding porosity (φ) are shown in Figure 2.6

Table 2-1: Test Matrix for Metal Tube Specimens

Designation	Deformation Ratio (DR)	Base Material	Wall Width, w_r (mm)	Wall Thickness, t_w (mm)	Outer Diameter, D_o (mm)	Net Area, A_o (mm^2)	Porosity, φ
0DR-S-1 0DR-S-2	0	Steel	2.3	4.4	127.0	123.3	65%
20DR-S-1 20DR-S-2	20		4.2			221.6	59%
40DR-S	40		4.8			256.8	55%
0DR-A	0	Aluminum	2.5	5.2	125.0	152.6	65%
20DR-A	20		4.2			259.7	59%
40DR-A	40		4.9			305.8	55%

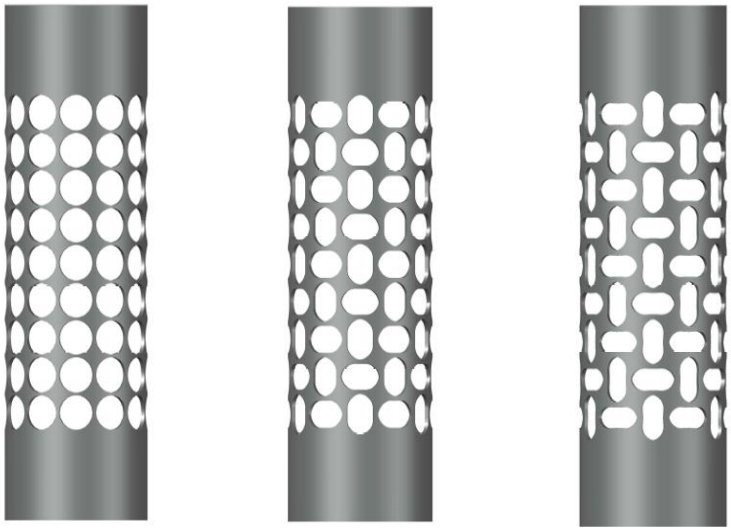

φ = 65%
a) 0DR

φ = 59%
b) 20DR

φ = 55%
c) 40DR

Figure 2.6: Final Specimen Designs.

To facilitate mounting into the test setup, top and bottom plates and stiffeners were welded to each tube specimens. The top and bottom plates were each *177.8 mm x 177. 8 mm × 12.7 mm* thick and composed of ASTM A36 grade steel or EN 6061 grade aluminum, depending on the tube base metal. The plates had four ϕ14.3 mm bolt holes located in the corners *25.4 mm* from each edge. The steel stiffeners were *25.4 mm x 50.8 mm*, made with *4.75 mm* thick A36 Steel. The aluminum stiffeners were *25.4 mm x 50.8 mm*, made with *6.35 mm* thick 6061 Aluminum. Figure 2.7 shows photographs of typical steel specimens as received and after welding.

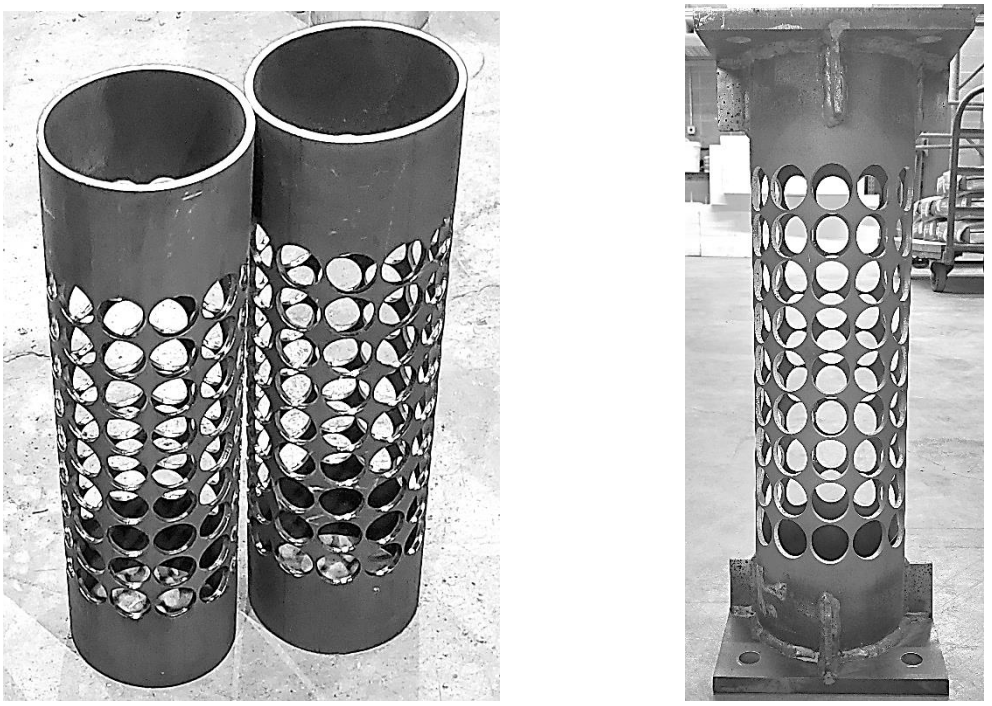

a) As received b) Prepared, unpainted

Figure 2.7: Photographs of a typical tubular specimens

2.4. Material Properties

The constitutive material properties of the steel and aluminum tubular specimens were determined using tensile tests performed on coupons extracted from the metal tubes. Coupons were prepared as shown in Figure 2.8 following Sec 6.9.2 of ASTM E8/E8M – 16a (ASTM Int'l 2016). Three replicates were tested for each base metal to establish the tensile stress-strain behavior. Monotonic testing was conducted following ASTM E8/E8M – 16a (ASTM Int'l 2016), with a constant crosshead displacement of *2 mm/min*. As the coupons possessed the same curvature as the tubes, the ends were flattened in a vice and smoothed using a belt sander to avoid slippage in the test machine grips. Digital image correlation was used to optically measure the axial strain in the gauge region.

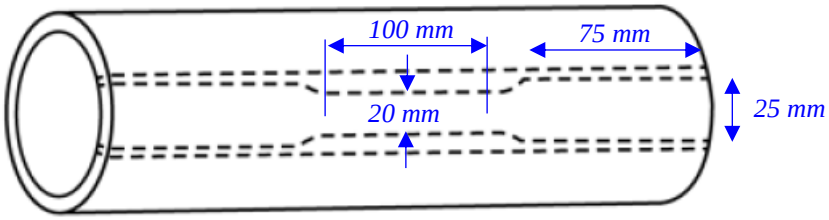

Figure 2.8: Geometry of tensile test coupons from large diameter tubes (ASTM Int'l 2016).

Figure 2.9 shows the measured engineering stress-strain behavior of the coupons. Table 2-2 and Table 2-3 summarize the results of the monotonic tensile tests for S355JR steel and 6060-T66 aluminum, respectively. The yield stress for steel was calculated based on the value of stress in yield plateau, while for aluminum the *0.2%* yield offset method was used.

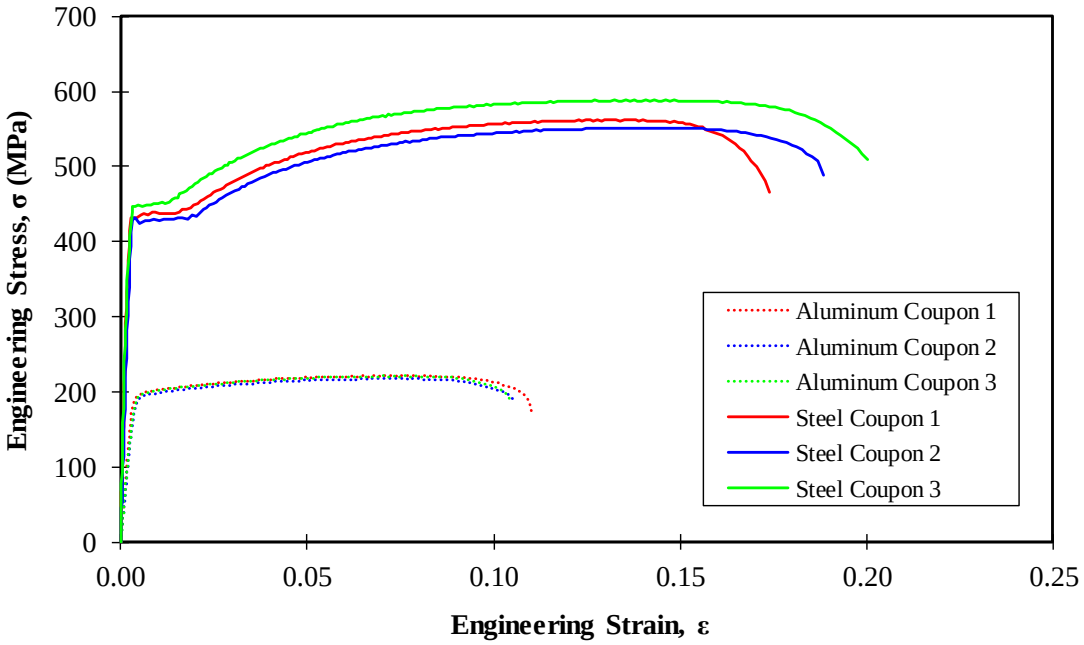

Figure 2.9: Engineering Stress-Strain data for S355JR Steel and 6060-T66 Aluminum.

Table 2-2: Coupon (Nominal) test results for S355JR Steel.

Coupon No.	Modulus (E), GPa	Yield Stress (σ_y), MPa	Failure Stress (σ_u), MPa	Final Elongation, (ε_u), %
1	213.6	431.3	562.4	17.4
2	160.0	432.4	551.8	18.8
3	232.5	446.5	588.7	20.0
Average	**202.1**	**436.8**	**567.6**	**18.8**

Table 2-3: Coupon (Nominal) test results for 6060-T66 Aluminum.

Coupon No.	Modulus (E), GPa	Yield Stress (σ_y), MPa	Ultimate Stress (σ_u), MPa	Final Elongation, (ε_u), %
1	60.3	197.1	221.2	11.0
2	51.2	193.7	217.4	10.6
3	55.0	196.6	220.9	10.4
Average	**55.5**	**195.5**	**219.8**	**10.7**

2.5. Test Setup

This section describes the specimen preparation, test assembly, instrumentation, load protocol, and test procedure.

2.5.1 Test Assembly

A custom mounting assembly, illustrated in Figure 2.10, was prepared to install the tubular specimens into the test machine. The mounting assembly consisted of *2 x 25.4 mm* thick A36 Steel plates, each attached to the base and crosshead of the MTS machine. The mounting plate at the bottom was welded to an *M36-2* threaded rod which screwed into the base of the MTS machine. The top mounting plate was bolted into the crosshead using an *M27-2* bolt. Both mounting plates were *177.8 mm x 177.8 mm* in plan with *4 x Ø12.7 mm* threaded bolt holes *25.4 mm* from each edge. The test assembly was designed such that each tubular specimen could be attached to the permanently attached mounting plates using *8 x 12.7 mm-13* ASTM A307 grade bolts and then removed after completion of each test.

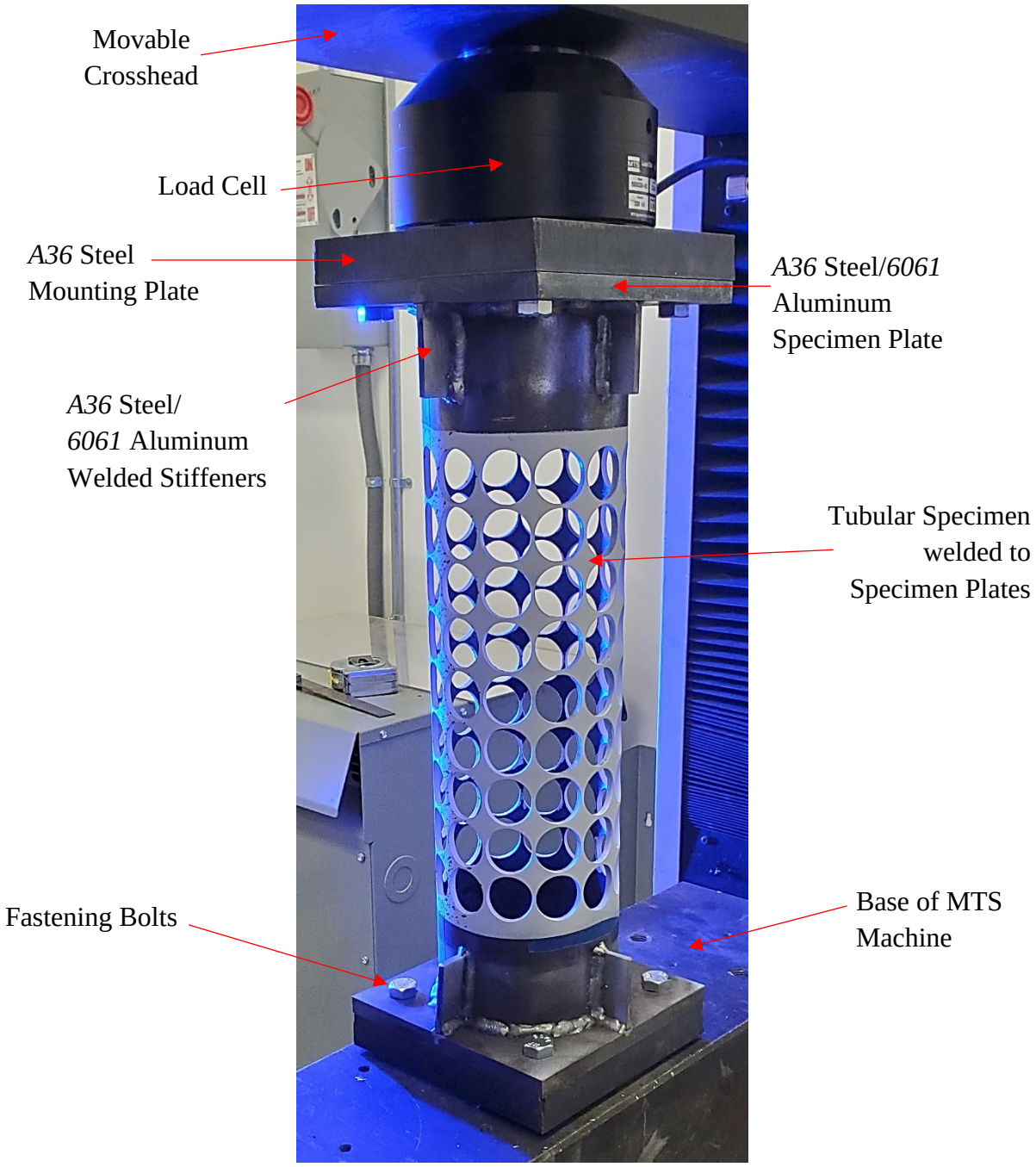

Figure 2.10: A typical tubular specimen mounted in the test fixture

2.5.2 Loading Protocol

To characterize their performance for potential application during extreme loads, such as earthquakes and blasts, most of the auxetic tubular specimens were subjected to the FEMA 461 (FEMA 2007) reversed-cyclic loading protocol. The loading protocol was defined based on the

expected yield (Δ_o) and maximum (Δ_m) displacements of the samples. As per FEMA 461, *6* cycles prior to yield corresponding to $0.25\Delta_0$, $0.5\Delta_0$, $0.75\Delta_0$ were included. Two cycles were recommended for each applied displacement increment with a *40%* increase between subsequent displacements after Δ_0.

Values of Δ_o and Δ_m used to generate the loading protocols were estimated based on preliminary FE analyses using elastic-perfect plastic stress-strain materials properties for steel on the specified yield strength. FE analysis was conducted for the steel geometries only and Δ_o was selected as the minimum yield displacement observed from all three DR geometries. Similarly, the maximum of all three predicted failure displacements was set as Δ_m. No FE analysis was conducted to predict these parameters for aluminum. Instead, an arbitrary value for Δ_o was selected while Δ_m was calculated by reducing the value for steel by the ratio of final elongations of aluminum and steel coupons.

Δ_0 values were *0.3 mm* and *0.5 mm* for steel and aluminum specimens, respectively. Similarly, maximum displacements Δ_m were *6.75 mm* and *4 mm* for steel and aluminum specimens, respectively. In case specimens did not fail at their maximum Δ_m values, displacement values were increased by a constant value $1.2\Delta_0$ every two cycles until failure was achieved. To mimic quasi-static loading conditions, a crosshead displacement of *0.3-1.2 mm/min* was adopted for all reverse-cyclic tests. Reverse-cyclic loading protocols for steel (Protocol S) and aluminum (Protocol A) specimens have been shown in Figure 2.11.

It was observed during testing that applied displacements defined in the loading protocols for steel did not translate to actual specimen displacements due to slack and deformation is the test assembly. While specimen displacements in compression were *60%* of applied compressive deformations on average, the measured tensile deformations were *35%* of the crosshead displacement on average. The differences in applied and actual displacements can be seen in Figure 2.11 for 0DR-S-1 and 20DR-A and testing details pertaining to the type and speed of tests have been presented in Table 2-4.

A single monotonic compressive test was also conducted to differentiate between cyclic behavior using specimen 20DR-S-2. For that test, a loading rate of *0.3 mm/min* was used. The

specimen was loaded to either failure or contact between opposing cell walls, whichever occurred first.

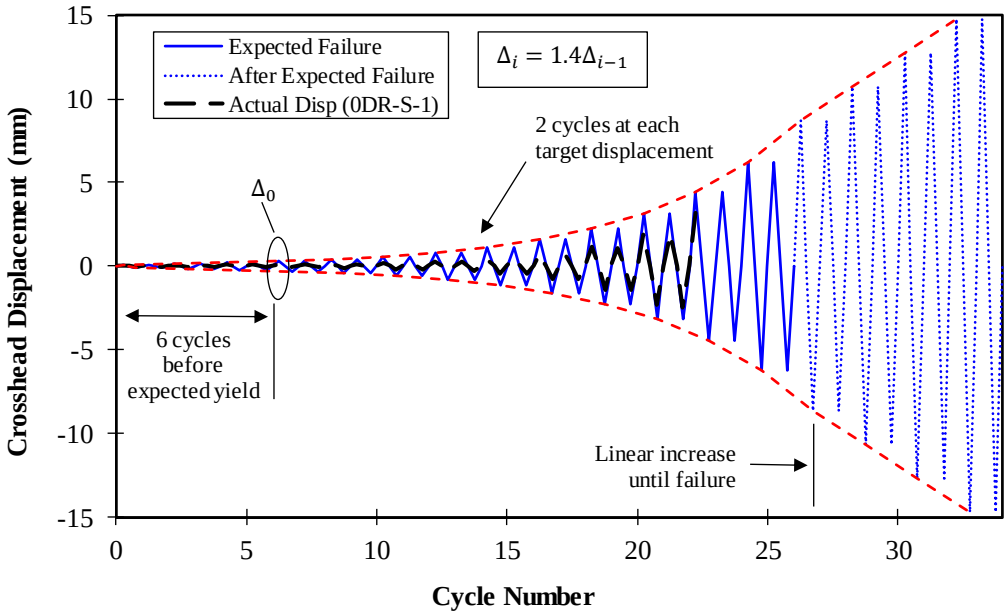

a) Steel specimens (Protocol S).

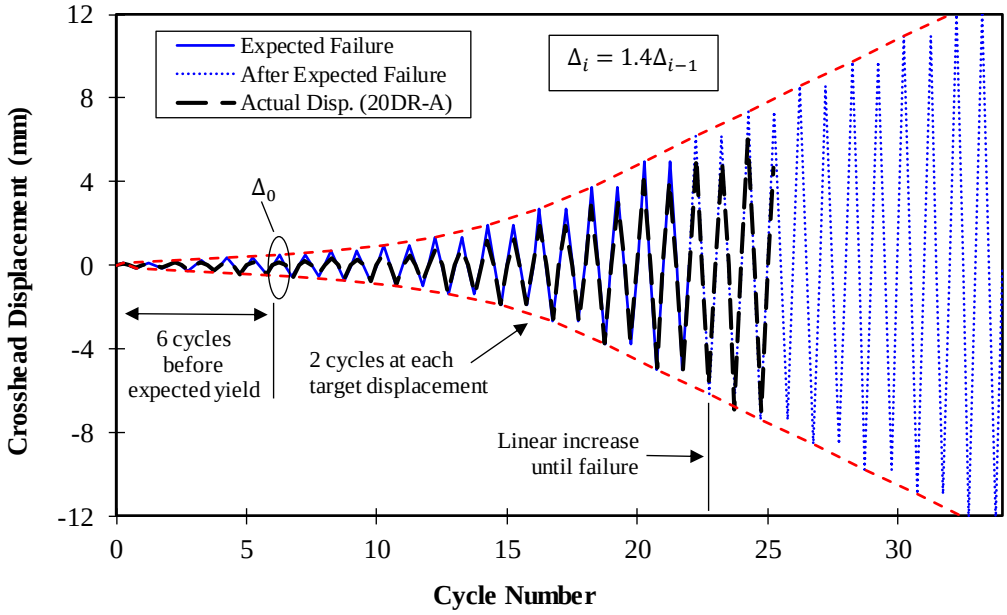

b) Aluminum specimens (Protocol A).

Figure 2.11: Reverse-cyclic loading protocols

Table 2-4: Testing Details for Specimens.

Designation	Loading Protocol	Strain Rate (min^{-1})	Crosshead Speed (mm/min)
0DR-S-1	Reverse cyclic: Protocol S	0.04	1.20
0DR-S-2 20DR-S-1 40DR-S		0.03	0.90
0DR-A 20DR-A	Reverse cyclic: Protocol A	0.02	0.60
40DR-A		0.03	0.90
20DR-S-2	Monotonic Compressive	0.01	0.30

2.5.3 Instrumentation

Reverse-cyclic tests were conducted using a double column MTS Insight Universal Testing Machine with a maximum tension/compression capacity of *33.75 kip* (*150 kN*). The MTS TestWorks4 software (MTS) was used to operate the MTS machine as well as acquire crosshead displacement and applied load data.

Digital image correlation (DIC) was used to measure the three-dimensional displacement field and strain distribution of the tubular specimens. The ARAMIS Adjustable 12M system (GOM n.d.) with two Schneider *25 mm* cameras was used for optical measurements. The cameras were mounted onto an "800 adjustable support system". A CP40/MV170 calibration plate was used to calibrate the equipment. Two additional DSLR Cameras (Canon EOS Rebel T6) were placed behind the test assembly to capture any additional deformation hidden from the DIC equipment. A time-lapse software was used to take incremental photos during testing. Figure 2.12 (a) shows the DIC camera arrangement and test setup.

A stochastic black speckle pattern was spray painted onto the specimens prior to testing. A typical specimen with speckle pattern is shown in Figure 2.12(b). Special care was taken to ensure only the outside surface of the tubes was painted. To this end, paper was taped to the inside of each specimen and removed prior to testing. To maximize contrast, a thin coat of flat protective enamel white paint was first sprayed onto the samples. The dense speckle pattern was then applied using

flat protective enamel black paint. A spraying technique was used to minimize droplet size while maintaining pattern density, ensuring a finer mesh to obtain localized data.

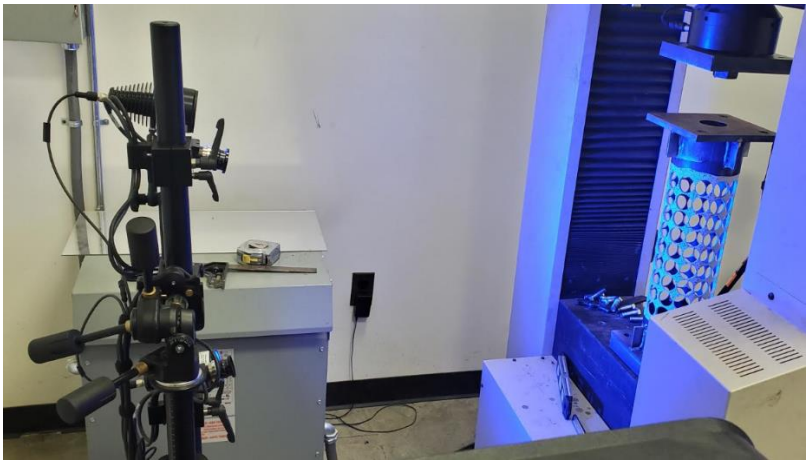

a) DIC equipment with test specimen

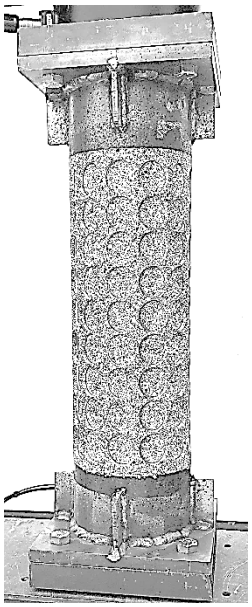

b) Typical specimen with stochastic pattern

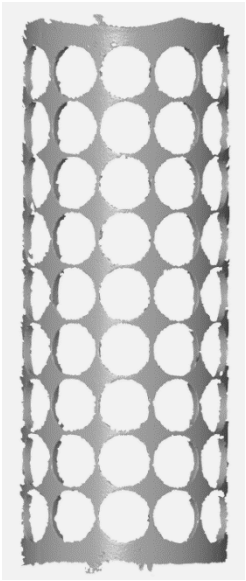

c) Typical 3D surface visible to the DIC system

Figure 2.12: Testing Arrangement and 3D surface.

The imaging equipment captured a test volume that was *380 mm* wide, *280 mm* tall and *240 mm* deep. The image acquisition setup was rotated vertically to maximize the portion of the captured volume containing the test specimen. The cameras were pointed towards the test specimen such that the line of sight was normal to the MTS machine. As the specimens were tubular, only half of the external surface area could be captured. A 3D surface rendering of 0DR-S-1 captured by the cameras is presented in Figure 2.12 (c). This surface was created for all

specimens analyzed for axial and radial deformations during the experiment using ARAMIS Professional 2019 (ARAMIS 2019).

2.5.4 Procedure

Preparation and testing of all tubular specimens followed a nominally identical procedure. The edges of all specimens were first filed to remove excess material and slag generated during the laser cutter process. The specimens were then degreased with acetone subsequently. Specimens and their corresponding end plates were marked and aligned for welding. Endplates and stiffeners were welded to the specimens using a Metal Inert Gas (MIG) welding process. Bending was observed in the mounting plates due to high heat produced by welding. However, the gap produced by the bent plates was minimized by tightening the bolts during final assembly. Slag produced by welding was removed and endplates were ground down to ensure a flat surface. A sheet of paper was then attached to the inside of each specimen before applying two coats of white paint. Subsequently, a speckle pattern was sprayed onto the area of interest. Details of painting and speckling have been provided in Section 2.5.3.

Before conducting each test, the calibration of the DIC equipment was performed and verified. The calibrated DIC apparatus was placed at the desired distance from the MTS testing assembly. Each tubular specimen was initially placed on the mounting plates and an image was taken using ARAMIS Professional 2019 software to ensure that the DIC equipment was capturing the desired surface. A 3D surface component was prepared using that individual photo to check pattern quality and intersection deviation between the two cameras. A deviation typically lower than *0.03* was required to ensure accuracy of the 3D data. Suitable facet size and distance between facets was selected such that a maximum surface area was captured while maintaining a continuous surface. A typical facet size of *12* pixels was targeted with a distance of *6-8* pixels. If the speckle pattern was found to be unsatisfactory, the surface of the specimens was sandblasted and repainted. Once the desired pattern quality and intersection deviation was achieved, the paper was removed from inside the finalized specimen.

The final specimens were then bolted onto the custom-made test assembly. First, the bottom specimen plate was aligned and bolted to the bottom mounting plate; bolts were not fully tightened at this stage to allow for some rotation in the specimen. Next, the MTS crosshead was

brought down gradually, and the top plates were bolted together after ensuring proper vertical alignment. All bolts were tightened while manually adjusting the crosshead to minimize loading on the specimen. Bolts were tightened such that the gap between each mounting plate and specimen plate was kept to a minimum. A perfect vertical alignment of each specimen was checked to avoid unwanted rotation, ensuring fully axial loading.

The cyclic loading protocols were coded into TestWorks4 software for actuating the MTS crosshead. The loading sequence was divided into 3 to 4 loading phases since the DIC software was limited to taking batches of *1000* photographs at a time. The loading was paused at the end of each phase, then DIC photos were saved, and the loading then resumed. The additional cameras were programmed such that they took photographs simultaneously with the DIC cameras for a given recording interval. Load (in Newtons) and cross-head displacement (in mm) were output from the MTS machine into DIC system.

The cyclic tests were terminated when either the base tubular material ruptured or if opposite cell walls contacted each other. No break detection routine was used in the MTS software, thus each experiment had to be manually terminated upon meeting either failure criteria. The experimental data obtained from the MTS machine, DIC equipment and cameras then were saved for post-processing.

Post-processing of experimental data was conducted using ARAMIS Professional 2019 software. To reduce processing time, raw files containing all the captured frames from the DIC apparatus were thinned down such that every $4^{th}/5^{th}$ frame was processed. These 'thinned' files were then processed. A custom alignment was created to orient the specimen along a global axis. Deformation data was then extracted from the created surface. A 3D surface of the specimen was first created using a facet size and facet distance which would maximize surface area as well as a finer mess. Data was processed in order to extract required deformation data (described in Section 1.1). The required data was then exported to a '.csv' file which was further processed into desired response parameters using Microsoft Excel. Details of the data analysis using the processed Excel files are presented in Chapter 3.

Chapter 3. Experimental Results

3.1. General

This chapter presents and compares the results for the eight auxetic and non-auxetic tubular specimens. The response of the tubes in terms of load-deformation, Poisson's ratio, deformed shape, energy dissipation, and failure mode is discussed. Section 3.2 provides an overall summary of the results, Section 3.4 provides an overview of the data analysis, and Sections 3.4 to 3.11 summarize the response of each individual tube.

3.2. Summary of Results

Overall summaries of the test results of the auxetic and non-auxetic tubes are listed in Table 3-1. Load-deformation characteristics have been described using maximum load, stress and strain for each tested specimen; negative values correspond to compression. Peak stress is defined as the peak load divided by the effective cross-sectional area (A_0). Maximum average vertical strain (ε_A), measured over the gauge length of the tubes, are displayed for tension and compression cycles to demonstrate effective strain range under reverse uniaxial loading. The angular rotation of a unit cell (θ_c^{exp}) about its geometric centroid at peak tensile load was extracted during post-processing. Failure in the tubes is illustrated via the observed failure mode and the loading cycle in while failure occurred.

The observed Tube Poisson's Ratio (v_T) behavior, based on the mid-height radial strain (ε_R) and average vertical strain (ε_A), specifies whether auxeticity was observed in the specimens. Average values for v_T calculated before yield and final values at failure are presented. The tubular Poisson's ratio does not describe the deformation of individual cells, rather it is a measure of the global response of the cellular pattern. Therefore, auxeticity of the tubes is defined by the global tube deformations rather than changes in individual cell geometry. Lastly, the energy absorption of each specimen, has been computed and normalized in two different ways. The Areal Specific Energy Absorption (ASEA) is calculated by normalizing total energy absorbed by areal mass, thereby highlighting the effects of the topology only. Similarly, Specific Energy Absorption (SEA) is calculated by normalizing total energy by specimen volume to include effect of base metal.

Table 3-1: Summary of experimental results obtained from ductile metal auxetic tube tests.

	Compression		Tension									
Specimen	**Peak Strain ε_A (%)**	**Peak Load (kN)**	**Peak Strain ε_A (%)**	**Peak Load (kN)**	**Angle θ_c^{exp} (deg)**	**Tube Poisson's Ratio ν_T**		**SEA (J/mm^3)**	**ASEA (MJ.m^2/kg)**	**Failure Cycle #**	**Failure Mode**	**Loading Protocol**
						Pre-yield	**Post-yield**					
0DR-S-1	-0.36	-70.2	0.71	75.6	0	0.25	0.66	374	2.13	23	Tensile Rupture	Reverse cyclic
0DR-S-2	-0.71	-68.2	0.45	75.2	0	-1.00	1.36	386	2.19	23	Tensile Rupture	Reverse cyclic
20DR-S-1	-1.51	-76.1	0.90	100.2	2.49	0.00	-1.42	957	6.38	27	Tensile Rupture	Reverse cyclic
40DR-S	-1.54	-66.6	1.82	78.0	3.57	-2.00	-2.00	1129	8.25	28	Tensile Rupture	Reverse cyclic
0DR-A	-0.21	-19.6	0.49	21.2	0	-0.56	1.72	136	2.19	18	Tensile Rupture	Reverse cyclic
20DR-A	0.15	-26.1	1.27	32.0	0.97	-1.48	-1.87	416	7.88	26	Tensile Rupture	Reverse cyclic
40DR-A	0.56	-26.0	1.74	32.2	2.89	-2.22	-2.76	393	8.17	28	Tensile Rupture	Reverse cyclic
20DR-S-2	-1.54	-72.6	-	-	-	-2.62	-1.77	-	-	-	Cell Wall Contact	Monotonic Comp.

3.3. Data Analysis

The raw data obtained from the experiments consisted of applied load and the three-dimensional measurements of specimen deformations using digital image correlation. This data was processed to extract vertical and radial strains, various definitions of Poisson's ratio (v), specific energy absorption, and load-deformation response for all experiments conducted.

The term "Poisson's Ratio" has been used in this thesis to describe global structural deformations of the tubular specimens. While this use of the term deviates from the material-level definition of Poisson's Ratio, the seminal papers on auxetic structures have adopted the terminology to describe structural level deformations as well. Influential works (Lakes 1987; Evans 1991; Alderson and Evans 1991) refer to the deformation response of Auxetic structures as "Poisson's ratio". Additionally, when studying tubular auxetics, Ren et al. (2016) employed the term "Poisson's ratio" to quantify the observed deformations.

A three-dimensional cartesian coordinate system adopted to facilitate data analysis. The XZ axes define a plane transecting the tube cross-section and the Y axis was oriented along the length of the specimen. The region of interest for data analysis was the portion of the auxetic topology visible to the DIC system over a vertical gauge length (H_g) of *317.5mm*. All tubular specimens were divided into *19* integrations slices ($Y_1 \dots Y_{19}$) across which deformation data was collected. Specimens were also divided into *9* vertical layers ($L_1 \dots L_9$), with each layer corresponding with the centerline of a row of cells. Figure 3.1 (a) shows the cartesian coordinate system and discretization of the tube into horizontal layers and integration slices for a typical specimen. The black dots represented points at which deformations were obtained from DIC measurements for data analysis.

For a material subjected to an axial stress below its proportional limit, ASTM E132-17 (ASTM Int'l 2017) defines Poisson's ratio (v) as "the negative of the ratio of transverse strain to the corresponding axial strain". However, for cyclic loading where axial stresses surpass the proportional limit, the calculation of Poisson's ratio using this definition yields bizarre and inconsistent results, as shown by Perry et al. (2005). This inconsistency in calculated Poisson's ratio was resolved by Chakrabarty (2012) who proposed a new incremental approach where change in radial and axial strains were used to calculate Poisson's ratio; results using this new approach

demonstrated a consistent average Poisson's ratio value. To obtain a similar consistency in results, this incremental approach is also employed in this study. Poisson's ratio is calculated using deformations measured over strain increments, measured between points of peak tensile and compressive strain in a given cycle.

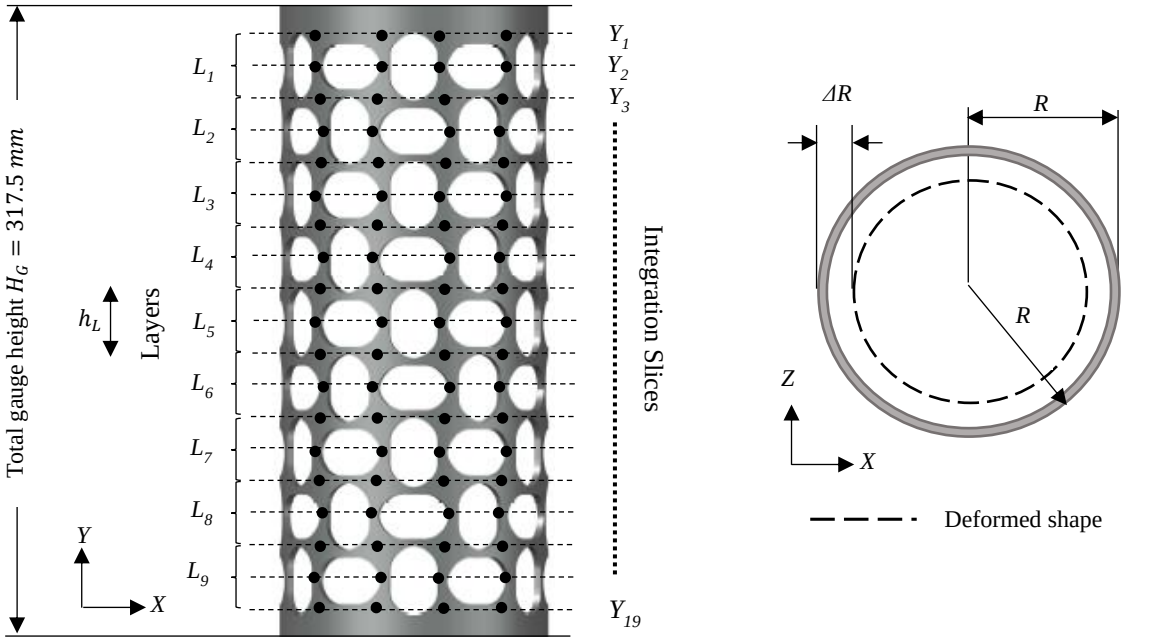

a) Elevation view b) Plan view

Figure 3.1: Coordinate system and discretization for tubular specimens

Effective Poisson's ratio was defined as the negative ratio between radial strains and axial strains in the tubes. Two effective Poisson's ratios were calculated; Tube (v_T) and mid-height layer (v_{MH}). Tube Poisson's Ratio (v_T) was a ratio of the axial deformation to the radial deformation observed in the entire tube. The deformations of individual cells were not accounted for, instead it was used to gauge the holistic mode of deformation for a given specimen. Mid-height layer Poisson's Ratio (v_{MH}) was the ratio of axial and radial deformation encountered in just the mid-height layer L_5. It accounted for cell deformations in a given layer, was used to quantify local response of a representative cell layer in a specimen. While inter-related, the Poisson's ratios had different values for each specimen.

Mid-height layer Poisson's ratio (v_{MH}), was calculated for a strain increment using the following equation,

$$v_{MH} = -\frac{\Delta\varepsilon_R}{\Delta\varepsilon_{AL}} = -\frac{(\Delta R_f - \Delta R_i)/R}{(\Delta h_{Lf} - \Delta h_{Li})/h_L} \quad (3)$$

where $\Delta\varepsilon_R$ and $\Delta\varepsilon_{AL}$ represent mid-height radial and layer vertical strains. Meanwhile, f and i represent the final and initial values in a strain increment.

Similarly, Tube Poisson's Ratio (v_T), was calculated using radial strain (ε_R) and average vertical strain (ε_A) at each strain increment. The following equation was used,

$$v_T = -\frac{\Delta\varepsilon_R}{\Delta\varepsilon_A} = -\frac{(\Delta R_f - \Delta R_i)/R}{(\Delta H_{Gf} - \Delta H_{Gi})/H_G}\ , \quad (4)$$

where f and i represent the final and initial points in a strain increment.

Radial strain (ε_R) was defined as the total change in radius (ΔR) of the tube at mid-height layer L_5 (Figure 3.1 (a)) at any time, with respect to the original outer radius (R). The specified layer was chosen as it had minimum boundary effects. As radial deformation data could not be directly recorded by the DIC apparatus, the radial components were calculated using a simple function in ARAMIS Professional which calculated radial displacements using the following equation,

$$\Delta R = \sqrt{(\Delta Z)^2 + (\Delta X)^2} \quad (5)$$

Where ΔR was the change in radius of the tube at each point while ΔX and ΔZ were the two orthogonal horizontal components of deformation, as shown in Figure 3.1 (b).

Two variations of vertical strains were computed: average (ε_A) and layer (ε_{AL}). Average vertical strain (ε_A) was defined as the ratio of the change in gauge height (ΔH_G), to the original gauge height (H_G). Layer vertical strain (ε_{AL}) was defined as the change in height (Δh_L) between slices Y_{11} and Y_9, divided by the original layer height (h_L). The height h_L is labelled on Figure 3.1 (a).

Net effective cross-sectional area (A_0) was used to calculate axial stress for the specimens; measured at the vertical height where least material was present. For calculating strain rate for loading, a gauge length of *30 mm* was selected, which corresponded- approximately- to the vertical height of each cell layer.

Axial load versus average vertical strain curves were plotted for each test. Points on the curves corresponding to yielding in tension and compression were visually identified at the first instance where the slope of the curves became non-linear. These points corresponded to the first instance of local yielding in individual cell walls rather than the apparent global yielding of the tubes.

3.4. Specimen 0DR-S-1

Specimen 0DR-S-1 was the steel control specimen containing an array of circular voids designed to exhibit positive Poisson's ratio behavior. Photographs of 0DR-S-1 before, during, and after testing are shown in Figure 3.2.

a) Unpainted prepared specimen

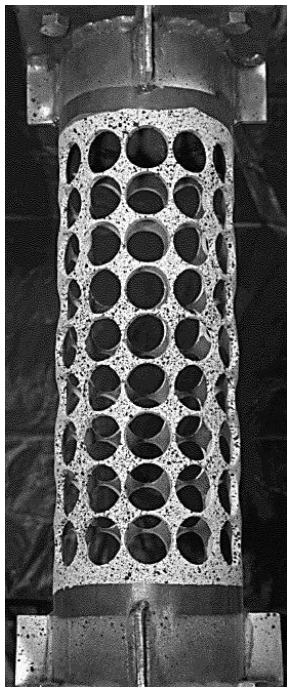

b) Localized deformations in layers under compression

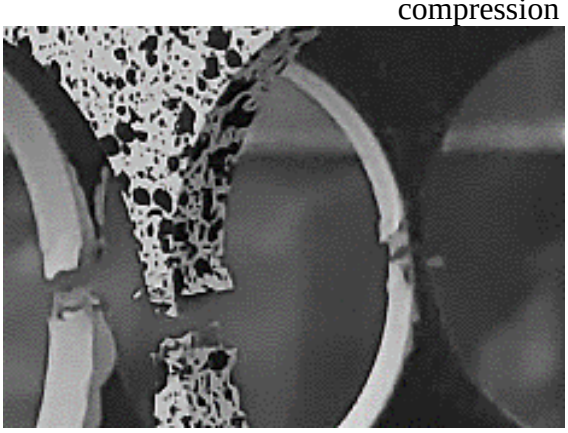

c) Tensile fracture of the cell walls in Layer L9

Figure 3.2: Photographs of Specimen 0DR-S-1.

Specimen 0DR-S-1 failed in the tension leg of the 23^{rd} cycle at a load of *75.6 kN* and an axial deformation of *2.24 mm*. Value for strain ε_A at peak tension was *0.71%*. To verify how the

axial strength of the tube compared to the coupon tests, the peak load was divided by the effective cross-sectional area. A peak tensile stress value of *613 MPa* was obtained which was within *8%* of the ultimate coupon strength.

The specimen displayed clear positive Poisson's ratio behavior visible to the naked eye with radial expansion of the tube under compressive loading, as shown in Figure 3.2 (b). NPR behavior in tension (radial expansion) was not obvious, but was present and confirmed after examining the processed deformation data. Tensile rupture of the cell walls (Figure 3.2 (c)) was observed in layer L_9 which propagated through five cell walls before loading was halted. Significant rotation of the base plate was observed at failure due to the eccentric nature of the loading caused by asymmetric rupture of cell walls. The failed sample was unloaded and a residual crosshead deformation of *2.53mm* was recorded. However, the residual displacement field of the unloaded specimen was not captured by the DIC apparatus.

Figure 3.3 (a) shows the hysteretic load-strain response of the tube under cyclic loading. The elastic slopes for tension and compression are similar, with tension yielding occurring at *35.7 kN* compared to a compression yielding load of *-48.9 kN*. Significant strain hardening was observed in tension defined by the positive slope of the diagram. In contrast, no noteworthy hardening is present in compression loading due to the out-of-plane deformations of cell walls. The unloading slopes of the diagram are consistent. The specimen experienced greater compression deformations than tensile deformations for the same crosshead displacement due to slack in the test assembly.

Figure 3.3 (b) shows the variation in radial strain (ε_R) with average vertical strain (ε_A) for mid-height layer L_5. The slope of the curves remains flat before yielding. The onset of yielding leads to an increase in slope before reaching a constant value. In a given loading cycle, the slope of the diagram is consistent for tension and compression, indicating the consistency in the deformation mechanism. The figure shows that a permanent radial expansion of the tube takes place as the final radial strain has a positive value. The negative slope of the graph is representative of the Tube Poisson's Ratio (v_T), which remains positive for each loading cycle, irrespective of the residual radial deformation. It can be concluded that a positive Poisson's ratio behavior is exhibited.

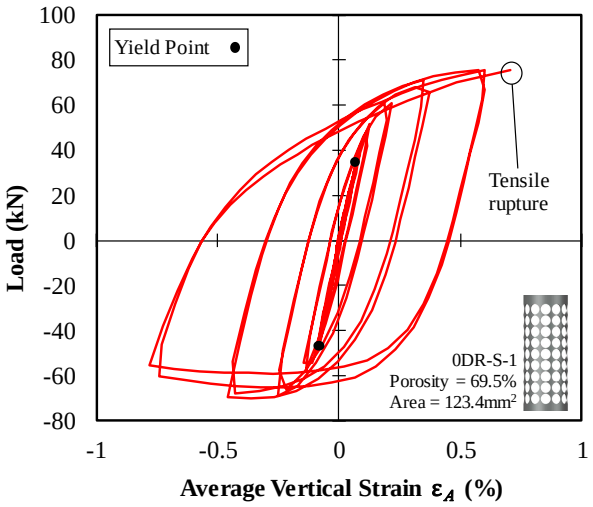

(a) Load vs. average vertical strain (ε_A)

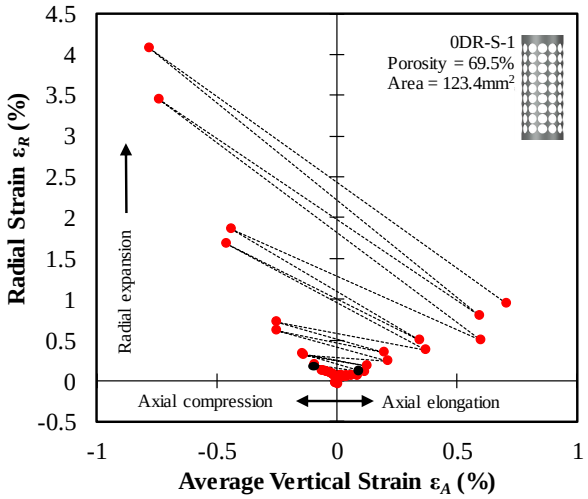

(b) Radial strain (ε_R) vs. average vertical strain (ε_A)

Figure 3.3: Specimen 0DR-S-1 deformation data.

Poisson's ratios, v_L and v_T, presented in Figure 3.4 for layer L_5 confirmed the non-auxetic nature of 0DR-S-1. Excluding the initial three cycles, the measured response of 0DR-S-1 demonstrated positive Poisson's ratio behavior. However, clear positive values are observed after yielding occurred in the 14th loading cycle. Before yielding, v_T was constant at a value of *0.2* and a significant rise was observed after yielding, to a value of *0.75*. This drastic shift may be attributed to formation of plastic hinges in the cell walls.

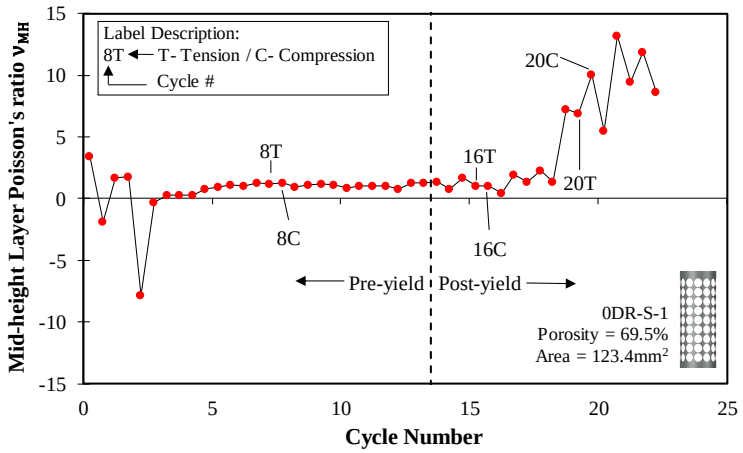

a) Mid-height Layer Poisson's ratio v_{MH}

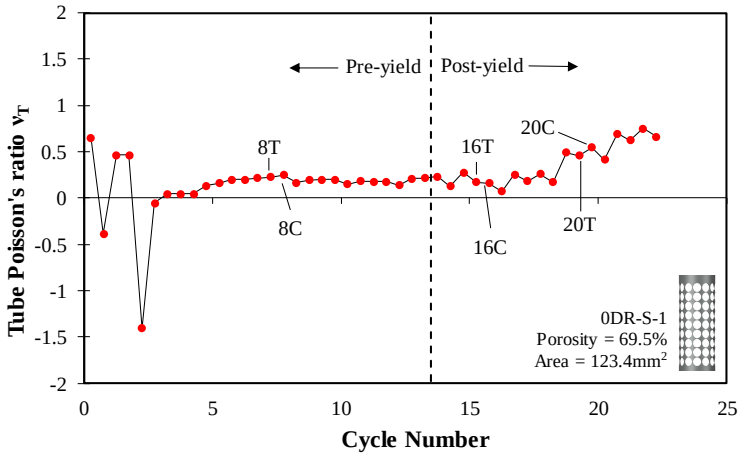

b) Tube Poisson's Ratio v_T

Figure 3.4: v_{MH} and v_T for specimen 0DR-S-1.

Figure 3.5 shows the radial deformations in 0DR-S-1 during tension and compression loading measured at the 8th, 16th, 20th, and final cycle before failure. It was observed that radial deformations were greater in compression than in tension. In tension, deformations were more uniform along the height of the tube. Deformations under compression were concentrated in the cell walls, which show local instability in cell layers with a sinusoidal deformed shape of the tube. Radial deformations were highest in layers L_5 and L_7 in the compressive cycle prior to failure.

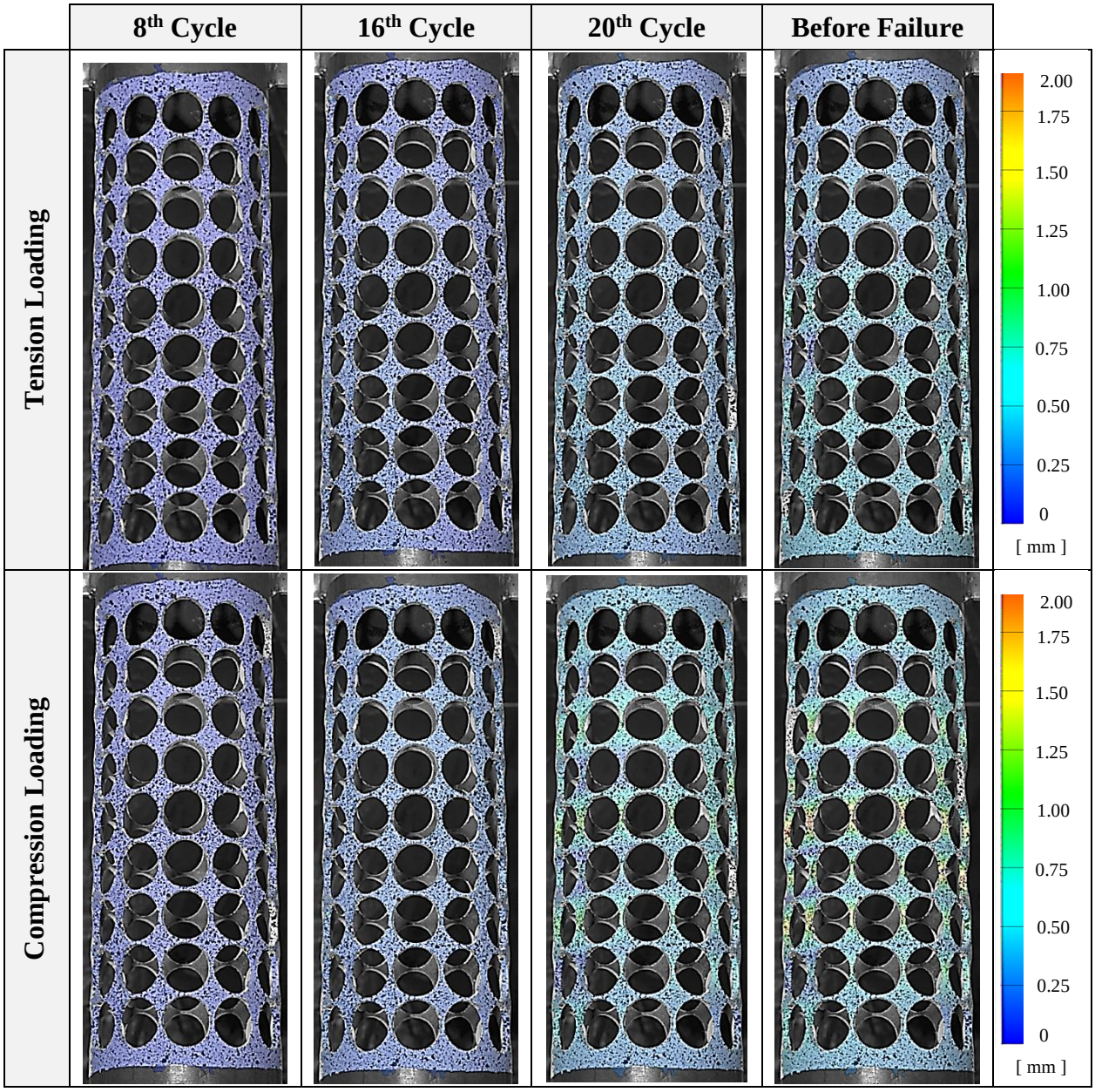

Figure 3.5: Radial Displacements in Specimen 0DR-S-1.

3.5. Specimen 0DR-S-2

Specimen 0DR-S-2 was the second steel control specimen designed to exhibit positive Poisson's ratio behavior. Figure 3.6 shows the specimen before and after testing.

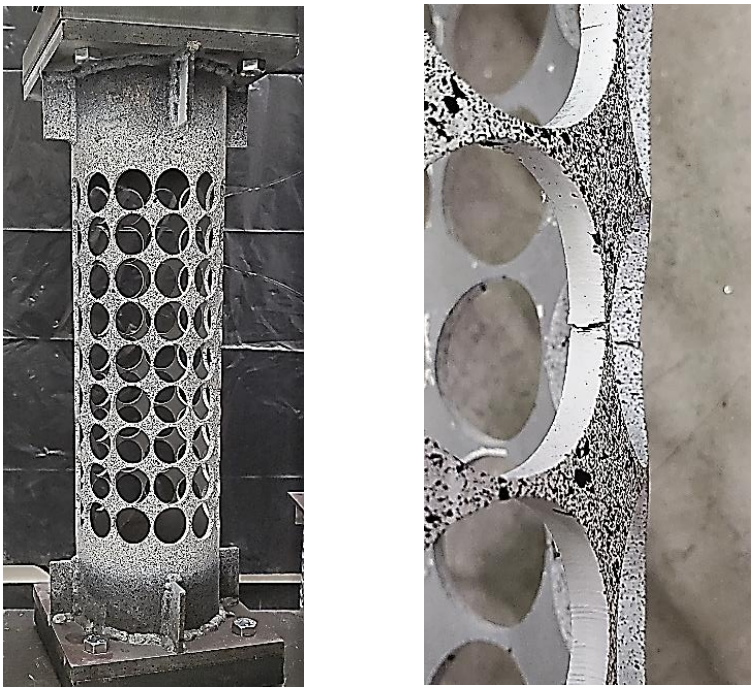

a) Prepared specimen

b) Tensile failure in cell wall in Layer L_6

Figure 3.6: Photographs of Specimen 0DR-S-2.

Specimen 0DR-S-2 failed in the tension leg of the *23th* cycle at a load of *67 kN* and an axial deformation of *0.90 mm*. Average vertical strain ε_A at peak tension was *0.45%*. Calculated axial stress at peak tension was *610 MPa*; similar to the ultimate stress measured in the coupon tests. While radial expansion could not be seen during the experiment, post-processing data confirmed that radial contraction occurred in layer L_5. Tensile rupture of the cell walls (Figure 3.6 (b)) was observed in layer L_6 which propagated through two cell walls before loading was halted. The failed sample was unloaded and a residual crosshead deformation of *1.78 mm* was recorded.

Figure 3.7 (a) shows the hysteretic load-strain response of the tube under cyclic loading. The elastic slope for tension was steeper than compression. Tension yielding occurs at *31.7 kN* compared to a compression yielding load of *-42.5 kN*. Strain hardening is observed in tension, depicted by the positive slope of the diagram. However, in compression, no significant strain

hardening is observed due to the out-of-plane deformations of cell walls. The unloading slopes of the diagram remain consistent until the final loading cycle where damage accumulation is likely to have caused softening. The specimen experienced greater compression deformations than tensile deformations for the same crosshead displacement due to slack in the test assembly.

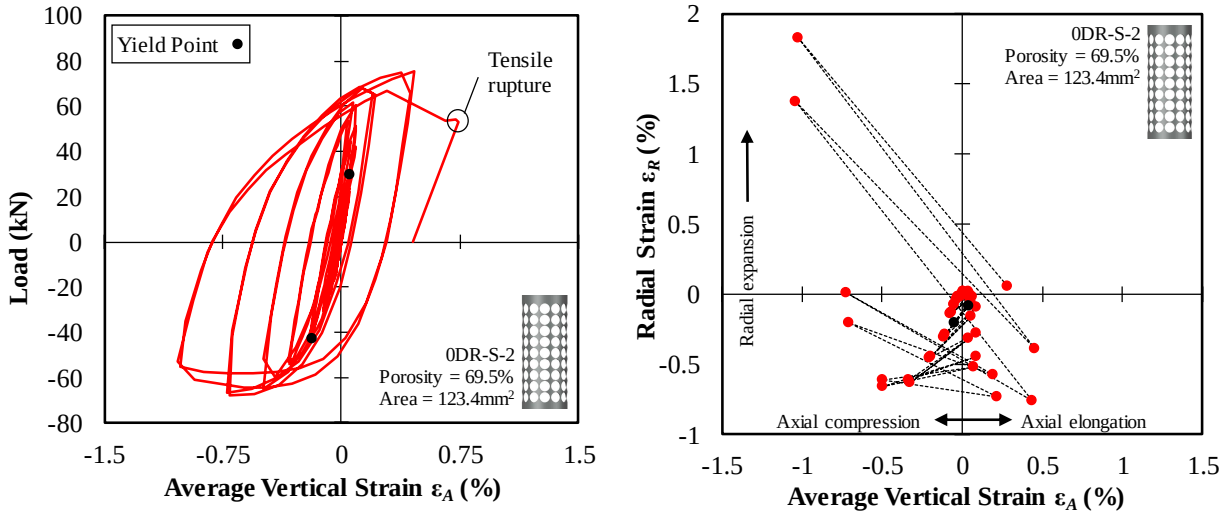

(a) Load vs. average vertical strain (ε_A)

(b) Radial strain (ε_R) vs. average vertical strain (ε_A)

Figure 3.7: Specimen 0DR-S-2 deformation data.

Figure 3.7 (b) shows the variation in radial strain (ε_R) with average vertical strain (ε_A) for mid-height layer L_5. The slope of the curves is positive before yielding but gradually shifts to a consistent negative value after yielding. In a given loading cycle, the slope of the diagram is similar for tension and compression showing that the deformation mechanism was independent of the nature of loading. The figure also shows that a permanent radial expansion of the tube takes place as the final radial strain has a positive value. There appeared to be a radial contraction at mid height during the earlier cycles which was possibly caused by an initial inward wave-like deformed shape. However, final cycles shifted towards a permanent radial expansion layer L_5, likely due to a shift in deformed shape. The tube demonstrated positive Poisson's ratio behavior as the negative slope of the incremental line, which represents the Poisson's ratio, was observed to be positive in the final cycles.

Poisson's ratios, v_L and v_T, are presented in Figure 3.8. Yielding was detected in the 14^h loading cycle. Both instances showed that values for v_L and v_T took constant values of *-2.5* and -

1, respectively, up to yielding after which a drastic rise was seen to *7* and *1.5*, respectively. Plastic deformation was the probable cause of this change in behavior.

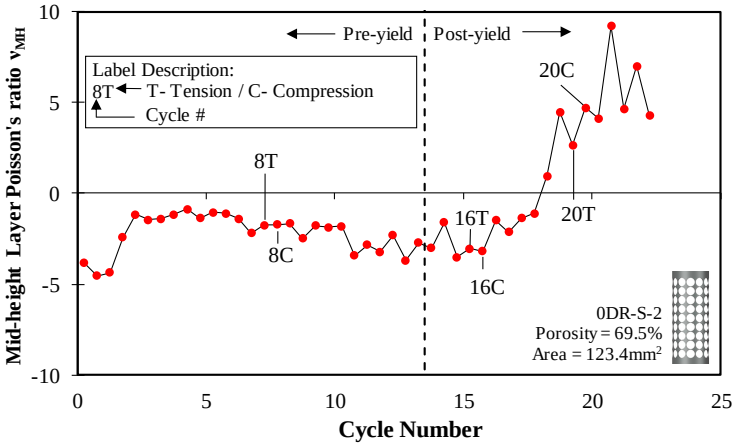

a) Mid-height Layer Poisson's ratio v_{MH}

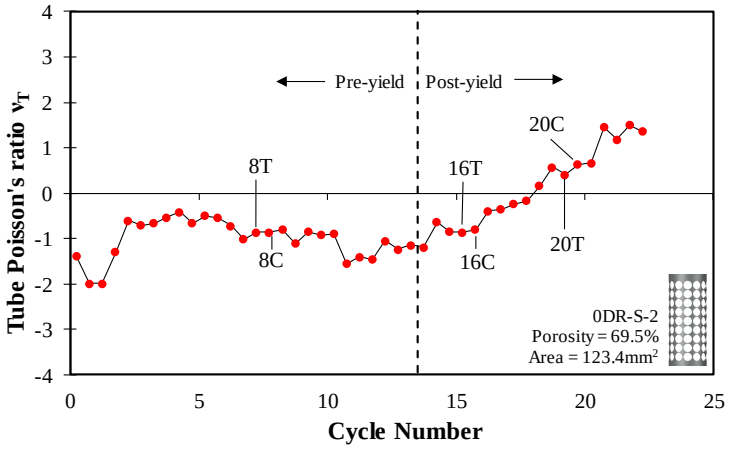

b) Tube Poisson's Ratio v_T

Figure 3.8: v_{MH} and **v_T** in Specimen 0DR-S-2.

A visual comparison between radial deformations measured during the experiment (Figure 3.9) shows that deformations were greater during compressive loading than tensile loading. Deformations were distributed uniformly along the height of the tube in tension, while concentration in cell walls was seen in compressive loading cycles, especially post-yield. Radial deformations were highest in layers L_4 and L_6 prior to failure and the tube displayed an instability with a sinusoidal deformed shape, similar to specimen 0DR-S-1. Ultimately, tensile rupture occurred in layer L_6.

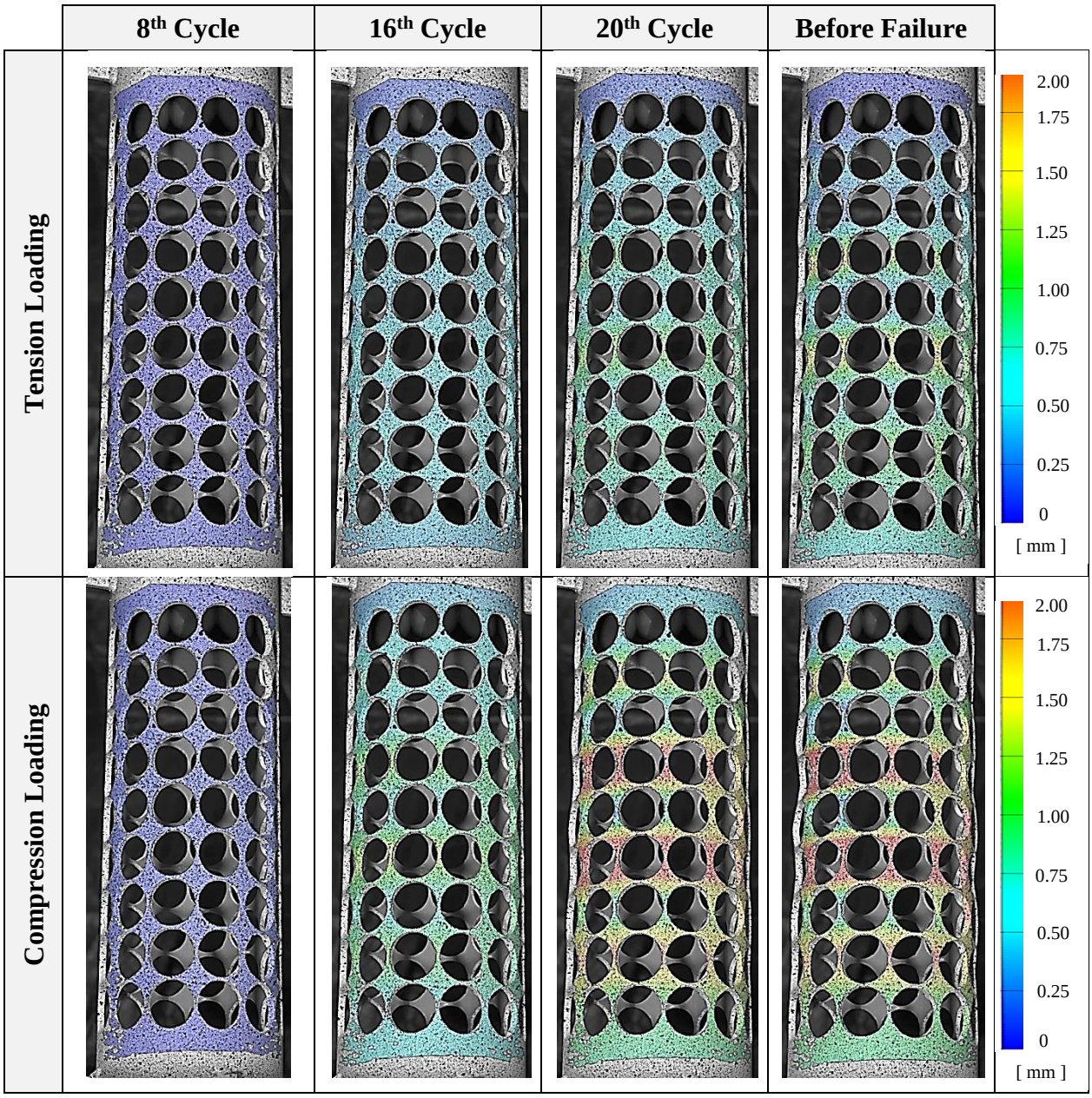

Figure 3.9: Radial Displacements in Specimen 0DR-S-2.

3.6. Specimen 20DR-S-1

Specimen 20DR-S-1 was the steel specimen designed to be auxetic due to the geometry of cells. Photographs of the specimen before testing and after failure are presented in Figure 3.10.

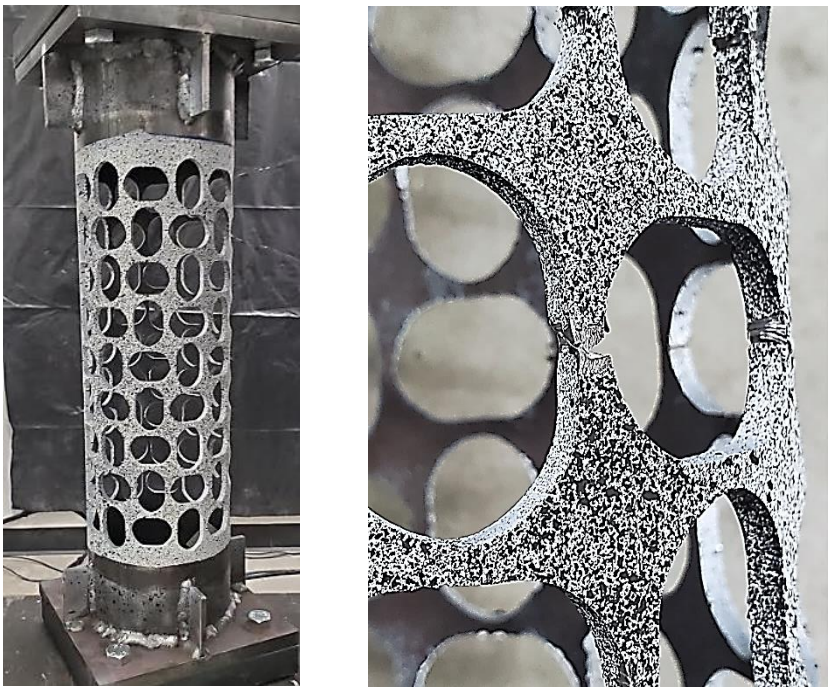

a) Prepared specimen

b) Tensile failure in cell wall in Layer L_6

Figure 3.10: Photographs of Specimen 20DR-S-1.

Testing was conducted in two parts as there was a weld failure in the bottom mounting plate during the 23^{rd} loading cycle in tension. The experiment was continued, until failure, from the same crosshead displacement at which weld failure occurred. Specimen 20DR-S-1 failed in the tension leg of the 27^{th} cycle at a load of *81.4 kN* and an axial deformation of *2 mm*. Peak tension load occurred at *0.90%* average vertical strain ε_A.

Radial contraction and expansion were not visually apparent during the test and only the change of shape of cells could be observed; cells contracted under compression and dilated under tension. Tensile rupture of the cell walls (Figure 3.10 (b)) was observed in layer L_6 which propagated through four cell walls before loading was halted. The failed sample was unloaded and a residual axial deformation of *3.56 mm* was recorded.

The hysteretic load-strain response of the tube under cyclic loading is presented in Figure 3.11 (a). The elastic slope was consistent for compression and tension but, tension yielding occurred at *31.1 kN* as opposed to compression yielding at *-38.4 kN*. Strain hardening was observed in tension but was not as significant in compression due to the geometrically induced buckling in the tube. Unloading slopes were consistent throughout the experiment. The response was highly un-symmetric in tension and compression. As the weld in the bottom mounting plate was weak, it was likely that significant deformation in the weld did not allow the full transfer of crosshead displacements to the sample during tensile loading.

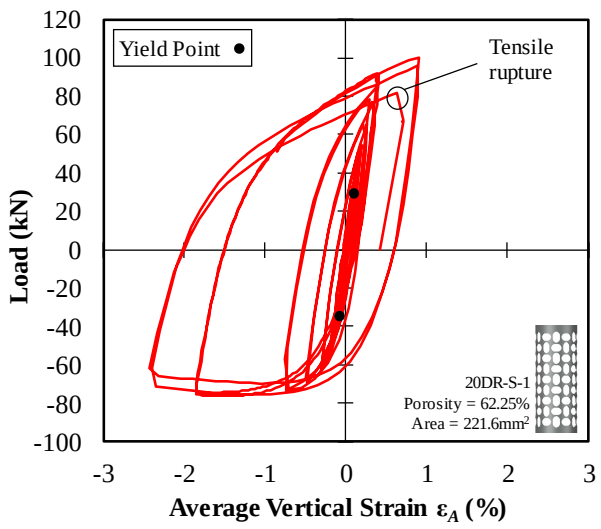

(a) Load vs. average vertical strain (ε_A)

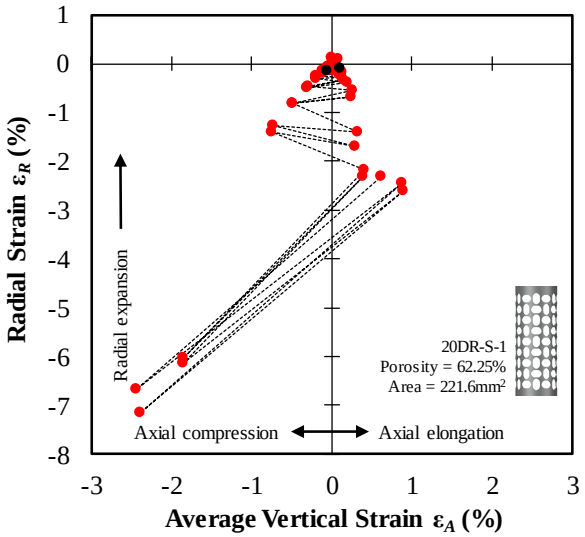

(b) Radial strain (ε_R) vs. average vertical strain (ε_A)

Figure 3.11: Specimen 20DR-S-1 deformation data.

The variation in radial strain (ε_R) with average vertical strain (ε_A) for mid-height layer L_5 is shown in Figure 3.11 (b). The negative value of slope figure is representative of Poisson's ratio (ν_T). A hybrid Poisson's ratio behavior was detected, with initial cycles showing PPR and final cycles demonstrating NPR. A sudden shift from a negative slope to positive was observed which then attained a consistent value. The initial negative slope can be attributed to a dominant localized buckling which was ultimately overshadowed by the global inward deformation of the tube at high axial strains. Slopes of the diagram were consistent, irrespective of compressive or tensile loading. A residual radial contraction was observed in the tube.

Figure 3.12 presents Poisson's ratios, v_L and v_T and confirms the hybrid nature. The specimen yielded in the *14th* cycle and exhibited an average zero value for both PR's prior to yielding. A stabilization effect was seen post yield, with both PR values displaying an average value of *0*. A sudden shift was seen in the *23rd* cycle where the values of v_L and v_T shifted to a consistent average value of *-2.25* and *-1.5*, respectively. Increased plastic deformations and an increase in the global buckling of the tube most likely contributed towards this shift.

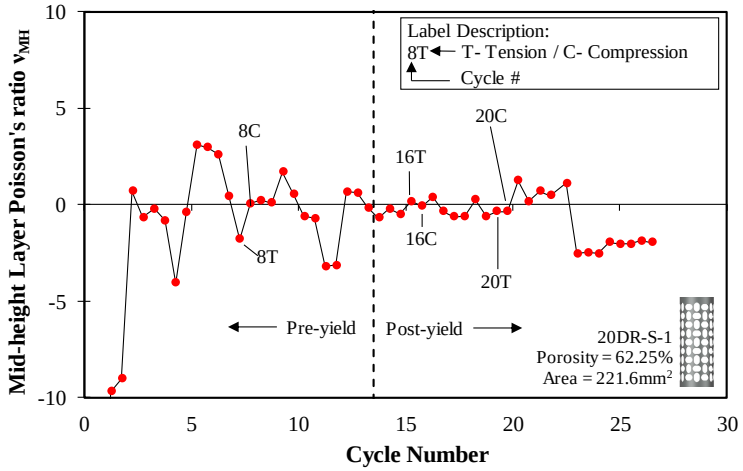

a) Mid-height Layer Poisson's ratio v_{MH}

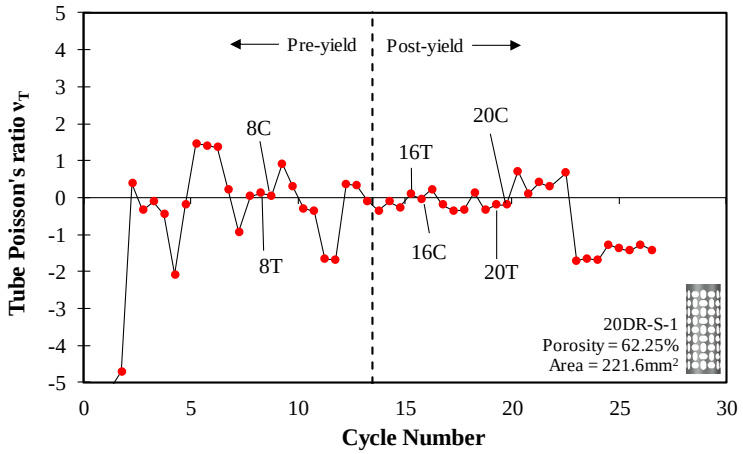

b) Tube Poisson's Ratio v_T

Figure 3.12: v_{MH} and v_T in Specimen 20DR-S-1.

Figure 3.13 shows the radial displacements calculated in the specimen during compression and tension cycles. The specimen showed greater radial deformation in compression than tension Initially, the radial deformations were uniformly distributed in the tube. However, deformations concentrated in layers L_4 and L_6 in the final compressive cycles and were observed to concentrate

in layer L_6 prior to failure under tension. While local deformed shapes of individual layers were not visible to the naked eye, a global inward deformation of the tube at mid-height layer could be seen in the final compressive cycle, confirming the presence of apparent NPR behavior.

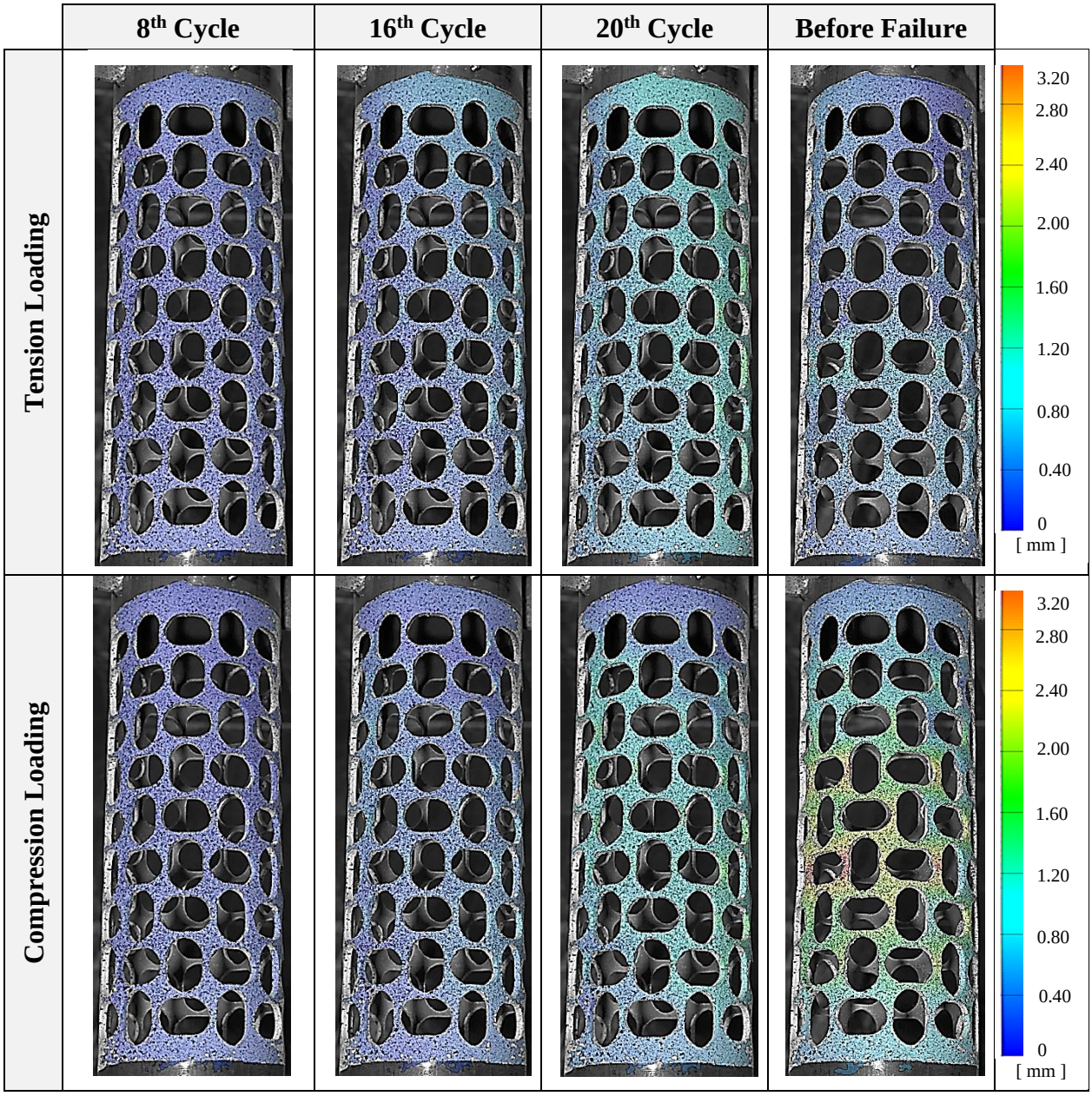

Figure 3.13: Radial Displacements in Specimen 20DR-S-1.

3.7. Specimen 40DR-S

Specimen 40DR-S was the steel specimen containing the *40*DR cell topology designed to demonstrate negative Poisson's ratio behavior. Figure 3.14 shows the photographs of the specimen before testing and after failure.

a) Prepared specimen

b) Tensile failure in cell wall in layer L_5

Figure 3.14: Photographs of Specimen 40DR-S.

Specimen 40DR-S failed in the tension leg of the 28^{th} cycle at a load of *66.2 kN* and an axial deformation of *5.30 mm*. Peak tensile load coincided with *1.82%* average vertical strain ε_A. Radial contraction and expansion were not discernable during testing and only the change in shape of cells could be observed with the naked eye, with cells expanding under tension and vice versa. Tensile rupture of the cell walls (Figure 3.14 (b)) was observed in layer L_5 which propagated through two cell walls before the experiment was stopped. The failed sample was unloaded and a residual deformation of *4.92 mm* was recorded.

The hysteretic load-strain response of the tube under cyclic loading is presented in Figure 3.15 (a). The response was symmetric in tension and compression, with a consistent elastic slope.

Apparent yielding was observed at *24.5 kN* in tension and *-20.1 kN* in compression. The tube exhibited significant strain hardening under tension while the same was not observed in compression, as a consequence of geometrically induced buckling. Unloading slopes were consistent during the experiment.

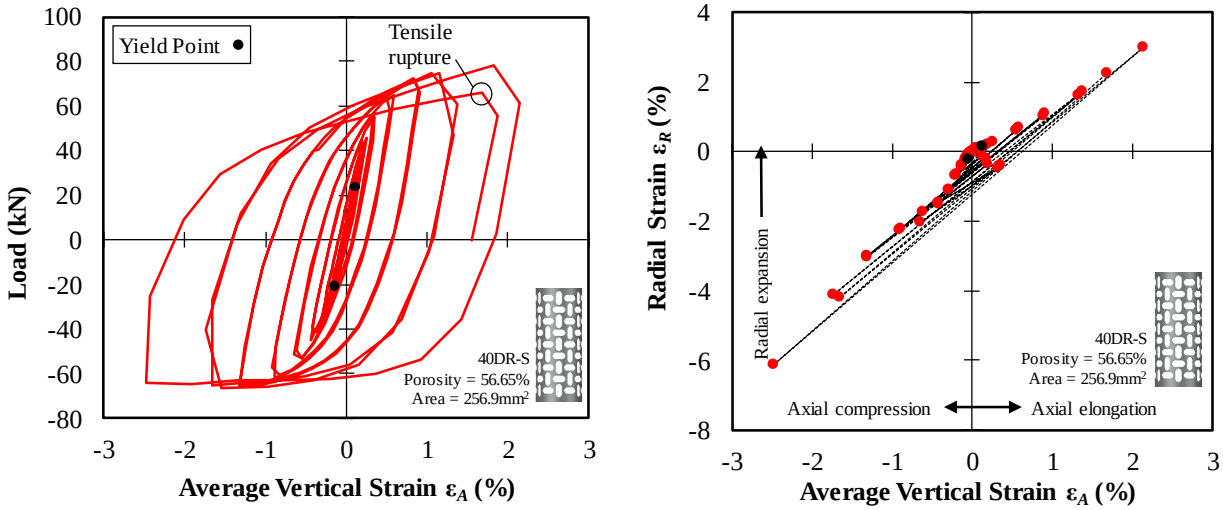

(a) Load vs. average vertical strain (ε_A)

(b) Radial strain (ε_R) vs. average vertical strain (ε_A)

Figure 3.15: Specimen 40DR-S deformation data.

The variation in radial strain (ε_R) with average vertical strain (ε_A) for mid-height layer L_5 is visualized in Figure 3.15 (b). The tube exhibited consistent NPR behavior throughout the experiment as the figure maintains a constant positive slope throughout the experiment, with no apparent effect of the type of loading. A slight residual radial contraction in layer L_5 takes place.

This consistent NPR behavior is also displayed in Figure 3.16, where Poisson's ratios, v_L and v_T are presented. Yielding was observed in the *14th* cycle. The specimen exhibited an average negative value of *-3.5* and *-2* for v_L and v_T, respectively, throughout the test. Yielding had a brief destabilizing effect on PR values, which subsided after four loading cycles.

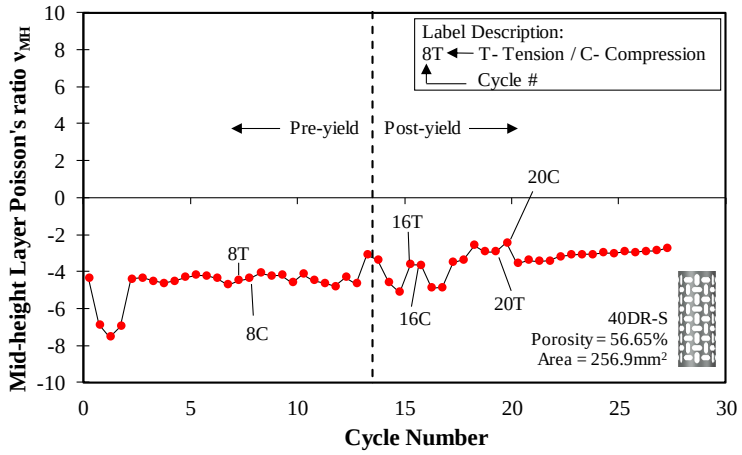

a) Mid-height Layer Poisson's ratio v_{MH}

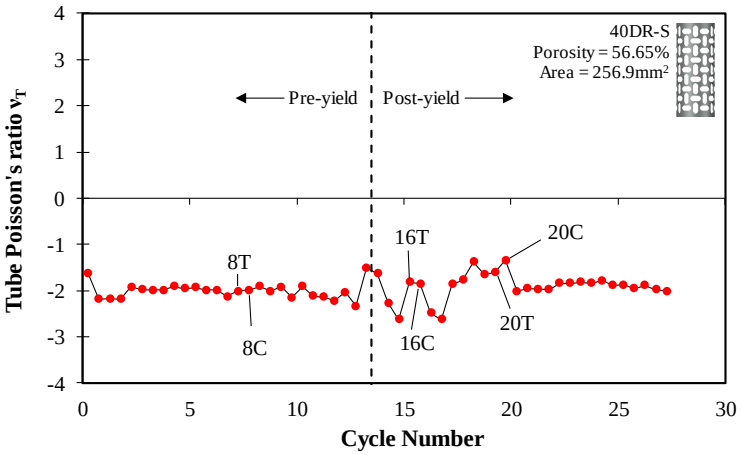

b) Tube Poisson's Ratio v_T

Figure 3.16: v_{MH} and v_T in Specimen 40DR-S.

Radial displacements in the specimen computed for the specimen can be seen in Figure 3.17. In general, greater radial deformations were recorded in compression than in tension. Deformations were uniformly distributed throughout the height of the tube initially, but concentrated to layer L_5 under increasing axial strains. A high concentration of radial deformation in layers $L_4 - L_6$ was observed and a clear global radial contraction was visible in the tube layers during the final compressive cycle, producing an hour-glass deformed shape. It can be concluded that global deformations induced by cell geometry dominated the deformation response relative to local inelastic deformations which were not observed.

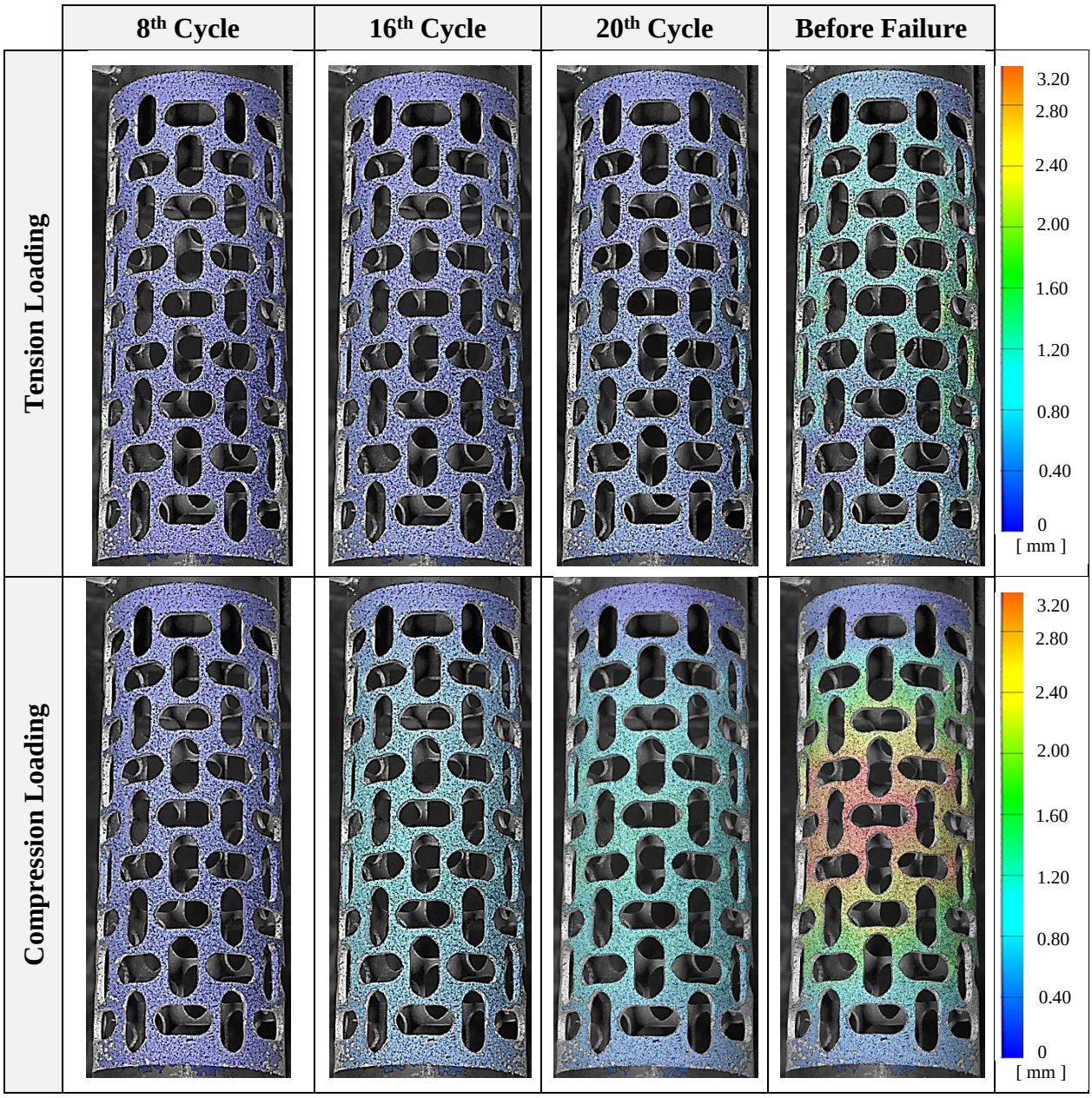

Figure 3.17: Radial Displacements in Specimen 40DR-S.

3.8. Specimen 0DR-A

Specimen 0DR-A was the aluminum control specimen designed to exhibit positive Poisson's ratio with its array of circular voids. Photographs of the condition of 0DR-A before and after testing are shown in Figure 3.18.

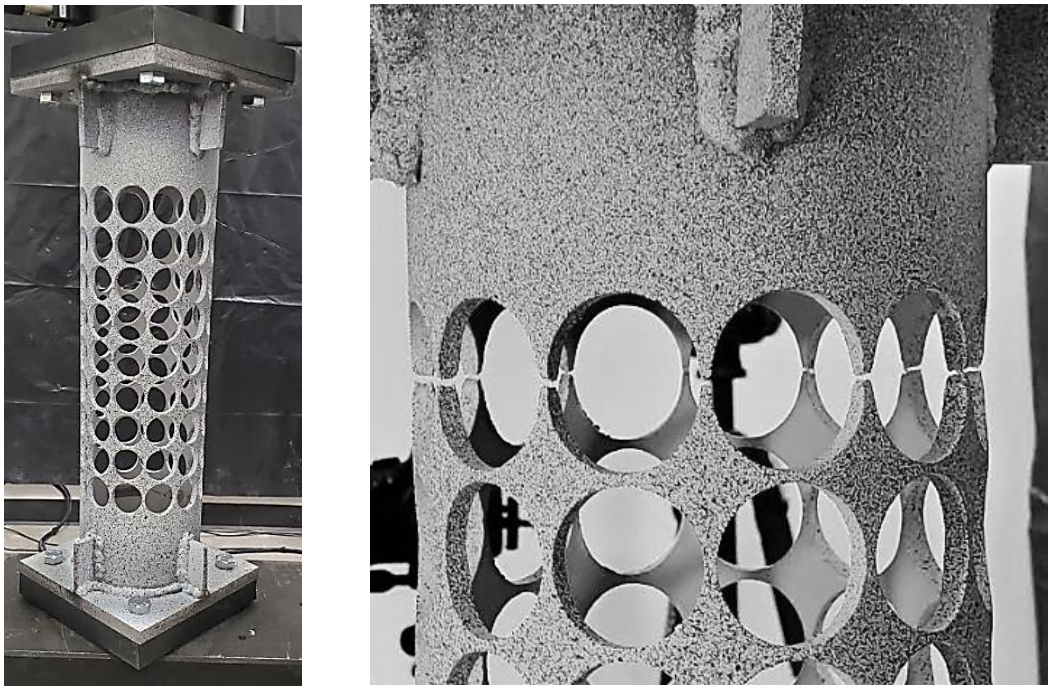

a) Prepared specimen b) Tensile failure in cell wall in Layer L_1

Figure 3.18: Photographs of Specimen 0DR-A.

Specimen 0DR-A failed in the tension leg of the 18th cycle at a load of *17.9 kN* and an axial deformation *of 0.85 mm*. Value for strain ε_A at peak tension was *0.49%*. Tensile rupture of the cell walls (Figure 3.18 (b)) was observed in layer L_1 which propagated through all adjacent cell walls before loading was halted. The failed sample was unloaded and a residual crosshead deformation of *2.29 mm* was recorded.

Figure 3.19 (a) shows the hysteretic load-strain response of the tube under cyclic loading. The elastic slopes for tension and compression were similar, with tension yielding occurring at *7.9 kN* compared to a compression yielding load of *-7.1 kN*. A comparison of peak experimental axial stresses and coupon ultimate stress was conducted which showed a *41%* reduction in experimental peak stress compared to coupon results. Reasons for this discrepancy are attributed to heat treatment of the base metal and will be highlighted in Section 4.8. Significant strain hardening was

observed in tension defined by the positive slope of the diagram. In contrast, no noteworthy hardening was present in compression loading due to the out-of-plane deformations of cell walls.

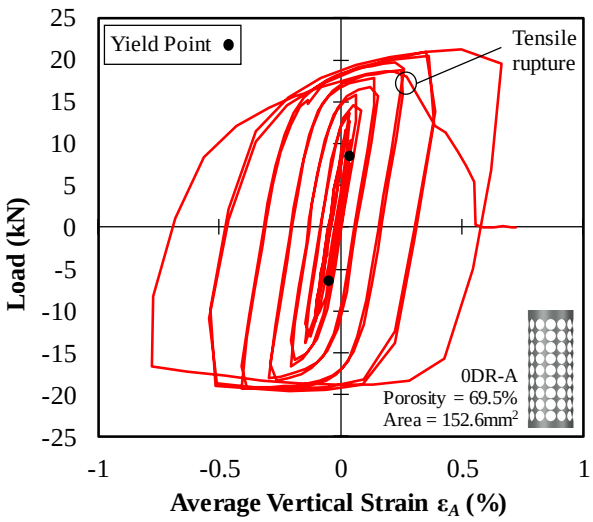

(a) Load vs. average vertical strain (ε_A)

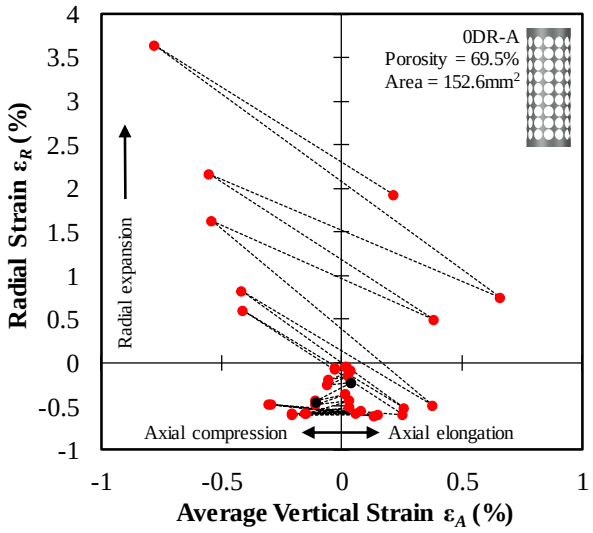

(b) Radial strain (ε_R) vs. average vertical strain (ε_A)

Figure 3.19: Specimen 0DR-A deformation data.

Figure 3.19 (b) shows the variation in radial strain (ε_R) with average vertical strain (ε_A) for mid-height layer L_5. It can be concluded that a positive Poisson's ratio behavior was exhibited by examining the negative value of slope for the diagram. The slope of the plot remained flat before yielding. The onset of yielding led to a decrease in slope before shifting to positive value which was maintained until failure. In a given loading cycle, the slope of the diagram was similar for tension and compression, indicating the consistency in the deformation mechanism. The figure indicates that a permanent radial expansion of the tube takes place with final radial strain remaining positive.

Poisson's ratios, v_L and v_T, are presented in Figure 3.20 for layer L_5 which confirm PPR behavior in the specimen. Yielding occurred in the 14th loading cycle. The measured response of 0DR-S-1 demonstrated a shift in PR behavior, with values in the negative domain prior to yield and positive PR values post-yield. Before yielding, v_L and v_T had a constant average value of *-1*. As the tube began to deform inelastically, a significant rise was observed in v_L and v_T which rose to ultimate average values of *10* and *2*. This drastic shift may be attributed to formation of plastic hinges in the cell walls.

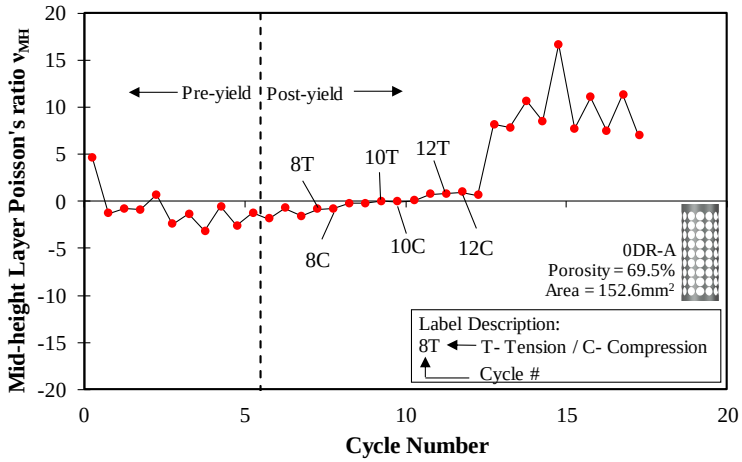

a) Mid-height Layer Poisson's ratio v_{MH}

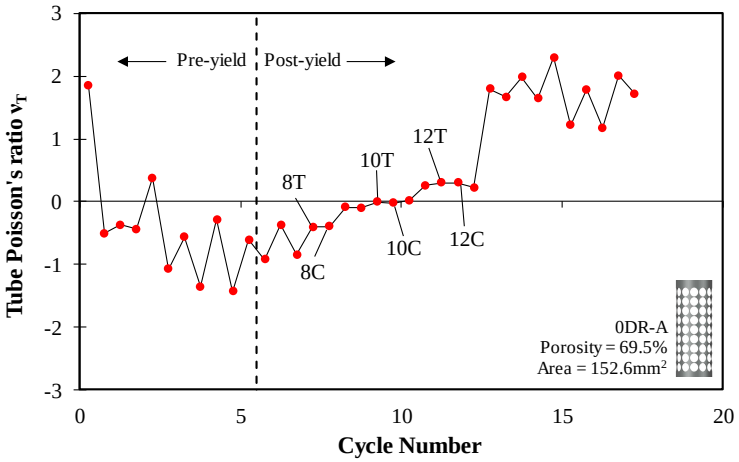

b) Tube Poisson's Ratio v_T

Figure 3.20: v_{MH} and v_T for specimen 0DR-A.

Figure 3.21 shows the radial deformations in 0DR-S-1 during tension and compression loading measured at the 8th, 10th, 12th, and final cycle before failure. It was observed that the magnitudes of radial deformations were similar in tension and compression. Generally, deformations were uniform along the height of the tube. However, in the final cycles before failure, deformations were concentrated in the cell walls due to instability which caused a sinusoidal deformed shape. Radial deformations were highest in layers L_4 and L_6 in the compressive and tensile cycle prior to failure.

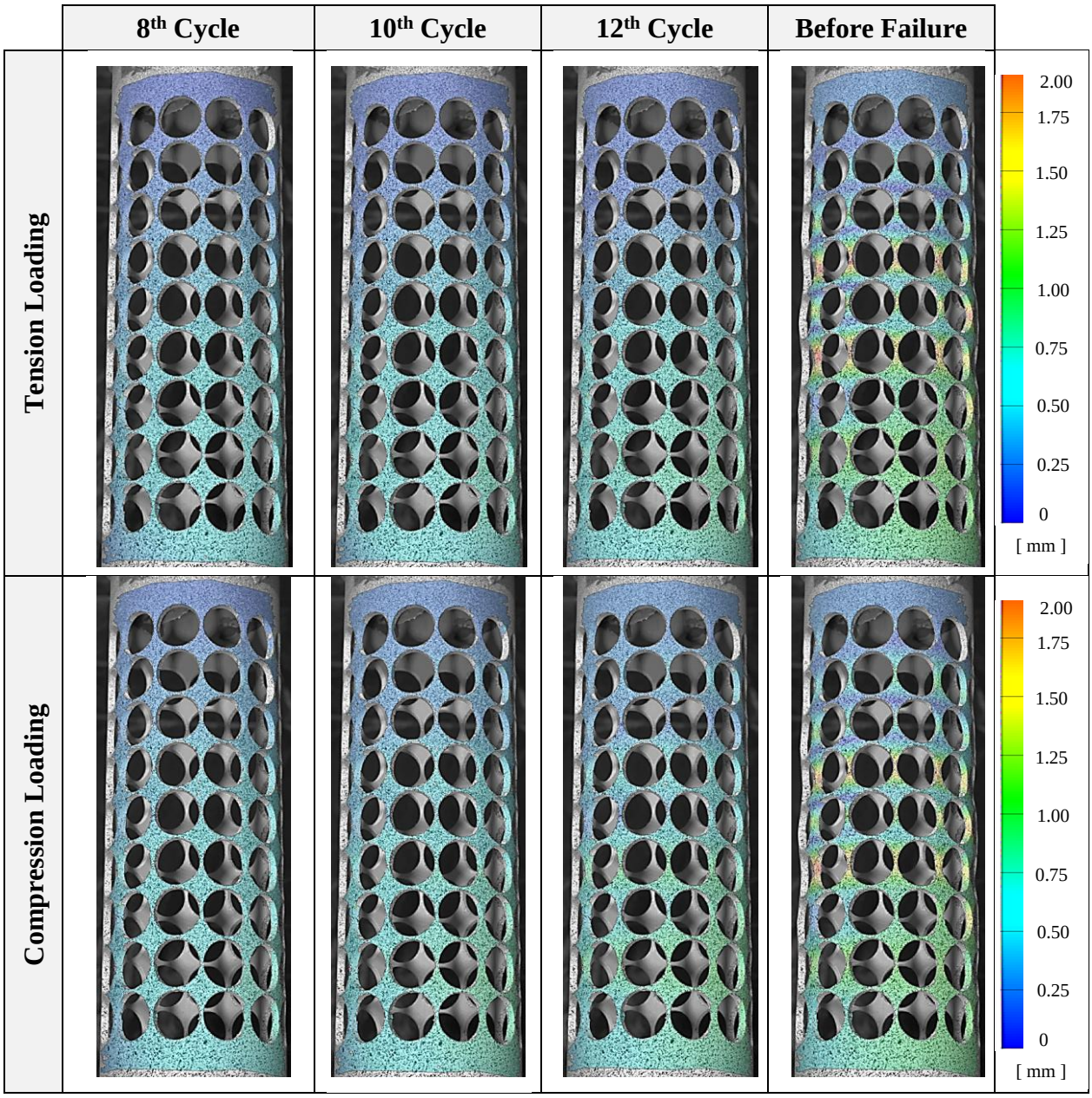

Figure 3.21: Radial Displacements in Specimen 0DR-A.

3.9. Specimen 20DR-A

Specimen 20DR-A was the aluminum specimen designed with a cell geometry to induce auxetic behavior. Photographs of the specimen before testing and after failure are presented in Figure 3.22.

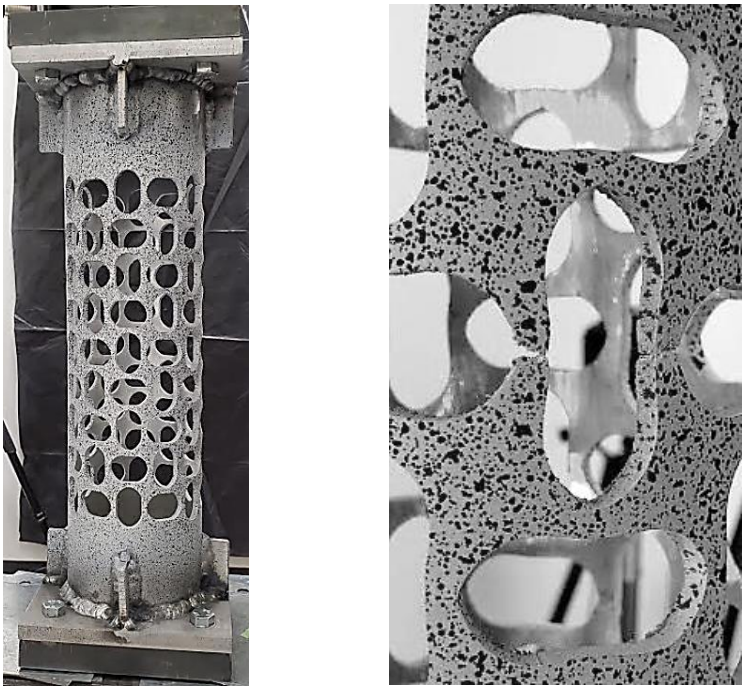

a) Prepared specimen b) Tensile failure in cell wall in Layer L_6

Figure 3.22: Photographs of Specimen 20DR-A.

Specimen 20DR-S-1 failed in the tension leg of the *26th* cycle at a load of *21.7 kN* and an axial deformation of *4.08 mm*. Peak tension load occurred at *1.27%* average vertical strain ε_A. Radial contraction could be seen with the naked eye but expansion was not visually apparent, however, the change of shape of cells could be observed; cells dilated under tension. Tensile rupture of the cell walls (Figure 3.22 (b)) was observed in layer L_6 which propagated through two cell walls before loading was halted. The failed sample was unloaded and a residual axial deformation of *3.91 mm* was recorded.

The hysteretic load-strain response of the tube under cyclic loading is presented in Figure 3.23 (a). The elastic slope was constant for compression and tension although yielding occurred before compression at *12.2 kN* as opposed to *-11.1 kN*. Strain hardening was observed in tension

but was not as significant in compression due to the geometrically induced buckling in the tube. Unloading slopes were consistent throughout the experiment.

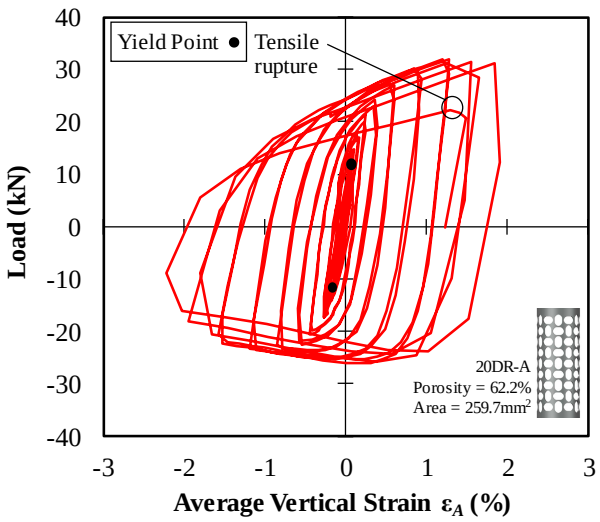

(a) Load vs. average vertical strain (ε_A)

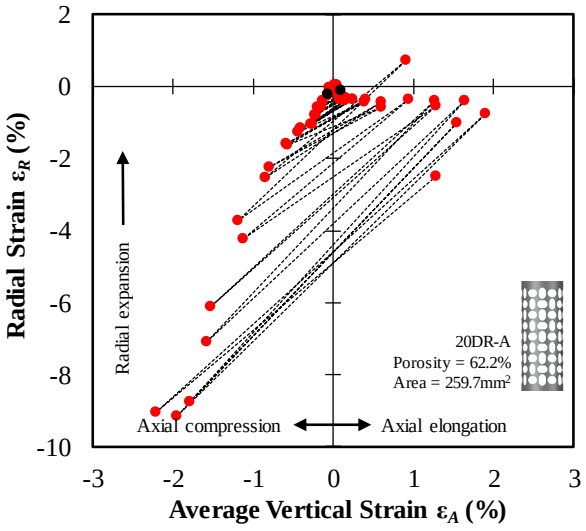

(b) Radial strain (ε_R) vs. average vertical strain (ε_A)

Figure 3.23: Specimen 20DR-A deformation data.

The variation in radial strain (ε_R) with average vertical strain (ε_A) for mid-height layer L_5 is shown in in Figure 3.23 (b). The slope of the plot was consistently positive for the experiment and was not affected by the nature of loading, compressive or tensile. The negative value of slope for the figure is representative of the Poisson's ratio (v_L), therefore, it can be concluded that the tube exhibited NPR behavior. A residual radial contraction was also observed in the tube.

Figure 3.24 presents the variation of Poisson's ratios, v_L and v_T. NPR behavior was observed throughout. The specimen yielded in the 8^{th} cycle and exhibited an average value of *-2.5* and *-1.5* for v_L and v_T, respectively, prior to yielding. Yielding did not have a drastic effect on PR values, and average post-yield PR values of *-1.5* and *-2* were recorded for v_L and v_T, respectively.

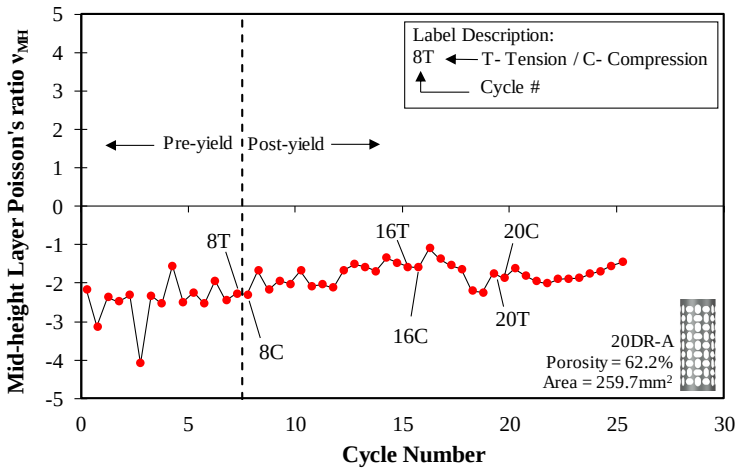

a) Mid-height Layer Poisson's ratio v_{MH}

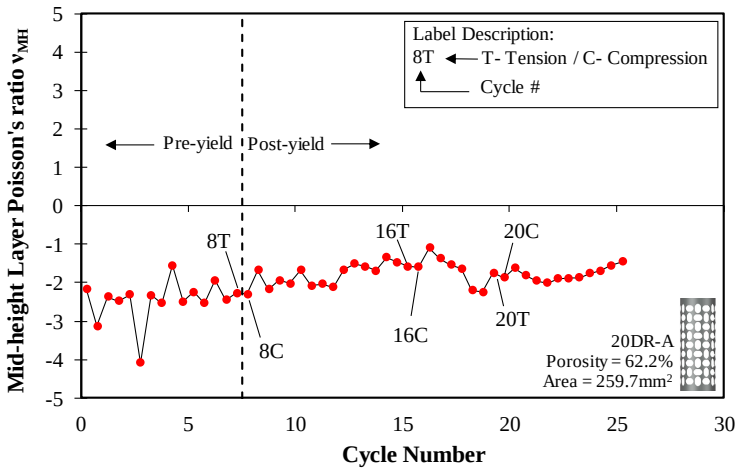

b) Tube Poisson's Ratio v_T

Figure 3.24: v_{MH} and **v_T** in Specimen 20DR-A.

Figure 3.25 shows the radial displacements calculated in the specimen during compression and tension cycles. Deformations were seen to concentrate in layers $L_4 - L_6$ and finally in layer L_6 prior to failure. Near failure, an un-symmetric radial contraction was observed in layer L_6. A global inward deformation of the tube at mid-height layer was clearly visible with the naked eye in the final compressive cycle with the tube assuming an hourglass shape, confirming the presence of apparent NPR behavior.

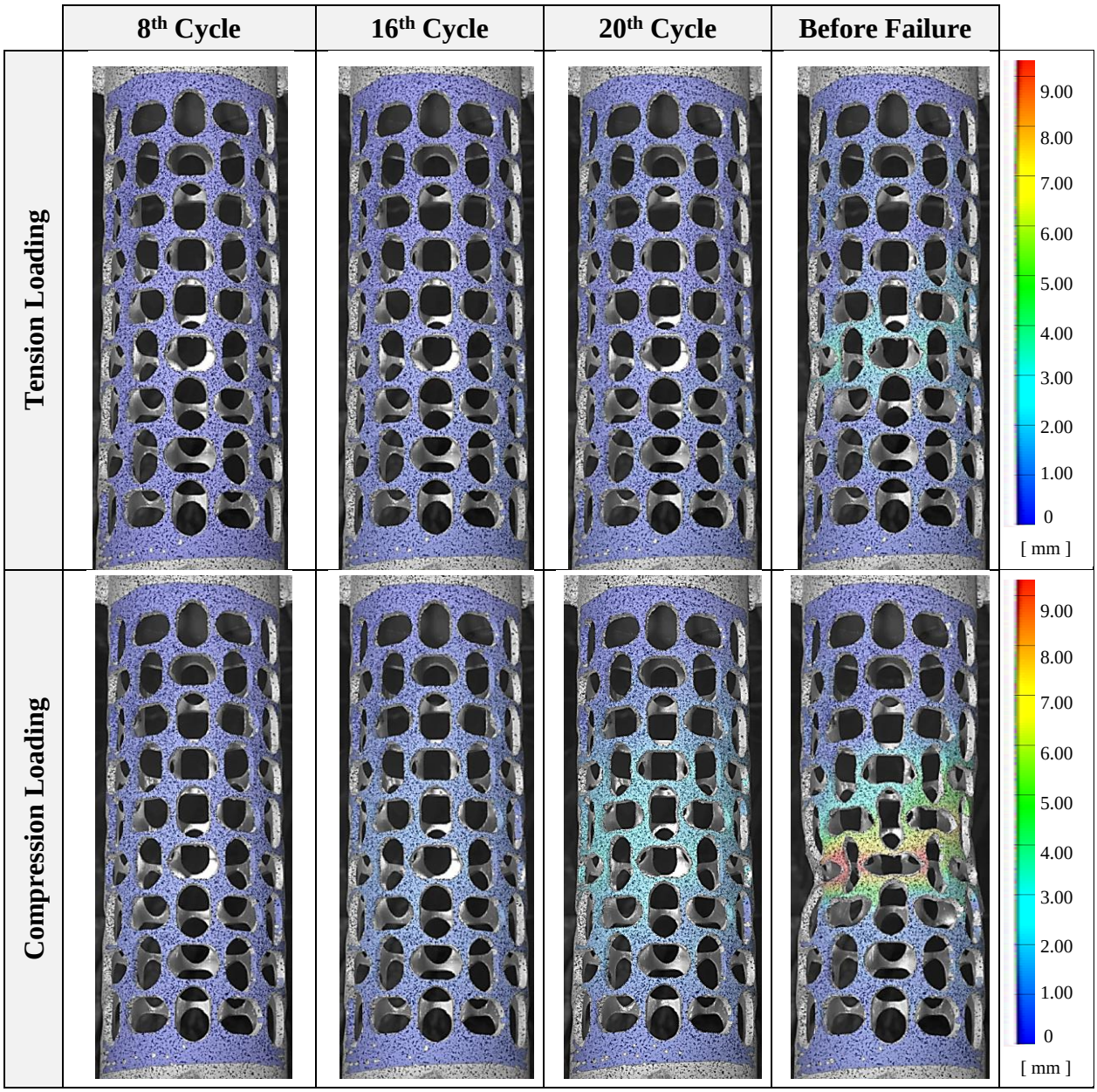

Figure 3.25: Radial Displacements in Specimen 20DR-A.

3.10. Specimen 40DR-A

Specimen 40DR-A was the steel specimen containing the *40*DR geometry of cells. It was designed to demonstrate negative Poisson's ratio behavior. Figure 3.26 shows the photographs of the specimen before testing and after failure.

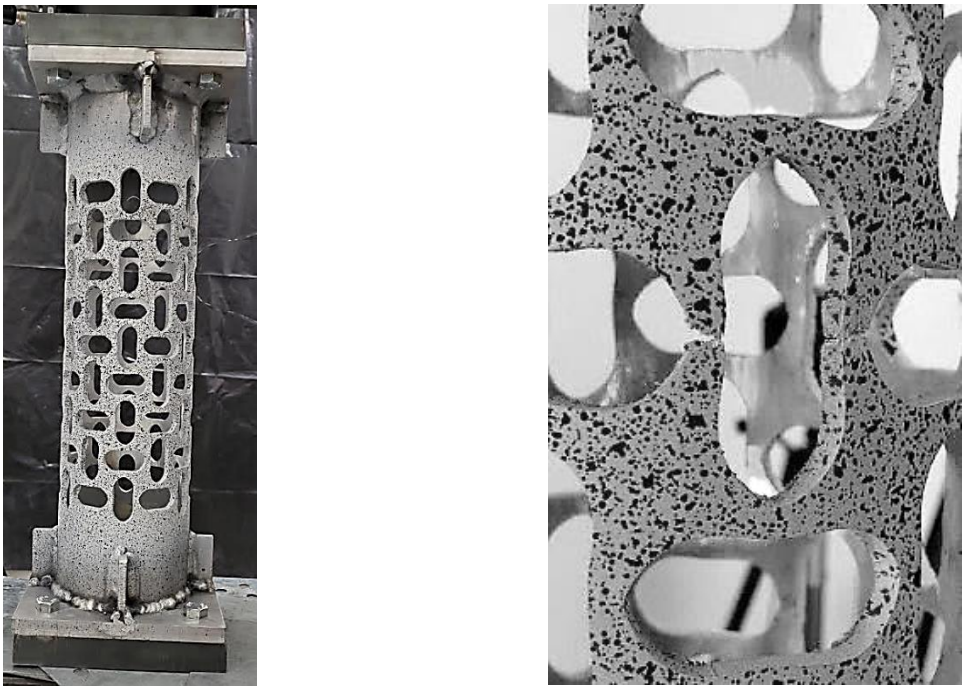

a) Prepared specimen b) Tensile failure in cell wall in layer L_5

Figure 3.26: Photographs of Specimen 40DR-A.

Specimen 40DR-A failed in the tension leg of the 28^{th} cycle at a load of *23.4 kN* and an axial deformation of *1.22 mm*. Tensile rupture of the cell walls (Figure 3.26 (b)) was observed in layer L_5 which propagated through two cell walls before the experiment was stopped. The failed sample was unloaded and a residual deformation of *0.68 mm* was recorded. Peak tensile load coincided with *1.74%* average vertical strain ε_A

The hysteretic load-strain response of the tube under cyclic loading is presented in Figure 3.27 (a). The elastic response was symmetric, with a consistent elastic slope under both compression and tension. Apparent yielding was observed at *10.4 kN* in tension and *-6 kN* in compression. The tube exhibited significant strain hardening under tension while the same was not

observed under compression, as a consequence of geometrically induced buckling. Unloading slopes were consistent during the experiment.

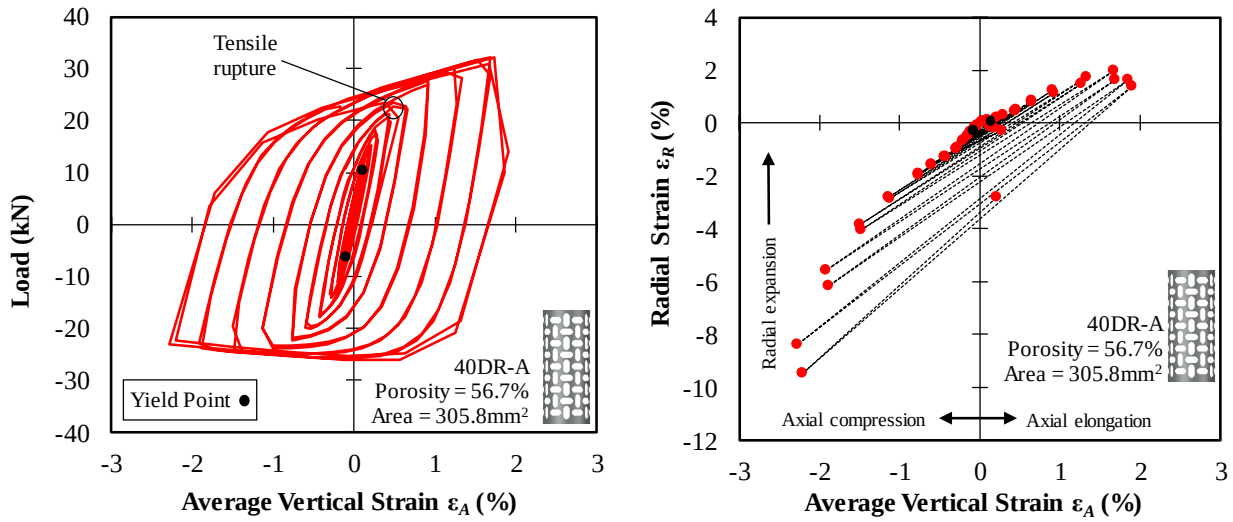

(a) Load vs. average vertical strain (ε_A)

(b) Radial strain (ε_R) vs. average vertical strain (ε_A)

Figure 3.27: Specimen 40DR-A deformation data.

The variation in radial strain (ε_R) with average vertical strain (ε_A) for mid-height layer L_5 is visualized in Figure 3.27 (b). The figure maintains a constant positive slope throughout the experiment, exhibiting consistent NPR behavior, with no apparent effect of loading type. A residual radial contraction in layer L_5 takes place.

This consistent NPR behavior is displayed in Figure 3.28, where Poisson's ratios, v_L and v_T are presented. Yielding was observed in the 8^{th} cycle. An average value of *-3* and *-2.25* was recorded for v_L and v_T, respectively, prior to yielding. Although yielding did not have a drastic effect on PR values, a temporary instability in PR values was seen post-yield which stabilized over eight cycles to reach stable average values of of *-2.5* for both v_L and v_T. v_T also appeared to be decreasing constantly up to failure.

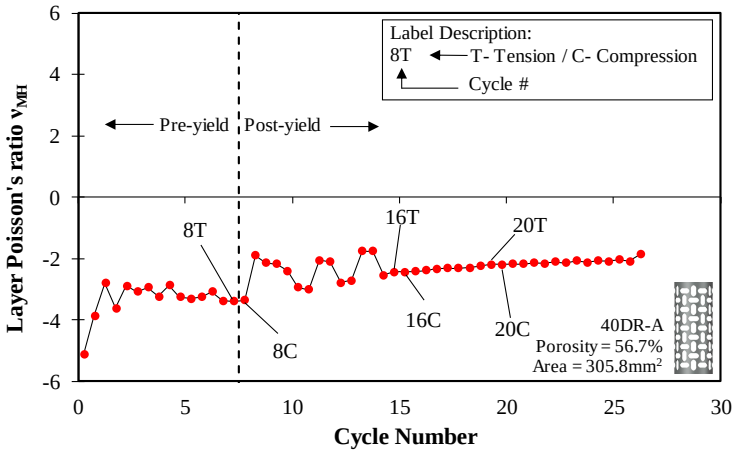

a) Mid-height Layer Poisson's ratio v_{MH}

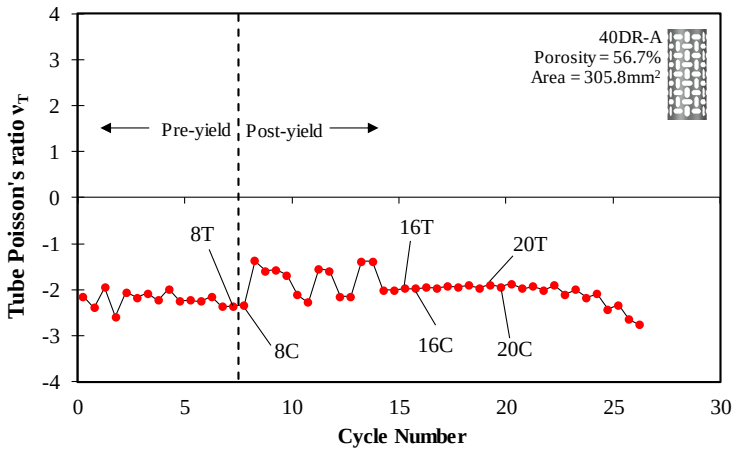

b) Tube Poisson's Ratio v_T

Figure 3.28: v_{MH} and v_T in Specimen 40DR-A

Radial displacements in the specimen computed for the specimen can be seen in Figure 3.29. In general, greater radial deformations were recorded in compression than in tension. Deformations were uniformly distributed throughout the height of the tube initially, but concentrated to layer L_5 under increasing axial strains. A high concentration of radial deformation in layers $L_4 - L_6$ was observed and a clear global radial contraction was visible in the tube layers during the final compressive cycle. This hourglass deformed configuration confirmed NPR behavior in the tube. It can also be concluded that global deformations induced by cell geometry dominated the deformation response relative to local inelastic deformations in the cell walls, which were not apparent.

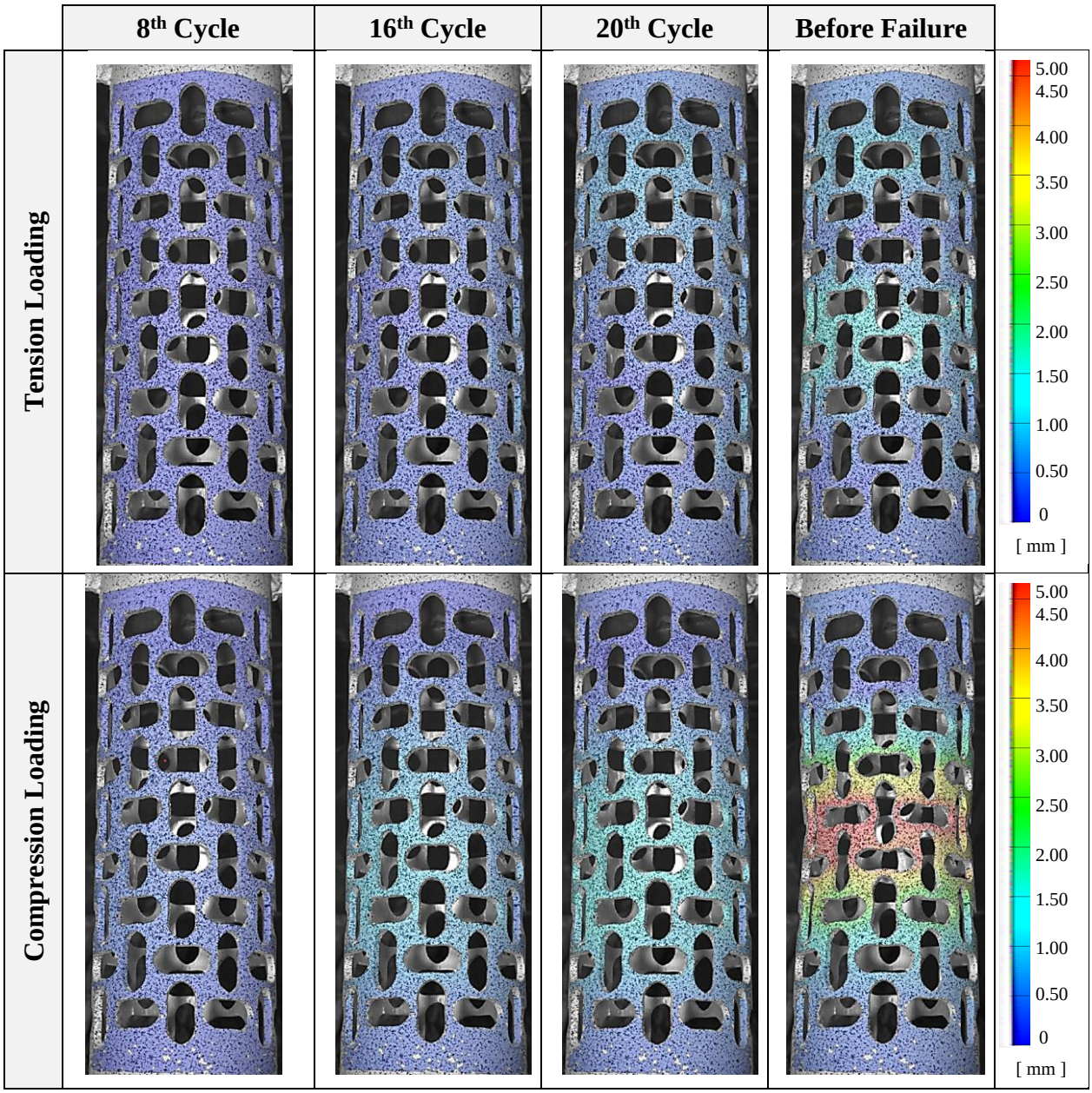

Figure 3.29: Radial Displacements in Specimen 40DR-A.

3.11. Specimen 20DR-S-2

Specimen 20DR-S-2 was the steel specimen designed to exhibit negative Poisson's ratio behavior due to its cell geometry. It was the only sample tested under a monotonic compressive displacement. Photographs of the condition of 20DR-S-2 before and after testing are shown in Figure 3.30.

a) Prepared specimen b) Densification of tube

Figure 3.30: Photographs of Specimen 20DR-S-2

While no rupture was observed in specimen 20DR-S-2 during the experiment, as per the failure criteria, the test was stopped when opposing cell walls came into contact. Failure occurred at *-8.8%* axial strain ε_A while peak compressive load was recorded at *-1.54%* average vertical strain. The specimen displayed clear negative Poisson's ratio behavior with radial contraction of the tube under progressive compressive displacement, as shown in Figure 3.30 (b).

Figure 3.31 (a) shows the load-strain response of the specimen. Negative values have been plotted on the positive axes. Apparent yielding occurred at an axial load of *-30.2 kN.* After yielding, strain hardening was observed and the specimen reached a peak loading value of *-72.6 kN.* Subsequently, a sudden decline in strength was observed due to the onset of buckling characterized

by a constant contraction of the tube at mid-height. Strength decreased with increasing plastic deformations in the cell walls. It is important to note that once the cell walls came into contact, the specimen started to resist greater loads.

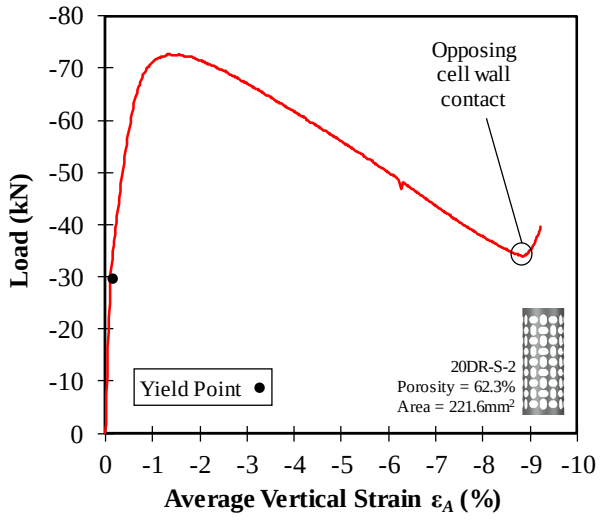

(a) Load vs. average vertical strain (ε_A)

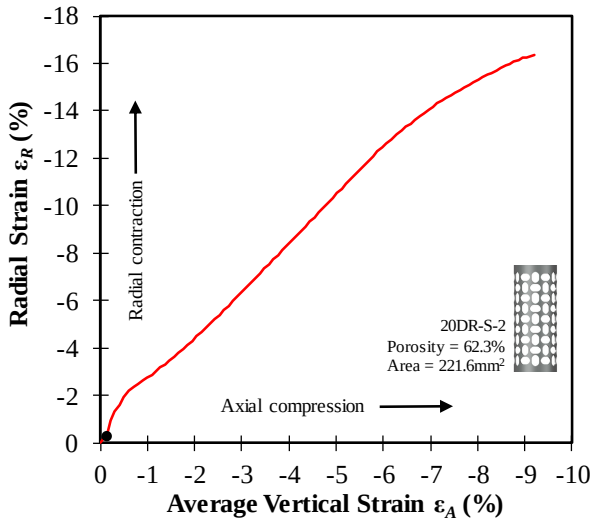

(b) Radial strain (ε_R) vs. average vertical strain (ε_A)

Figure 3.31: Specimen 20DR-S-2 deformation data.

Figure 3.31 (b) shows the variation in radial strain (ε_R) with average vertical strain (ε_A) for mid-height layer L_5. The plot maintains a consistent positive slope post yield, demonstrating positive Poisson's ratio behavior. Before peak loading, the slope of the diagram has a higher value and a maintained decreased slope is visible after the onset of buckling.

Poisson's ratios, v_{L5} and v_T, are presented in Figure 3.32 for layer L_5. Consistent NPR is observed. Both figures show that v_L and v_T achieve peak NPR values of *-4.15* and *-7*, respectively, at *-0.22%* ε_A. Yielding occurred at *-0.11%* ε_A. Thus, yielding caused a drastic shift in PR values between the strain range *-0.22%* to *-2.41%* ε_A before stabilizing. Average values of *-2.5* and *-2* for v_L and v_T, respectively, were observed; excluding the initial abrupt change.

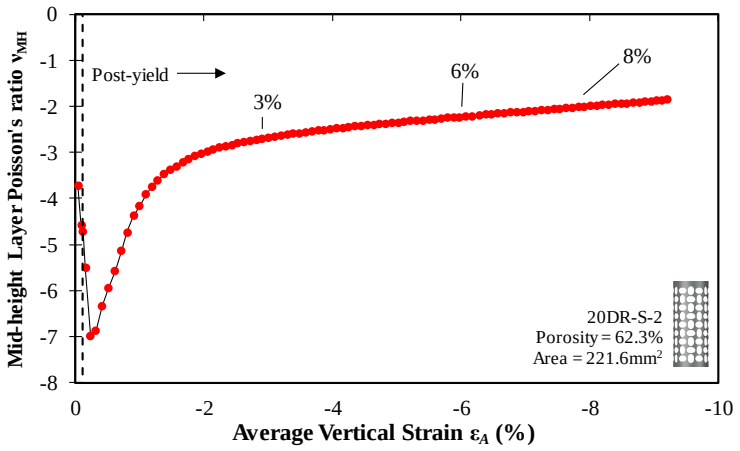

a) Mid-height Layer Poisson's ratio v_{MH}

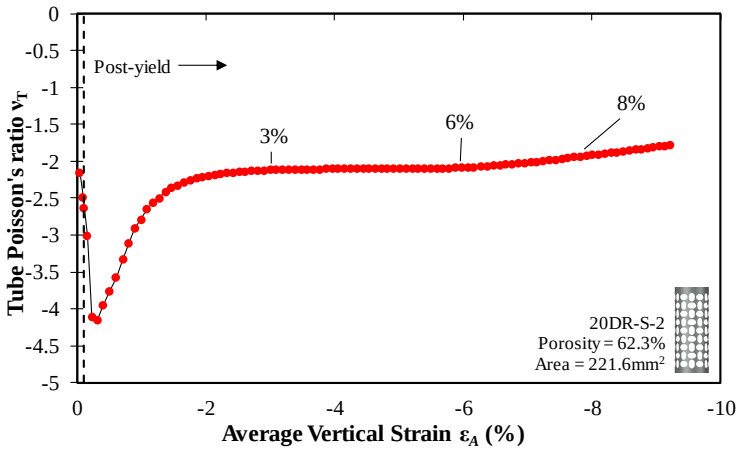

b) Tube Poisson's Ratio v_T

Figure 3.32: v_{MH} and v_T in Specimen 20DR-S-2.

A visual representation of radial displacement in the specimen is shown in Figure 3.33 which can be related to marked locations on Figure 3.32. Radial contraction was initially spread uniformly through layer L_2 to L_8 but, concentrated towards layer L_6 with an increase in compressive axial strain. High radial contraction in layer L_6 led to an eventual contact of cell walls.

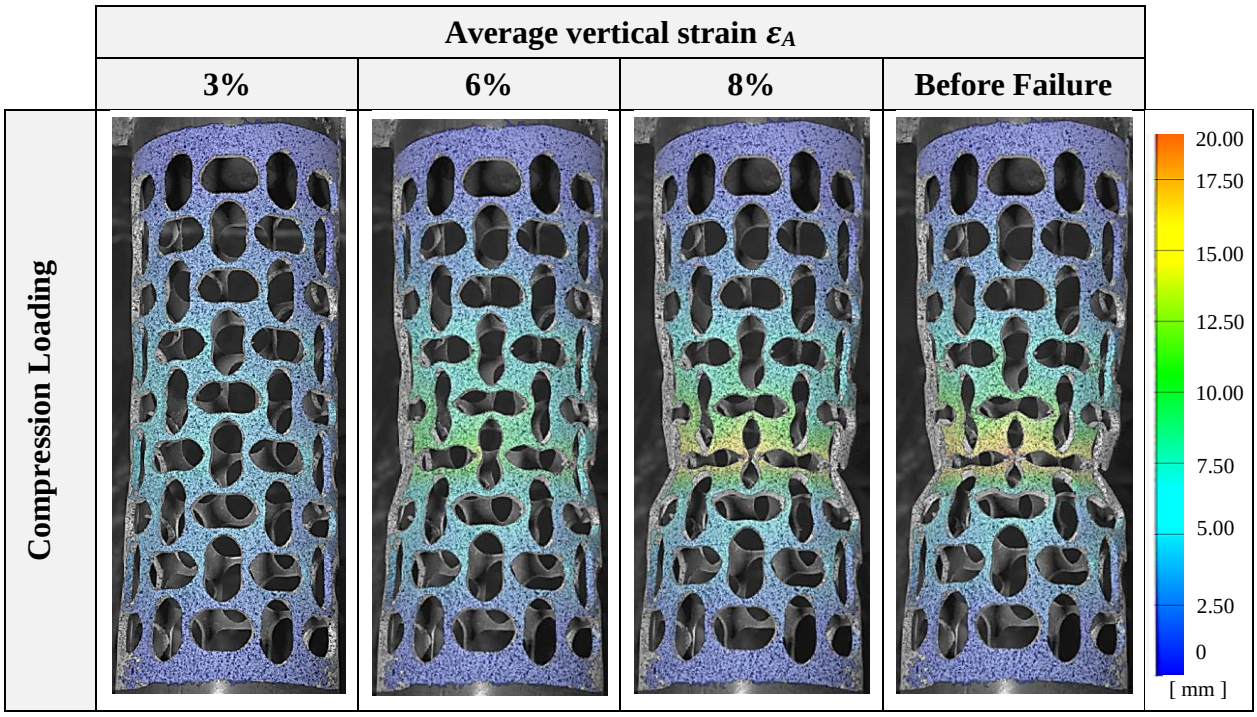

Figure 3.33: Radial Displacements in Specimen 20DR-S-2.

Chapter 4. Discussion of Experimental Results

4.1. Overview

This section discusses and compares the experimental results and observations of the eight auxetic and non-auxetic metal tubes tested during the experimental program. The effects of auxetic topology and base material on load-deformation response, energy absorption, deformation response, and failure mode are all considered. The effects of the tube manufacturing process on base material properties is discussed.

4.2. Effect of Auxetic Topology on Structural Deformations

Experimental observations confirmed that ductile metal tubes are capable of demonstrating auxetic behavior. This is supported by the fact that all specimens containing the auxetic cell topology demonstrated deformations characteristic of NPR. This also suggests that deformed shapes in ductile metal tubes can be controlled through the introduction of a unique cellular topology.

Increased stability in the auxetic specimens has been illustrated through Figure 4.1 and Figure 4.2, which show the deformed shape of the fully-plastic steel and aluminum specimens in the final cycles before failure, respectively. The patterns over the entire gauge height were visualized using three-dimensional displacements recorded using the DIC system.

It can be observed that in non-auxetic 0DR specimens, radial strains concentrated at cell mid-height which resulted in a localized instability in individual cell layers. A wave-like deformed mode was observed along the height of the cell pattern under axial compression. However, auxetic cell topologies demonstrated a significant reduction in the observed localized instability as the DR value was increased. Instead, a global deformation along the height of the topology was observed with maximum deformations generally recorded in the mid-height layer L_5. This was due to the presence of boundary effects produced by the fixed end conditions in the tubes. In theory, it is predicted that the radial response would have greater uniformity if the vertical height of specimens

is increased, minimizing boundary effects. Straightening of the tube walls was observed under tensile load, although plastic response led to permanent residual deformations.

The global deformation mechanism can be attributed to the unique cell geometry introduced in the tube walls which causes cell rotation, leading to the observed response. This unique deformation mechanism directly influenced the global stability of the tube, hence can be beneficial for generating ductile metal elements with enhanced stability and load-bearing capacity.

Furthermore, the transition from non-auxetic to auxetic topology by the means of increasing DR value resulted in a more geometrically stable deformed shape, with little to no local instabilities observed in individual layers of cells. Tube with non-auxetic topologies exhibited local buckling of cell walls in compression, leading to the development of unstable deformation mechanisms. Increasing the DR value of auxetic tubes produced a more geoemtrically stable and uniform deformed shape which counteracted the buckling mechanisms observed in non-auxetic tubes. The improvement in behavior observed in the auxetic topologies is thought to be due to the formation of a stabilizing hoop stress in the circumfrential direction under the action of NPR deformations. This suggests that an additional stability can be imparted to a tubular element by altering a geometric parameter such as DR, while maintaining tube dimensions such as size and thickness. This may lead to an enhancement in load-bearing properties in structural elements without affecting structural weight or size.

The novel transformation in the global structure of tubes offered by the auxetic effect can be exploited to design enhanced, stable structural elements. These enhanced structures canbear higher loads than equally porous non-auxetic tubular geometries at large deformations while minimizing second-order effects by maintaining concentric axial forces. Furthermore, the deformation mechanism caused by the unique auxetic topology can be used to augment existing structural systems through means of an external auxetic element. For example, the radial contraction demonstrated by auxetic tubes under axial compression can be utilized to apply an active confining force to columns, thereby increasing their load-bearing capacity and enhancing ductility.

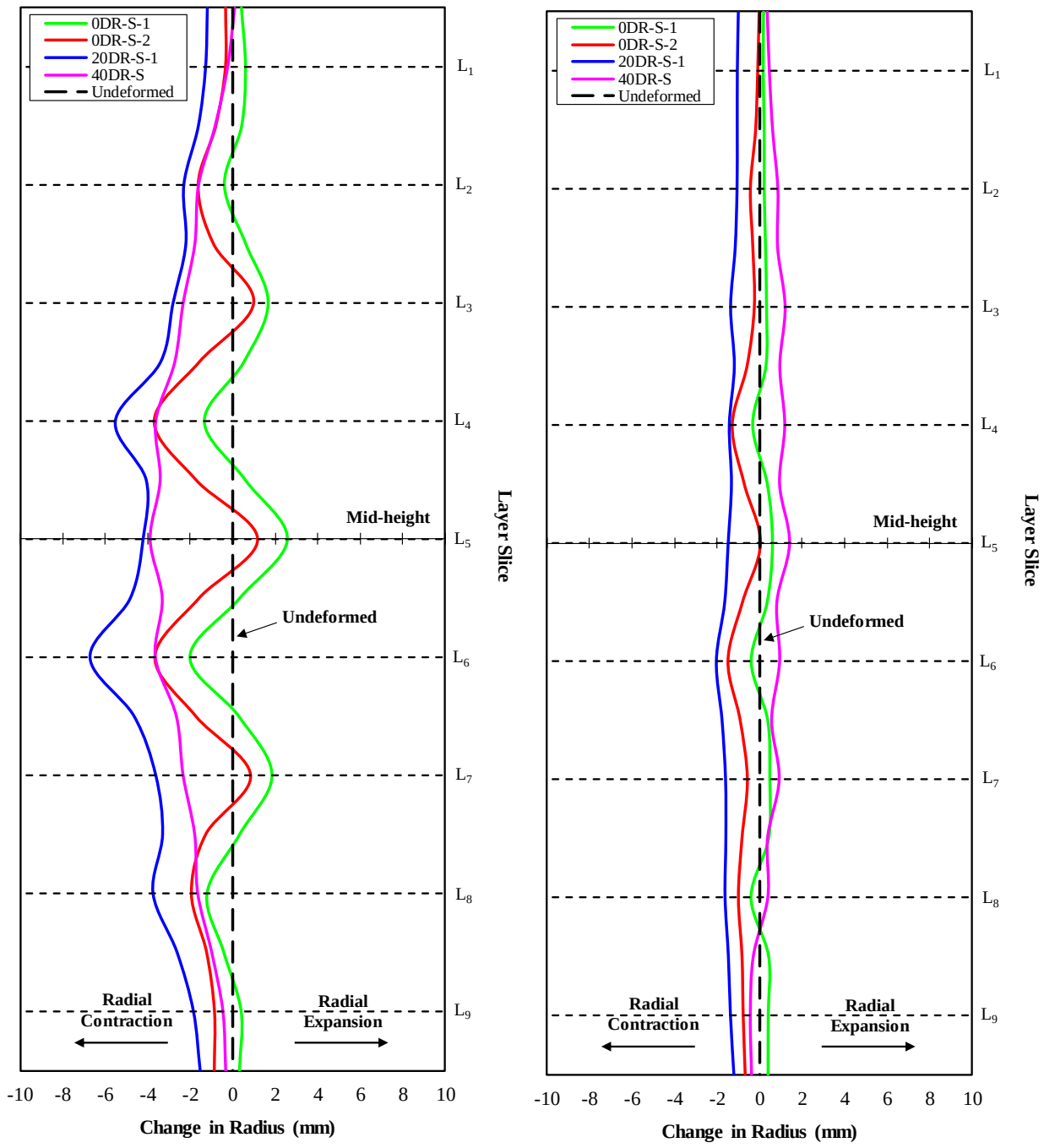

(a) Final compressive cycle before failure

(b) Final tension cycle before failure

Figure 4.1: Comparison of deformed shapes in steel specimens obtained from DIC measurements.

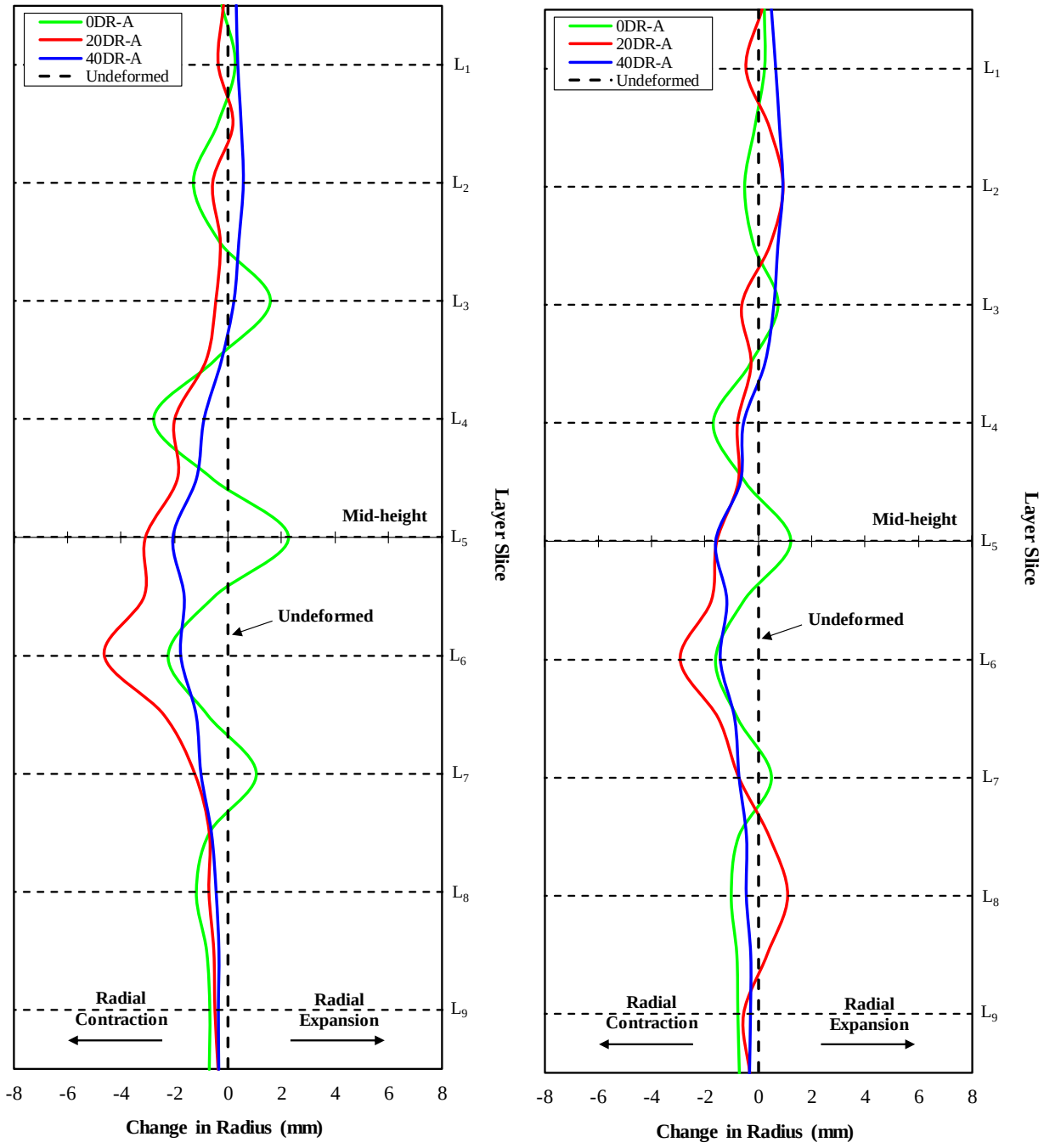

(a) Final compressive cycle before failure

(b) Final tension cycle before failure

Figure 4.2: Comparison of deformed shapes in aluminum specimens obtained from DIC measurements.

4.3. Effect of Auxeticity and Base Metals on Load-Deformation Response

Results indicate that auxetic topology had a direct effect on load-deformation response of the specimens subjected to cyclic loading, however, the observed response was different for each base metal. Auxeticity increased axial strength and ductility in aluminum and steel tubes with improved load-deformation characteristics observed with increasing DR values. Auxetic specimens demonstrated a reduced stiffness due to increased rotations in unit cells, however, this was accompanied by an increase in effective strain in both compression and tension. Increase in DR value led to symmetric hysteretic performance in steel specimens while only tensile performance was observed to be improved for aluminum. While higher strengths in auxetic specimens could in part be attributed to the larger cross-sectional areas (A_0) for the auxetic specimens, the increase in ductility can be attributed to the auxetic phenomenon produced by the cell geometry.

The load-deformation response was gauged using extracted load vs. average vertical strain (ε_A) backbone curves of tested specimens. Curves have been plotted for steel and aluminum specimens in Figure 4.3. Parameters used to quantify the hysteretic performance of specimens included initial elastic stiffness, strain hardening and effective strain in axial tension and compression.

A comparison of peak loads and axial strains for all specimens is presented in Figure 4.4. The results demonstrate that, for the same DR values, the steel topologies exhibited greater peak strengthens than comparable aluminum topologies. This was attributed to the superior mechanical properties of steel compared with aluminum. Furthermore, the results show that for specimens subjected to reversed cyclic loading, topologies with the same DR values experienced similar magnitudes of vertical average strain ε_A regardless of base metal.

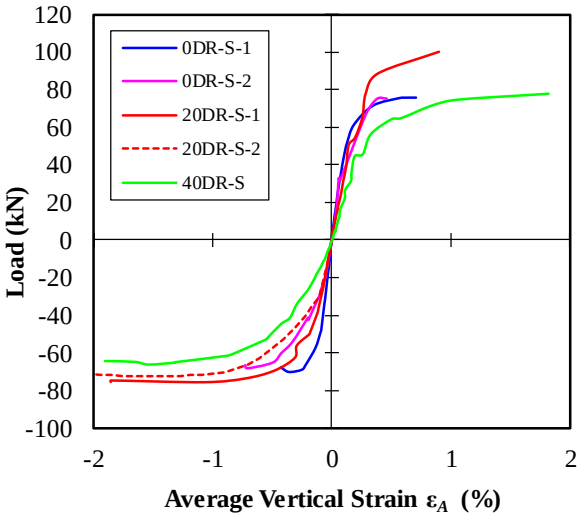

(a) Steel specimens

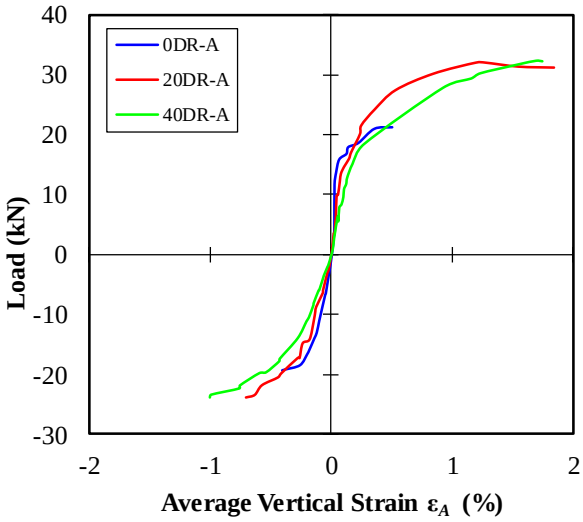

(b) Aluminum specimens

Figure 4.3: Comparison of load-deformation behavior.

Effective strain in both loading directions was quantified using peak average vertical strains (ε_A). In steel, enhanced effective average vertical strain was observed in compression for both auxetic specimens, while vertical strain capacity in tension was significantly enhanced for only specimen 40DR-S. An increase in DR value correlated with symmetric load-deformation response in relation to loading direction, demonstrating that the geometry of cells had a direct effect on load-deformation behavior.

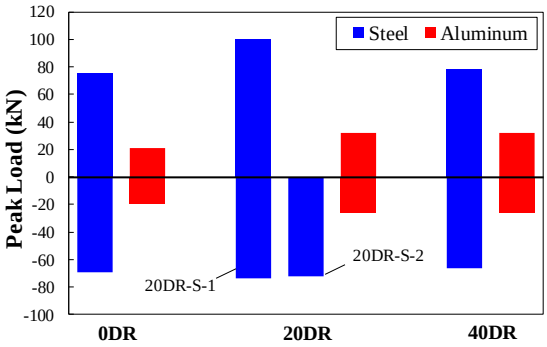

a) Comparison of Peak Loads.

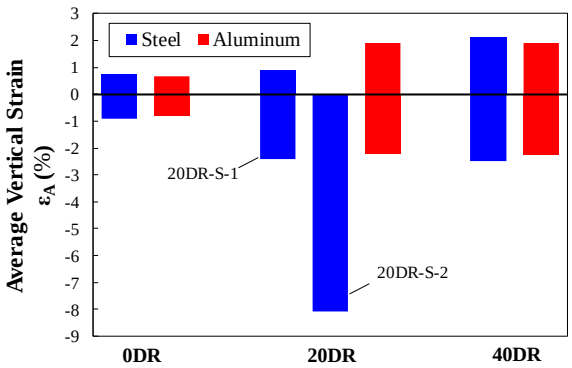

b) Comparison of Effective Average Vertical Strains ε_A in Tension and Compression.

Figure 4.4: Comparison of peak loads and average vertical strains $\boldsymbol{\varepsilon_A}$ for all tested specimens.

In aluminum, a significant enhancement in strength and ductility was observed for auxetic tubes 20DR-A and 40DR-A prominently in tension. Enhancement in compression ductility was

slight and un-symmetric to tension. A high degree of strain hardening was only exhibited in tension.

The effect of cyclic loading on the effective average vertical strain can be observed by the difference in peak compressive strains in 20DR-S-1 and 20DR-S-2 presented in Figure 4.4 (b). Specimen 20DR-S-2, which was subjected to a monotonic compressive deformation, demonstrated a capacity to deform to a value *8.1%* compressive vertical strain ε_A in compression before failure. In contrast, specimen 20DR-S-1, which was subjected to cyclic loading, demonstrated a substantially reduced vertical strain capacity of *2.3%* ε_A. This reduction in effective strain can be attributed to the damage accumulation caused by multiple cycling of specimen 20DR-S-1 through plastic strains.

4.4. Effect of Auxetic Topology on Energy Absorption

The experimental results demonstrate that 20DR and 40DR auxetic topologies exhibit superior energy absorbing capability compared with the 0DR topologies. This is partly due to the superior energy absorbing capability of auxetic cell deformation mechanism when compared to the mechanism observed in non-auxetic tested tubes. Additionally, the difference in cell wall dimensions for the tested specimens also led to higher total absorbed energy for specimens with thicker cell walls.

Due to the auxetic cell geometry, cell rotations dominated the deformation mechanism, hence radial strains were distributed uniformly along the gauge height of the tube. With a wider, more uniform distribution of strains, material plasticity was exhibited by a greater fraction of the auxetic topology, which improved energy absorbing performance compared to the tested non-auxetic topology. Contrarily, plastic strains were observed to concentrate in the mid-section of $2-3$ cell layers before failure in the 0DR specimens. This meant that material plasticity was localized and thus, the 0DR specimens were not able to dissipate as much energy as their auxetic counterparts.

Auxetic specimens showed a significant improvement in energy absorbing capacity with an increase in DR value. On average, energy absorption for 20DR specimens was *180%* greater than the non-auxetic specimens. Further enhancement was observed with an increase in DR; 40DR specimens recorded an energy absorption value *195%* greater energy than 0DR specimens.

Results indicated that cell geometry can be optimized to enhance energy absorption without altering tube dimensions or using additional material. Total energy absorption was dependent on the base metal for a specific cell geometry with steel specimens absorbing significantly greater amounts due to their superior mechanical properties.

Total absorbed energy for all specimens was quantified by calculating the area under their respective load-deformation curves. As tested specimens were not equally porous and did not contain the same amount of material, a normalization was performed against total specimen volume to calculate energy absorption for specimens with equal dimensional parameters. The normalized parameter was termed Specific Energy Absorption (SEA). Values of SEA are presented graphically in Figure 4.5 (a). Results indicated that using steel as base metal increased SEA values approximately by a factor of *3,* when comparing identical steel and aluminum specimens. This effect can be attributed to the higher yield and tensile strengths for steel. Results highlight that the selection of base material with superior mechanical properties can enhance hysteretic performance while maintaining cell geometry.

The effect of only auxetic cell geometry on energy absorption capacity of tubular specimens was quantified using Areal Specific Energy Absorption (ASEA), defined as the total energy absorbed per areal mass (m_A) of specimen; where m_A was defined as the total mass of each specimen divided by the exterior surface area and total energy was the area under the load-deformation curve for each specimen. (Qi et al. 2017) previously used the same approach to study the effect of specimen geometry on energy absorption in lightweight sandwich panels subjected to blast loading. This approach was adopted so that a direct comparison between cell geometries could be conducted without accounting for material properties. ASEA for seven cyclic experimental tests was calculated; higher ASEA values correspond with better energy dissipation and vice versa.

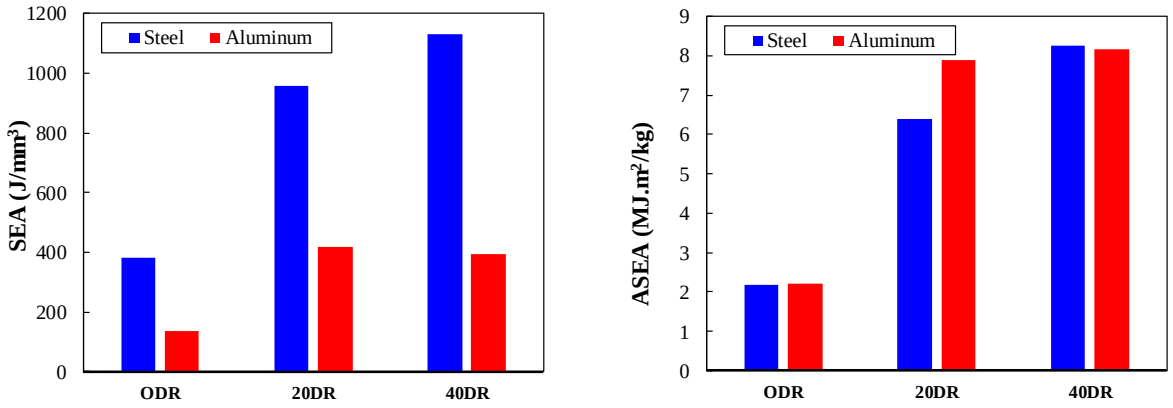

a) SEA b) ASEA

Figure 4.5: Comparison of Energy Absorption for all cyclic tests.

Results for ASEA plotted against DR in Figure 4.5 (b) indicate that introduction of auxetic geometries increased the ASEA for all tubular specimens, with higher ASEA related directly to higher DR value. A continuous increase in ASEA is observed for steel specimens while values for aluminum peaks with specimen 20DR-A. Values for a given cell geometry were almost identical, irrespective of base metal. This suggests that auxetic cell geometries can enhance energy absorption in metal tubes. As energy-absorption is fully-dependent on cell geometry, cell patterns can be modified easily to suit different applications of metal auxetics.

4.5. Effect of Base Material Yielding on Auxeticity

Figure 4.6 shows the effect of base material yielding on average pre- and post-yield values of the Tube Poisson's Ratio (ν_T). For the cyclic loading regime, material plasticity was observed to have an insignificant effect on Poisson's ratio behavior in the auxetic specimens. This is demonstrated by the fact that pre- and post-yield average values for ν_T in all auxetic specimens did not change by a value more than *0.23*. For the non-auxetic specimens, the effect of base material yielding was more pronounced. While all non-auxetic specimens demonstrated a PPR behavior post-yield, pre-yield behavior was highly unpredictable. Identical specimens 0DR-S-1 and 0DR-S-2 demonstrated opposite behavior pre-yield, with 0DR-S-1 exhibiting PPR behavior and 0DR-S-2 exhibiting NPR behavior. Specimen 0DR-A also exhibited NPR behavior pre-yield.

This effect can be attributed to the presence of local instabilities in the non-auxetic specimens. As radial deformations were only calculated in the mid-height layer of the tube, the method of computing Tube Poisson's Ratio v_T may have had an effect on the results.

The insignificant effect of material yielding on the Tube Poisson's Ratio behavior in the tested auxetic tubes can be attributed to their unique deformation mechanism. A visual representation of deformed shapes in Section 4.2 showed that auxetic behavior was a result of induced geometric instability, which caused in-plane rotations in the cells and led to the formation of plastic hinges in cell walls. These in-plane deformations were more stable due to the tubular geometry, which formed a reactive hoop stress in the circumferential direction. Therefore, the formation of plastic hinges in auxetic cell walls did not affect average NPR behavior significantly. Contrarily, the non-auxetic mechanism was dominated by cellular instability. This likely led to the plastic hinging of cell walls in the radial direction. Out-of-plane deformations in individual cell layers produced high second order effects. These second-order effects were further increased by the formation of mid cell plastic hinges which affected PR behavior significantly.

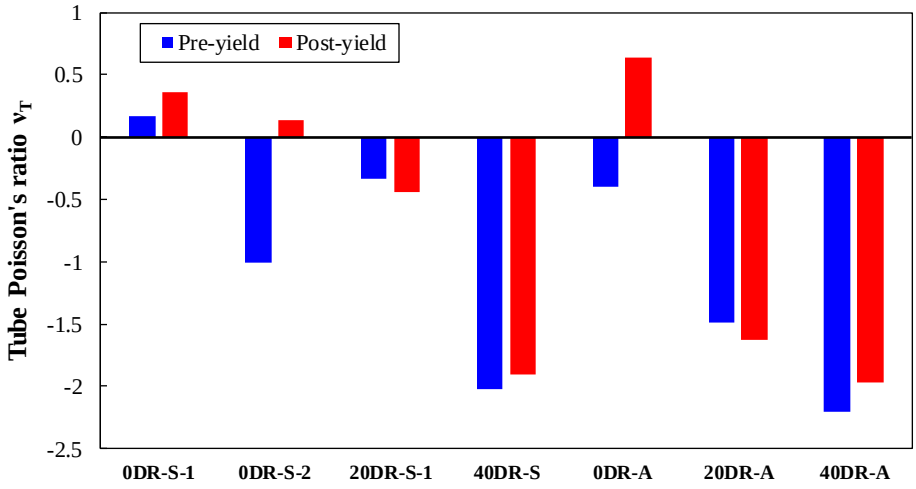

Figure 4.6: Effect of base material yielding on Tube Poisson's Ratio ($\boldsymbol{v_T}$)

In general, an increase in DR value for the auxetic specimens led to an increase in magnitude for v_t. This is highlighted by the fact that 40DR specimens, irrespective of base metal, demonstrated a greater magnitude of average Tube Poisson's Ratio v_T than the 20DR specimens.

4.6. Effect of Loading Regime on Properties of Auxetic Specimens

The effect of loading regime was substantiated using data from just a single experiment i.e. the monotonic test for specimen 20DR-S-2. As just one monotonic test was conducted, a direct comparison could only be conducted between specimens 20DR-S-1 and 20DR-S-2.

Figure 4.7 shows the effect of cyclic and monotonic compressive loading on the response of 20DR steel auxetic tubes 20DR-S-1 and 20DR-S-2. The comparison indicates that although the 20DR-S specimens share similar peak strengths in compression, the effective compression strain range of the monotonically loaded 20DR-S-2 was substantially greater than that of the cyclically loaded 20DR-S-1 which failed in tension. Reduction in effective strain range in compression for the cyclically loaded specimen can be attributed to the accumulated damage caused by cycling the specimen through high plastic strains. This was not the case for the monotonically loaded specimen, which failed after withstanding significantly higher vertical strains. Results suggest that under static loading conditions, auxetic tubes can be designed to exhibit substantial axial deformations, thereby enhancing their ductility.

The failure mechanisms were also different for the loading regimes. Specimen 20DR-S-1, which was subjected to cyclic loading, failure due to tensile rupture of the cell walls while the monotonically loaded specimen 20D-S-2 was considered to fail due to the tube densification; this occurred when opposing cell walls came into contact. Although only substantiated by a single data point, the result suggests that perhaps auxetic tubular structures may be better suited for compression load scenarios.

The comparison of average Tube Poisson's Ratio v_T (Figure 4.7) showed that the monotonically loaded specimen demonstrated significantly higher magnitudes before and after yielding, when compared to the cyclically loaded specimen. However, a direct comparison cannot be conducted as different processing techniques were adopted to calculate v_T for both loading regimes. This owes to the fact that an incremental methodology was employed for calculating strain in the cyclic loading protocol, while strains were calculated relative to the initial undeformed geometry for the monotonically loaded specimens.

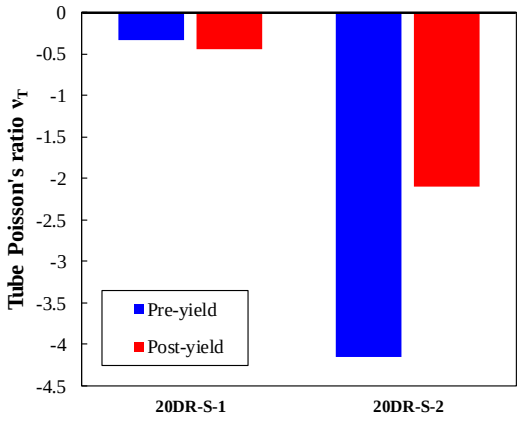

Figure 4.7: Comparison of Tube Poisson's Ratios ($\boldsymbol{v_T}$) for cyclic and monotonic loading.

4.7. Effect of Auxetic Topology on Failure Mode

Under the action of cyclic loading, the failure mode for all tubular specimens regardless of DR value was by tensile rupture of the cell walls at the location of minimum cross-sectional area. For non-auxetic tubes, the cell walls experienced a predominantly uniaxial stress state with visible necking observed in the rupture zones. For auxetic tubes, tensile failure was precipitated by a combined flexural-axial stress state caused to the rotation of the unit cells. Inspection of the rupture zones in the auxetic tube cell walls showed signs of plastic hinging rather than necking.

4.8. Effect of Manufacturing Process on Base Material Properties

The low tensile strength of the non-auxetic 0DR-A aluminum tube, equal to roughly 50% of the theoretical strength predicted using coupon test data, suggests that the base material properties of the 6060-T66 aluminum may have been adversely affected by the laser-cutting process. This phenomenon was not observed in the non-auxetic 0DR-S-1 and 0DR-S-2 steel tubes which had tensile strengths comparable to those of the steel coupons.

The low structural strength observed in 0DR-A was attributed to heat generated by laser-cutting processes having an adverse effect on the mechanical properties of metals (Shandookh 2018). The formation of a Heat Affected Zone (HAZ) around the boundary of the cut edges reduces the mechanical properties near the edge compared with the bulk material. Although all metals experience HAZ when subjected to high temperatures, aluminum alloys are especially challenging to cut using laser techniques due to the high reflectivity of the material which requires more power or slower cutting speeds (Eiroa 2015). The high thermal conductivity of aluminum also leads to a

larger HAZ which can generate micro-cracking, stress concentrations and, changes in base material properties. Coupon tests performed by Shandookh (2018) on AA 2024-T3 and AA 7075-T6 aluminum demonstrated that tensile coupons prepared using laser cutting processes were 34% weaker than comparable CNC-cut coupons. The decrease in mechanical properties reported by Shandookh (2018) is comparable to the reduction in failure strength observed for specimen 0DR-A during testing. It is thereby likely that the auxetic aluminum tubes 20DR-A and 40DR-A experience comparable reductions for similar reasons.

The extension of the HAZ beyond the laser cut edge has been shown to be relatively narrow (Araujo et al. 2003; Stournaras et al. 2009). However, the cell walls of aluminum specimens were very thin (approx. *2-4 mm* wide and *5 mm* thick) which meant that the tubes structures were very sensitive to HAZ. Increase in width of cell walls was expected to reduce sensitivity to HAZ, with a rise in fraction of unaffected base material. The effect of laser cutting was also visually apparent in aluminum specimens which had roughened laser cut edges as opposed to smooth cut edges observed in the steel specimens.

The noticeable loss in the strengths of aluminum tubular specimens could be directly attributed to the formation of a HAZ by the manufacturing process, the material parameters need to be modified accordingly to accurately predict the mechanical properties of tubes. This modification was especially pertinent for conducting numerical analyses such as FE simulations. Greatest accuracy in predicting the properties of the HAZ can be achieved if the manufacturing parameters such as power, speed and dimensions of laser are known. However, these parameters were unknown for the tested specimens. Therefore, empirical modifications were applied to material models based on relevant literature while taking the dimensional parameters of tubes into consideration. For future research, it is recommended that the extent of the HAZ in the laser cut specimens is calculated based on laser parameters as well as separate experimental tests of laser cut coupons, so that greater accuracy can be achieved in predicting material behavior.

Chapter 5. Finite Element and Simplified Macromechanical Modeling

5.1. Overview

This chapter presents the finite element and simplified macromechanical modeling techniques aimed at predicting the response of the auxetic and non-auxetic topologies studied during the experimental phase. This is achieved through two analyses, first by generating hysteretic load-deformation predictions for auxetic and non-auxetic tubes using FE simulations, followed by the development of simplified strength equations based on equilibrium of moments to predict the ultimate tensile strength of the tubular specimens. All numerical analyses were performed using the commercial finite element software LS-DYNA (LSTC 2018) while pre- and post-processing of data was conducted using LS-PrePost (LSTC 2002) .

5.2. Summary of Results

Table 5-1 provides a summary of the results from FE and simplified macromechanical computations of tensile strength for all tubular specimens. The actual tensile failure loads recorded during the experiments (T_e) have been compared against the predicted failure loads computed using FE simulations (T_p^{FEA}) as well as the predictions for the same calculated using the strength equations (T_e^{STR}).

Table 5-1: Summary of Predicted and Experimental Results.

			Finite Element Analysis (FEA)		Strength Equation	
	Specimen	Failure Load T_e (kN)	Predicted Failure Load T_p^{FEA} (kN)	$\frac{T_p^{FEA}}{T_e}$	Predicted Failure Load T_p^{STR} (kN)	$\frac{T_p^{STR}}{T_e}$
Steel	0DR-S-2	75.2	82.6	1.09	70.0	0.93
	20DR-S-1	100.2	94.9	0.95	88.3	0.81
	40DR-S	78.0	87.8	1.12	81.6	0.88
Aluminum	0DR-A	21.2	23.3	1.10	20.1	0.95
	20DR-A	32.0	39.2	1.22	30.2	0.98
	40DR-A	32.2	30.9	0.96	29.5	0.86
			Avg.	1.07	**Avg.**	0.90
			StD.	0.1	**StD.**	0.06
			CV.	9.57%	**CV.**	6.99%

5.3. Constitutive Models used for Analysis

This section presents the material models used in the finite element analysis and simplified modeling of the auxetic and non-auxetic tubes tested in the experimental program. The true stress-strain relationships for steel and aluminum coupons are derived for use in finite element analysis. In addition, an empirical modification to the mechanical properties of aluminum is described to empirically account for the reduction in base material properties due to the laser manufacturing process.

5.3.1 Material Models

The true stress-strain relationships for the steel and alumium materials were necessary for finite element analysis. Engineering stress-strain curves for the metals, presented in Section 2.4, were converted into true stress-strain relationships using the conversion formulae presented in Eqs. (6) and (7). In this manner, true strain (ε_T) and true stress (σ_T) were obtained following:

$$\varepsilon_T = \ln(\varepsilon_E + 1) \tag{6}$$

$$\sigma_T = \sigma_E . e^{\varepsilon_T} \tag{7}$$

where ε_E and σ_E are the experimental coupon nominal strain and stress values, respectively. True stress σ_T was only calculated up to the onset of necking and extrapolated to true strain ε_T at failure.

A two-stage approximation of the true stress-strain curves was used in the finite element analysis. For the initial elastic stage, elastic modulus (E) and yield stress (σ_y) were used to model behavior. The plastic stage was defined through the use of an Armstrong-Frederick kinematic hardening model (Jiang and Kurath 1996) to capture the Bauschinger effect during cyclic loading. Material plasticity was defined based on kinematic hardening modulus (C) and a plasticity factor (γ) which were unknown for the base materials used. As this numerical model is a built into the DAMAGE_3 material model in the FE analysis software, a series of predictive FE analyses were conducted to compute the unknown parameters. A hit-and-trial methodology was used to obtain values for C and γ such that the true stress-strain response would match the experimental results. Poisson's ratios and mass densities for the base metals were acquired from relevant material specifications (DIN 2005; DIN 2003).

A fully integrated shell element formulation was implemented which uses a Bathe-Dvorkin (Dvorkin and Bathe 1984) transverse shear treatment to eliminate w-mode hourglassing effects. Other modes of hourglassing are also eliminated using this formulation by the use of 4 in-plane integration points except for the purpose of calculating transverse shear, where only 1 in-plane integration point is considered. This element formulation corresponds to formulation 16 (EQ16) in LS-DYNA. A single 4-node quadrilateral element with *5* through-thickness integration points was modeled, measuring *2 mm x 2 mm.* Shell thickness was *5 mm.* Five in-plane integration points were chosen such that the error between output stresses at the outermost integration points and the element surface could be minimized.

The bottom boundary of the element was restrained against all degrees of freedom while only vertical (Z) displacement was allowed on the top boundary. Vertical displacement was applied to the top boundary in the tensile direction. Total vertical force and displacements were extracted to compute true stress-strain behavior for both base metals.

Final values for material model parameters C and γ that produced accurate stress-strain response have been tabulated in Table 5-2. For steel, a value of $C = 3000$ and $\gamma = 10$ were found to accurate match coupon test data. Similarly, a value of $C = 700$ and $\gamma = 10$ were found to accurate match coupon test data for aluminum, Figure 5.1 shows a comparison of true stress and strain data for the experimental coupon tests as well as the single-element FE analyses for both

base metals. The FE model captured steel and aluminum coupon material yielding and hardening accurately, validating the kinematic hardening approach adopted to describe stress strain behavior. Therefore, the same material model was adopted for further FE analyses.

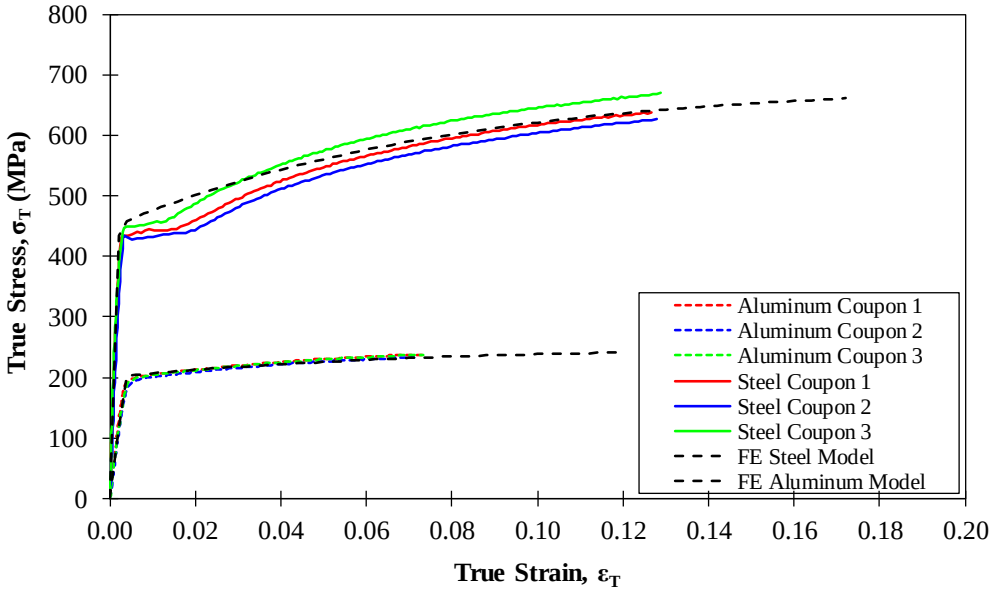

Figure 5.1: Comparison of true stress-strain response for metal coupons.

5.3.2 Empirical Modification to Aluminum Material Model

Due to the effects of laser cutting on material properties summarized in Section 4.8, tensile properties of aluminum specimens were affected noticeably. In order to account for this behavior, the aluminum material properties were empirically modified to incorporate strength loss observed during the aluminum tube tests.

Due to a lack of data in the literature regarding HAZ in thinly cut aluminum sheets, empirical modification factors were computed. An average value for reduction in true yield stress (σ_y) and true ultimate stress (σ_u) was calculated using values using values reported in literature (Aalberg et al. 2001; Stathers et al. 2014; Shandookh 2018; Nazemi and Ghrib 2019) for welded and laser cut aluminum alloys. A HAZ modification factor (ϕ) of *0.60* was applied to true coupon yield stress (σ_y) and ultimate stress (σ_u) for specimen 0DR-A. As for specimens 20DR-A and 40DR-A, a *0.80* reduction factor was applied. This was based on a reasonable assumption that thinner cell walls would be more sensitive to the HAZ while a greater unaffected zone would be

present in thicker cell geometries. No changes were made to the elastic modulus (E). Final material inputs for the FE models have been presented in Table 5-2.

Table 5-2: FE modeling parameters for reverse-cyclic analysis of tubular specimens.

Material	Mass Density ρ (kg/mm^3)	Kinematic Hardening Modulus C (MPa)	Plasticity Factor γ	Elastic Modulus E (GPa)	Strength Modification (ϕ)	Yield Stress σ_y (MPa)	Ultimate Strain ε_u (%)	Ultimate Stress σ_u (MPa)	Poisson's Ratio (ν)
Steel	7.8 x 10^{-6}	3000	10	217.5	1	438.8	10.15	717.3	0.30
Aluminum	2.7 x 10^{-6}	700	10	57.2	0.6 for 0DR-A 0.8 for 20DR-A and 40DR-A	117.9 for 0DR-A 157.2 for 20DR-A and 40DR-A	17.19	151.6 for 0DR-A 202.3 for 20DR-A and 40DR-A	0.33

5.4. Finite Element Modeling

This section describes the FE modeling procedure and relevant modeling parameters employed to generate load-deformation responses of the auxetic and non-auxetic tubes.

5.4.1 Modeling and FE Analysis of Ductile Metal Tubes

3D test specimen geometries were created in AutoCAD and imported to LS-PrePost. Imported geometries were meshed into 4-node quadrilateral shell elements. Element formulation was the same as that of the coupon test validation FE analysis. A fully integrated shell element formulation, corresponding to LS-DYNA formulation 16, was implemented to eliminate w-mode hourglassing effects using the Dvorkin and Bathe (1984) transverse shear treatment. A total of *5* through-thickness integration points were selected to minimize errors between output stresses calculated at the outer-most integration points and the exterior surface of the shell elements. Only the gauge height (H_G) was modeled as the additional length of tubes was assumed to be completely rigid and was excluded to save computational time. Material properties were integrated via the DAMAGE_3 material model as described in Section 5.3.1. Empirically modified constitutive material models were used for each specific specimen to account for strength reduction due to manufacturing, if any.

Material model inputs were followed by assigning test assembly boundary conditions. The base of the tube was restrained against all degrees of freedom. The top nodes of the tube were restrained against all degrees of freedom except for vertical (Z-axis) displacement. AUTOMATIC_SINGLE_SURFACE contact was selected as the contact parameter for all specimens. Implicit analysis was carried out for all ductile metal tube specimens with a *1 ms* timestep corresponding to a vertical displacement increment of *0.02 mm*. All specimens were subjected to the same displacements recorded across gauge length H_G in their respective experiment. A typical FE model for 20DR-S-1 is presented in Figure 5.2.

The data acquired from all tests included nodal deformations in three dimensions and axial reaction forces. Results for each individual FE simulation are discussed in Section 5.6.

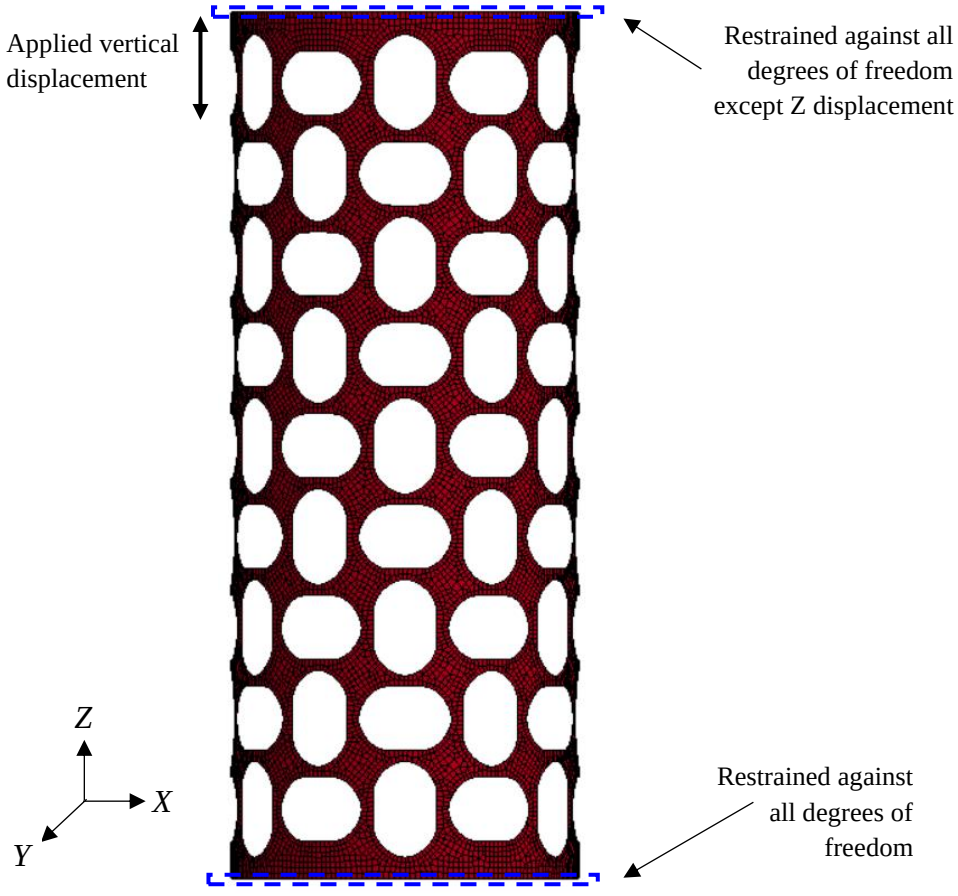

Figure 5.2: Typical finite element model for 20DR-S-1.

5.4.2 Mesh Convergence Study

Mesh size was finalized after conducting a mesh convergence study using the FE model for 20DR-S-1 on LS-DYNA. Mesh size was varied between *5 mm* and *1 mm*. The model was subjected to a short loading protocol with one cycle each at $0.5\Delta_0$, $1.0\Delta_0$, $1.4\Delta_0$, $1.96\Delta_0$ and $2.74\Delta_0$. Peak positive and negative axial load values for each applied deformation was compared. Table 5-3 shows the percentage difference between the mesh sizes, taking *1 mm* mesh as the baseline. Convergence was achieved at a mesh size of *2 mm*, with minimal error between the *1 mm* mesh. A *2 mm* mesh size was selected for all further FE computations. Figure 5.3 compares the predict load-deformation response for each mesh size evaluated.

Table 5-3: Percentage differences in cyclic peak loads (Mesh sensitivity).

Mesh Size	**Applied Axial Displacement (mm)**									
	0.15	**-0.15**	**0.30**	**-0.30**	**0.42**	**-0.42**	**0.59**	**-0.59**	**0.82**	**-0.82**
5mm	7.9%	8.2%	10.8%	11.4%	5.8%	6.4%	3.7%	4.6%	4.4%	5.3%
3mm	4.2%	4.3%	5.0%	5.2%	2.8%	3.2%	3.9%	4.5%	5.2%	6.3%
2mm	1.5%	1.6%	1.1%	1.3%	1.4%	1.5%	2.3%	2.5%	1.0%	2.1%
1mm	0.0%	0.0%	0.0%	0.0%	0.0%	0.0%	0.0%	0.0%	0.0%	0.0%

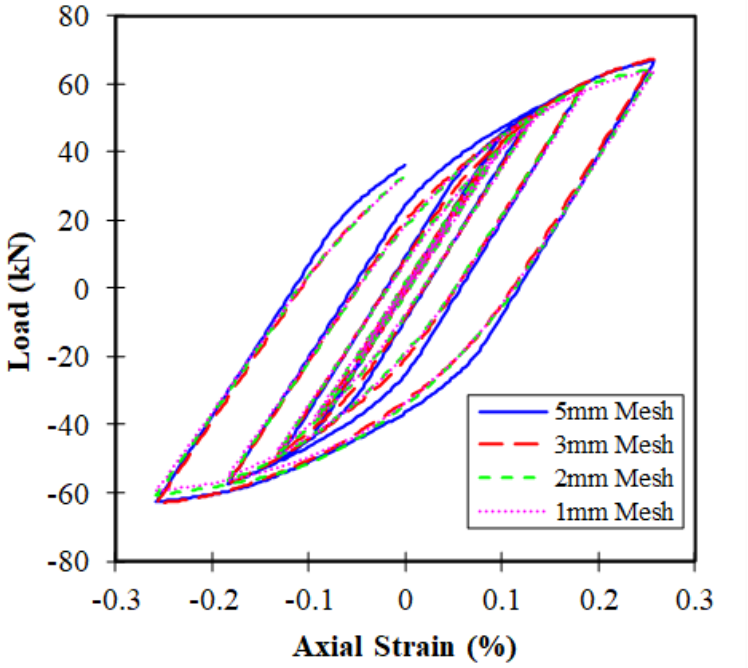

Figure 5.3: Comparison of peak axial loads for mesh sensitivity.

5.5. Strength Equations for Metal Tubes

Two simplified strength equations were derived to predict the tensile load carrying capacity of ductile metal tubes. One is a strength equation for non-auxetic tubes based on tensile strengths extracted from material coupon tests. The other is for auxetic tubes and is derived based on the principle of equal energy using an idealized until cell undergoing concentrated plastic hinging in the cell walls. This section describes the derivation of the strength equations. A comparison of predicted strengths to experimental results is presented in Section 5.6.

5.5.1 Non-Auxetic Ductile Metal Tubes

It was observed that all non-auxetic specimens failed in tension while under pure axial stress. The mode of loading and failure was identical to the coupon as no rotations were induced in the non-auxetic specimens. Therefore, the following simplified equation, based on ultimate coupon tensile strengths (σ_u), was derived to predict failure load (T).

$$T = n\sigma_u t_w w_r \tag{8}$$

Where n is the number of cells in a horizontal cell layer, σ_u is the ultimate coupon tensile stress for the base metal, t_w is the tube thickness and w_r is the measured thickness of each cell wall.

5.5.2 Auxetic Ductile Metal Tubes

The geometry of the unit cell for the macro-mechanical strength model is illustrated in Figure 5.4. For simplicity, the auxetic cylinder is "unrolled" to create the idealized planar topology illustrated in Figure 5.4 (a). The analysis is concerned with the behavior of a unit cell located at mid-height of the auxetic topology. Several simplifying assumptions were made regarding the deformation of this cell. First, vertical and lateral cellular deformations, illustrated in Figure 5.4 (c), are caused by rotation of the cell about its geometric centroid C_g. This implies that axial deformations of the unit cell about both principal axes are negligible compared to the relative to deformations caused by cellular rotation. Furthermore, lateral dilation of a given unit cell is unopposed by adjoining cells. That is, there is no horizontal force acting across the cell, which is only reasonable near mid-height of the auxetic topologies away from the rigid boundaries. Finally, just prior to incipient failure, the unit cell is assumed to rotate by an angle θ_c about its centroid.

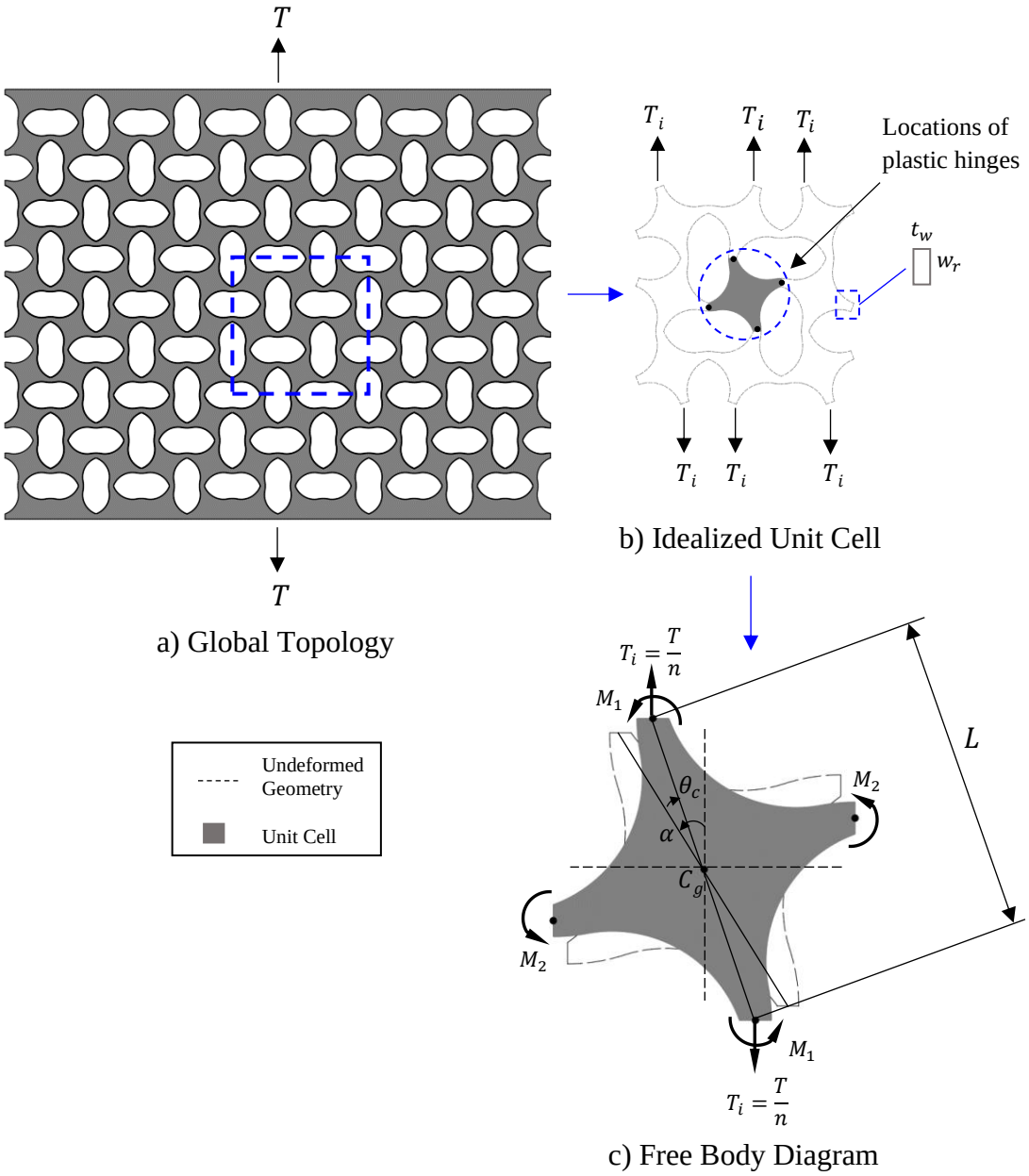

Figure 5.4: Idealized deformed configuration of unit cell under uniaxial tension.

The assumptions required to simplify the problem have two physical implications. First, the vertical axial strain in the unit cell, ε, is related to the rotation at failure θ_c failure according to:

$$\varepsilon = \frac{\cos(\alpha - \theta)}{\cos(\alpha)} - 1 \tag{9}$$

The second is that the Poisson's ratio of the unit cell $\nu = -1$.

The strength of the idealized unit cell can be established considering the free-body diagram, shown in Figure 5.4 (c). The unit cell is subject to a vertical tensile force T_i equal to the total tensile load T divided by the number of rows of unit cells, n. The force T_i acts at the ends of the vertical struts and cause the cell to rotate through an angle θ_c about its centroid. At failure, a series of plastic hinges will form at the ends of each of the struts. Each plastic hinge has a rectangular cross-section with width equal to the tube wall thickness (t_w) and height equal to the minimum depth of the unit cell (w_r).

The ultimate capacity of the unit cell is assumed to be governed by the moment capacity M_1 of the "primary hinges" located in the vertical struts. This is consistent with the location of tensile fracture observed during the experiments due to the combined effect of axial force-bending moment interaction. Therefore, the strength of the primary hinges, M_1, when subjected to tensile force T_i can be estimated by means of an idealized elasto-plastic beam-column interaction relationship given in Eq. (10):

$$M_1 = M_u \left(1 - \left(\frac{T_i}{T_u}\right)^2\right) \tag{10}$$

where M_u and T_u are the ultimate flexural and tensile capacities of a rectangular cross-section, respectively. For the case of pure flexure, $M_u = \frac{\sigma_u t_w w_r^2}{4}$, while for pure tension $T_u = \sigma_u t_w w_r$.

When the primary hinges attain their moment capacity, it was assumed that the moment M_2 developed in the "secondary hinges" was equal to the plastic moment capacity of the strut:

$$M_2 = \frac{\sigma_y t_w w_r^2}{4} \tag{11}$$

Equilibrium of forces in Figure 5.4 (c) requires that the sum of moments about the centroid equals zero, such that the tensile force T_i is equal to:

$$T_i = \frac{2(M_1 + M_2)}{Lsin(\alpha - \theta_c)} \tag{12}$$

Substituting Eqs. (10) and (11) into Eq. (12) yields the following expression or T_i:

$$T_i = \frac{\sigma_u t_w w_r^2 \left(1 - \left(\frac{T_i}{\sigma_u t_w w_r}\right)^2\right) + \sigma_y t_w w_r^2}{2Lsin(\alpha - \theta_c)} \tag{13}$$

The expression for T_i given in Eq. (13) yields a second-degree polynomial. For a given rotation at failure θ_c, a solution for T_i can be obtained using the fixed-point iteration numerical technique or similar root-finding algorithm (Hamming, 2012). However, solutions to Eq. (13) requires values of θ_c to be known, or at least estimated, prior to computing T_i.

Once a solution to Eq. (13) is obtained, the total load carried by the auxetic tube T can be found:

$$T = n \cdot T_i \tag{14}$$

Where n is the number of columns of auxetic cells in the topology. For the topologies studied in this research, $n = 12$.

Input values for θ_c were based on the theoretical inelastic rotation capacity of a cell wall, which was estimated based on the following relationship:

$$\theta_c = \left[\mu_\phi - 1\right]\phi_y L_p \tag{15}$$

Where μ_ϕ is the curvature ductility of the auxetic cell, ϕ_y is the yield curvature ($\phi_y = \frac{2\sigma_y}{Ew_r}$) and L_p is the length over which inelastic curvatures are constant. The value of L_p was assumed to be equal to minimum depth of the unit cell wall w_r, which is roughly equal to the length over which inelastic deformations were observed in the cell walls after the tests. Therefore, the rotation capacity θ_c reduces to:

$$\theta_c = [\mu_\phi - 1]\frac{2\sigma_y}{E} \tag{16}$$

Values of μ_ϕ used in the analysis were empirically derived based on the observed rotations at tensile failure θ_c^{exp}shown in Table 3-1. As was previously discussed in Chapter 4, the 40DR tubes underwent greater rotations prior to failure than 20DR tubes. In addition, steel topologies experienced greater overall rotations than aluminum ones. Furthermore, the results in Section 4.4 suggest that it is possible to normalize certain mechanical properties of the metal auxetic topologies, namely specific energy absorption, with respect to base material properties. These observations combined to provide the impetus to develop an empirical relationship for μ_ϕ based on experimental θ_c^{exp} as a function of material and geometric properties of the auxetic topologies.

As illustrated in Figure 5.5, the curvature ductility μ_ϕ of the auxetic unit cells can reasonably be approximated according to:

$$\mu_\phi = 14\frac{DR \cdot E}{\gamma} \tag{17}$$

where DR is the deformation ratio (in %), E is the modulus of elasticity of the base material (GPa), and γ is bulk density of the material (kg/m^3). It must be noted that the empirical nature Eq. (17) is calibrated directly to the material and geometric properties of the auxetic tubes studied in this research. Accordingly, caution should be exercised when applying Eq. (17) to metal auxetic topologies that are considerably outside the range of parameters of this study.

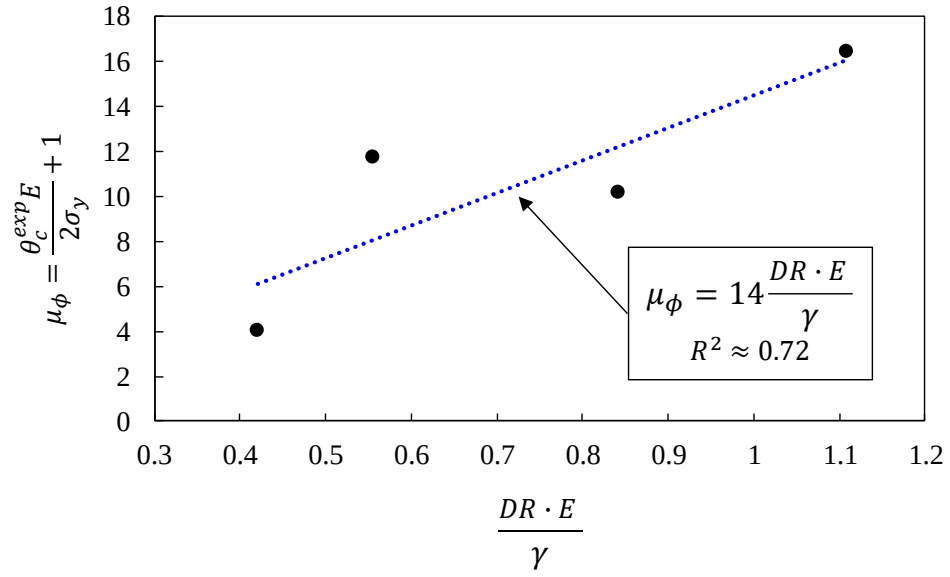

Figure 5.5: Approximation of curvature ductility $\boldsymbol{\mu_\phi}$ for auxetic unit cell wall.

5.6. Discussion of Results

5.6.1 Finite Element Analysis

The FE models adequately describe general material behavior and Poisson's ratio with reasonable accuracy for all specimens once empirical modifications are applied to material properties. In general, there was a tendency to overpredict axial strengths but higher values are justifiable as accumulated damage due to cycling at plastic strains was not incorporated into numerical calculations. Hardening in tension and loss of strength in compression due to instability was captured with good accuracy. The models can be refined further by incorporating material damage and failure to generate more accurate results.

The results of the FE analysis and calculated failure loads (T) using the simplified strength equations for steel and aluminum specimens are presented in Figure 5.6 and Figure 5.7, respectively. Load deformation response is presented using stress-strain response while Tube Poisson's Ratio (v_T) is displayed using a radial strain (ε_R) vs. average vertical strain (ε_A) diagram for each specimen. Failure and damage accumulation during cyclic loading were not modeled and have not been discussed.

The FE analysis of steel specimens predicted the load-deformation behavior moderately well. Initial yield slopes for all specimens were predicted with good accuracy. The model for 0DR-S-2 overestimated peak loads in tension and compression; showing a maximum discrepancy of *10.6%* and *9.8%*, respectively. However, the FE model for 0DR-S-2 had a *12.1%* higher cross-sectional area, which also accounted to for the discrepancy in strength. The model for 20DR-S-1 underpredicted the peak tensile and compressive strength of the tube by *5.3%* and *4.6%*, respectively. The 40DR-S model overpredicted the peak strengths of the tube by *12.5%*, however, greater softening was predicted in compression than the experimental results; peak compressive load was *6.6%* lower than the experimental value. Strain hardening in tension was captured well for all specimens. The models also captured the loss in compressive strength due to instability, with values in compression within *11%* of the experimental results. Unloading slopes were consistent with experimental data.

All steel FE models accurately captured the general Poisson's ratio behavior for the tubes although exact values of v_T could not be predicted. Specimen 0DR-S-2 was accurately predicted to demonstrate PPR behavior while NPR in specimens 20DR-S-1 and 40DR-S was accurately predicted. The general trends in slopes matched the experimental data for the steel tubes. The FE model for specimen 0DR-S-2 predicted a residual mid-height radial expansion greater than the actual experimental specimen. For specimens 20DR-S-1 and 40DR-S, only minor permanent mid-height radial residual contraction was predicted, which matched the experimental results.

The modified aluminum FE models predicted the load-deformation behavior reasonably well. The FE models reproduced the initial yield slopes for with good accuracy. Strain hardening in tension was captured well for all specimens, along with the declining compressive strength due to instability. Unloading slopes were also consistent with experimental results. The 0DR-A modified FE model demonstrated similar behavior to its experimental counterpart. Strength in tension and compression were overpredicted by *15.3%* and *10.1%*, respectively. The model for 20DR-A also overpredicted the peak tensile and compressive strengths of the tube with a maximum discrepancy of *22.6%* and *8%*, respectively. However, the 40DR-A model underpredicted the peak tensile and compressive strength of the tube, with a *4%* and *11.4%* discrepancy in values, respectively. Results showed that the empirical modifications applied to the

aluminum material models yielded good results, except for the tensile strength in specimen 20DR-A.

The general Poisson's ratio behavior for the aluminum tubes was predicted accurately, although exact values of v_T were not reproduced. The slopes of the strain plots for aluminum matched the general trends observed in the experimental data. The models for all three aluminum specimens predicted the PPR/NPR behavior well, along the residual radial deformation seen during the experiment. PPR in 0DR-A was accurately predicted while NPR behavior was replicated well for 20DR-A and 40DR-A. Models also predicted the residual mid-height expansion for 0DR-A and contraction for specimens 20DR-A and 40DR-A.

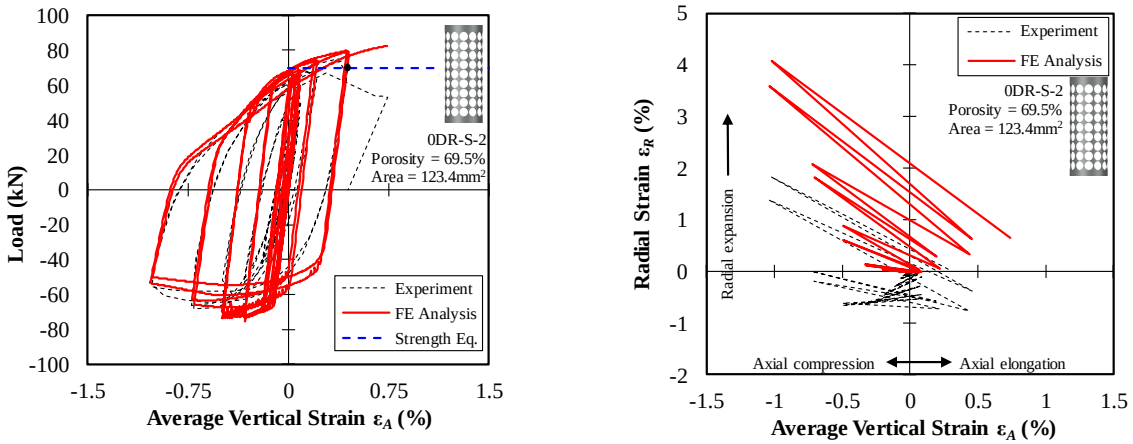

a) 0DR-S

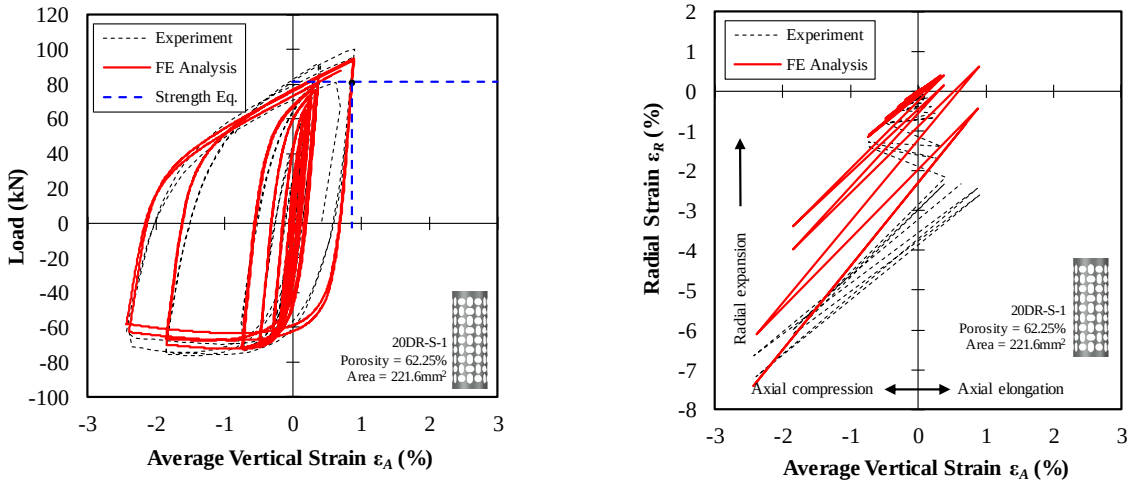

b) 20DR-S

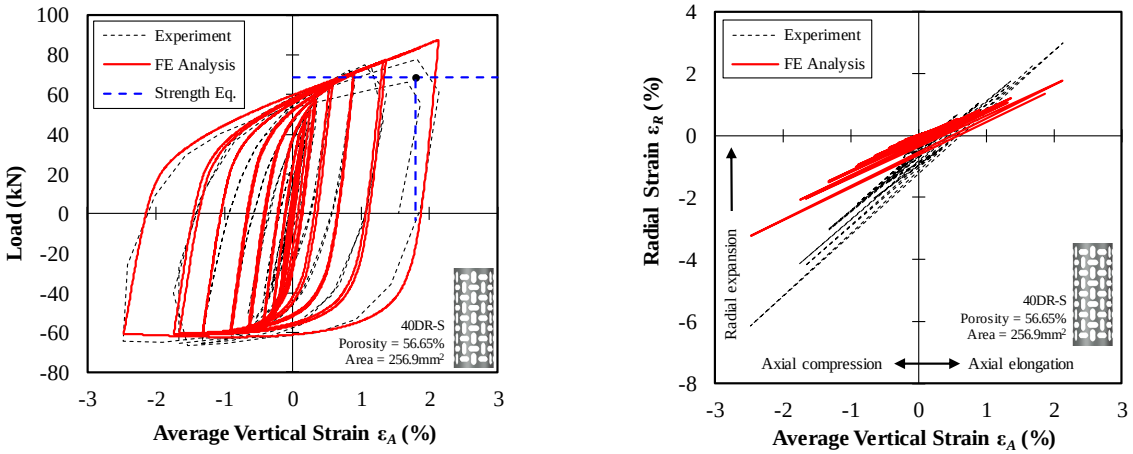

c) 40DR-S

Figure 5.6: Comparison of FE results and experimental data for steel specimens

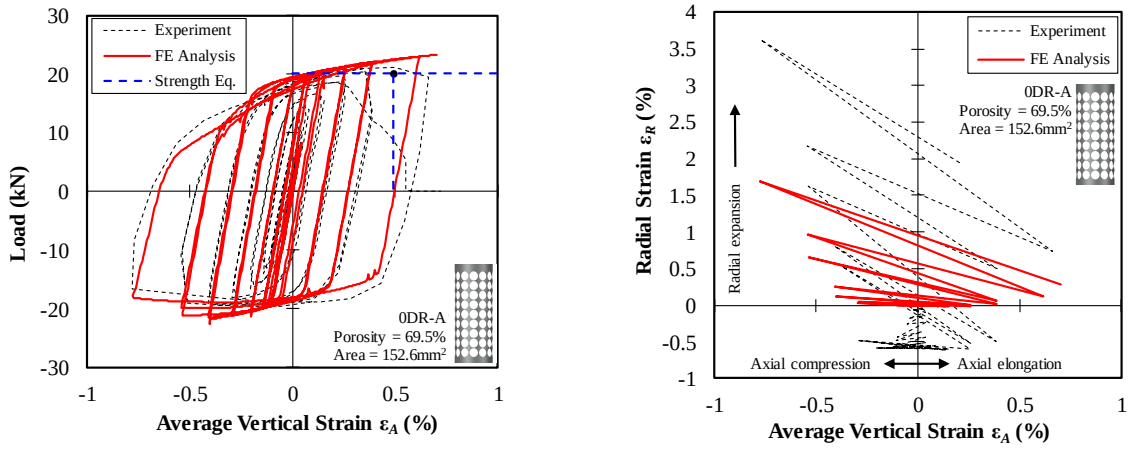

a) 0DR-A

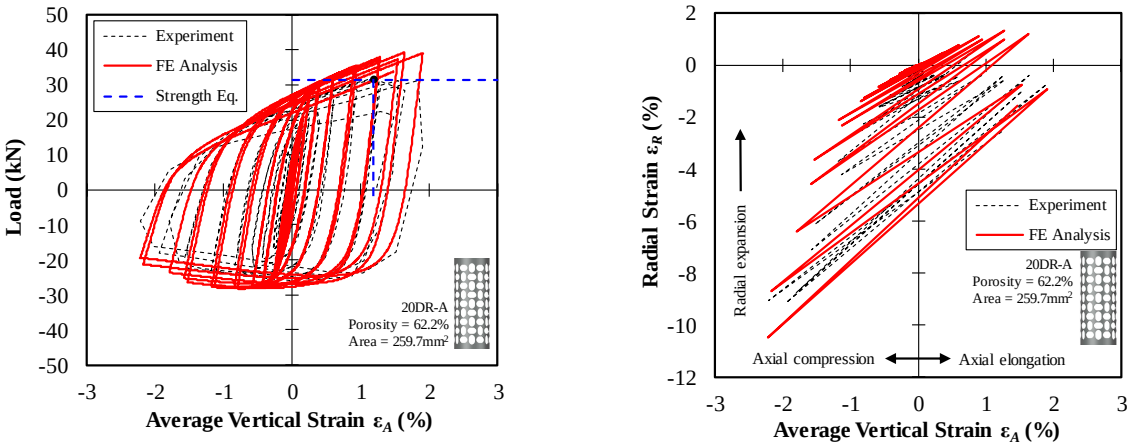

b) 20DR-A

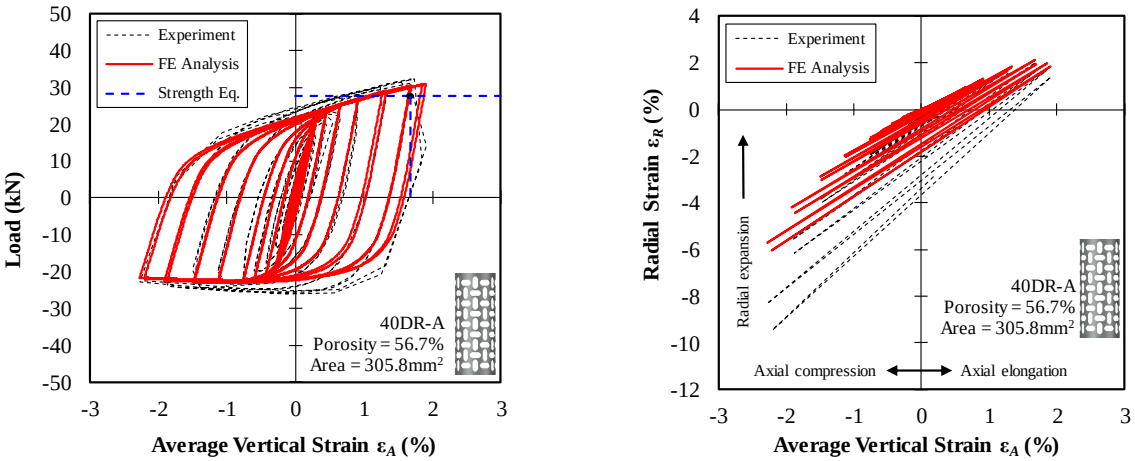

c) 40DR-A

Figure 5.7: Comparison of FE data and experimental data for aluminum specimens

5.6.2 Analytical Models for Tube Tensile Strength

Table 5-4 summarizes the inputs and results of the macromechanical strength analysis. For 0DR specimens, Eq. (8) was used to obtain the tensile load at rupture. For the auxetic specimens, 20DR and 40DR equations (13) and (16) were used to calculate peak tensile strength. Figure 5.6 and Figure 5.7 show predicted tensile strength T and strain ε at peak strength against that of experimental load versus axial load relationships.

The following observations were made upon calculating strengths and comparing results with experimental values:

- Peak load seems to be predicted reasonably well for both auxetic and non-auxetic topologies. Load predictions for steel and aluminum were consistent with a *13%* average discrepancy for steel and *7%* for aluminum specimens.

- Estimated rotations at peak load were reasonably close to those calculated during the experiment. Errors in estimation was seen to increase with an increase in DR value. In steel, for instance, predicted angles for 20DR-S-1 and 40DR-S were *63%* and *94%* accurate, respectively. However, some caution is needed while using these quantities as empirically calibrated equations were used to compute curvature ductility.

- Predictions of axial strain at peak load are fair, although accuracy was observed to increase with increasing DR. In the model, unit cell deformations were assumed to be produced by cell rotation only. However, axial elongation in cell walls was also observed during experiments which has not been accounted for. Incorporating this effect would enhance deformation predictions.

- Poisson's ratio was also not captured by the deformation mechanisms. Assuming unit cell deformations due entirely to rotation meant that PR would always have a value of *-1*. This assumption was not fully accurate as experimental v_T for 20DR was around *-1.5* and for 40DR was around *-2*. The rotation analogy is still a good one as clear cell rotation was observed in the experimental videos. Perhaps, an elliptical rotation model with incorporated plastic axial would be more appropriate. This requires further work.

- The strength model predicts strengths reasonably well. Assumptions regarding plastic hinging, axial load-moment interaction, and progression of failure in primary and secondary hinges are reasonable. However, everything can be related back to the empirical calibration of hinge rotation. Further work is required to construct a more robust model.

- **Table 5-4:** Inputs and Results of Macromechanical Tensile Strength Analysis.

	Base Material	**Steel**			**Aluminum**		
	Specimen	**0DR-S**	**20DR-S-1**	**40DR-S**	**0DR-A**	**20DR-A**	**40DR-A**
Material and Geometric Properties	DR	0%	20%	40%	0%	20%	40%
	L (mm)	-	33.0	34.3	-	32.5	33.8
	α (deg.)	-	9.1	16.7	-	9.1	16.7
	t_w (mm)		4.4			5.2	
	w_r (mm)	2.3	4.2	4.8	2.5	4.2	4.9
	σ_y (MPa)		438.8		117.9	157.2	
	E (GPa)		200			57.2	
	σ_u (MPa)		567.6		131.9	175.8	
	γ (kg/m^3)		7850			2720	
Experimental and Predicted Results	**Rotations at Tensile Rupture**						
	θ_c (deg.).Eq. (16)	-	1.56	3.36	-	1.54	3.39
	θ_c^{exp} (deg.) Table 3-1	-	2.49	3.57	-	0.97	2.89
	θ_c/θ_c^{exp}	-	0.63	0.94	-	1.59	1.17
	Axial strain at Peak Tensile Load						
	ε (%) Eq. (9)	-	0.40	1.58	-	0.40	1.60
	ε_a (%) Table 3-1	-	0.90	1.82	-	1.27	1.74
	$\varepsilon/\varepsilon_a$	-	0.44	0.87	-	0.31	0.92
	Peak Tensile Load						
	T (kN) Eq. (8) for auxetic	-	81.2	68.6	-	31.5	27.7
	T (kN) Eq. (14) for non-auxetic	70.0	-	-	20.1	-	-
	T^{exp} (kN)	75.2	100.2	78.0	21.2	32.0	32.2
	T/T^{exp}	0.93	0.81	0.88	0.95	0.98	0.86

5.6.3 Conclusions from Results

The results from the FE analysis demonstrated that this numerical analysis procedure can accurately predict mechanical properties of ductile metal tubes with reasonable accuracy, given that empirical modifications to strengths are applied. FE models were able to demonstrate similar Tube Poisson's Ratio v_T behavior as well as similar plasticity to experimental specimens. The FE models estimated tube strengths with reasonable accuracy; tensile and compressive strengths were predicted within *23%* and *16%* of the actual results. This shows that FE analysis can be utilized as a design tool to predict material strength, plastic response as well as Poisson's ratio behavior. FE models can be further refined to include material failure as well as damage due to cycling at plastic strains to get higher accuracy.

The derived strength equations also predicted failure loads within an error of *19%*. The model could be employed as simplified design tool to predict strength based on the base material characteristics and geometrical parameters of tubes including the DR value.

Chapter 6. Summary and Conclusions

6.1. Summary

An experimental and numerical study was undertaken to explore the effects of auxetic (NPR) behavior on load-deformation characteristics, deformed shape and energy absorbing capability in ductile metal tubes. The objective of the research was to identify what performance enhancements in auxetic behavior could be obtained if the base material is permitted to yield and undergo plastic deformations.

A total of eight specimens were manufactured, compositing five steel and three aluminum. Specimens consisting of three different geometric configurations were designed and manufactured via a 6-axis laser cutting process. A custom-made test assembly was manufactured for experimental testing. With one exception, a reverse-cyclic loading protocol was employed in experimental tests. Digital Image Correlation (DIC) was used to acquire experimental strain data. The force-deformation characteristics and Poisson's ratio behavior of tested specimens was discussed. The effect of base metal yielding on auxeticity was studied by comparing pre- and post-yield Tube Poisson's Ratio. A direct comparison of observed deformed shapes under axial loading was conducted to study the effect of increasing Deformation Ratio (DR) for each base metal. The trend in specific energy absorption due to the change in DR was discussed quantitatively for each base metal.

Finite element modeling of the tubes was performed to analyze the deformation and strength characteristics of auxetic and non-auxetic topologies. The models were subjected to the same loading protocols as the experimental tests. Experimental boundary conditions were replicated in the FE analyses to conduct a direct comparison between results. Load-deformation and Poisson's ratio behavior was extracted from the FE analysis. In addition to the high-fidelity FE models, simple macromechanical expressions were derived using equal energy principles to predict peak tensile strengths of auxetic and non-auxetic topologies. Predicted results obtained from the FE analyses and macromechanical strength models were compared against experimental data to evaluate the accuracy of the numerical procedures in describe global structural behavior of the tubes.

6.2. Conclusions

The following conclusions can be derived from the literature review, experimental data and numerical analysis presented in this thesis:

- Auxeticity can be induced in ductile metal tubes by cutting voids with a specific geometry that causes deformations in the circumferential direction. This specific cell geometry was derived based on the deformed shape of circular voids in an initial design tube. The degree of auxeticity was found to be highly-dependent on cellular geometry, quantified by a parameter defined as Deformation Ratio (DR) in this thesis.

- Deformed shapes for auxetic tubes were more stable than the tested non-auxetic tubes with circular voids. Local instability was observed in non-auxetic tested specimens. In contrast, stable, uniformly distributed radial deformations were observed in the auxetic specimens. Stability was observed to be dependent on DR value; specimens with higher DR vales demonstrated more geometrically stable deformed shapes. Global response of the auxetic tubes generated a reactive hoop stress in the tube which led to additional stability and uniformly distributed plasticity.

- Total energy absorption for the same cell geometry was dependent on base material properties. Steel specimens had superior total energy absorption to the aluminum specimens due to their superior material properties.

- A significant improvement in aerial specific energy absorption (ASEA) was caused by the auxetic geometry of cells with increase in DR linked to higher ASEA values. The deformation mechanism produced by the auxetic geometries was such that it caused a greater fraction of the tube to behave inelastically. This uniformly, widespread plasticity led to greater energy absorption despite using the same amount of base material. This implies that auxetic geometries can be optimized to maximize energy absorbing potential for a given material.

- Enhanced energy absorption is not directly caused by the NPR phenomenon, rather, the auxetic pattern used induce a more stable, uniform deformation mechanism with a

homogeneous distribution of strains in the structure which led to greater energy absorption. Auxetic specimens are stable over a greater strain range.

- In general, the results demonstrate that the introduction of an auxetic topology to ductile metal tubes through a rotated collapsed cell geometry can be beneficial for improving the effective strain range while maintaining the geometry of the structure. Furthermore, strength of the auxetic tubes increased with the use of metals with superior mechanical properties.

- Deformations in ductile metal auxetic tubes can be tuned by varying the DR of the topology. As enhanced ductility is also a factor in the total energy absorbing capacity of a structural elements, the design of ductile metal auxetic elements can potentially be tailored for such applications.FE models can accurately predict stiffness, strength, instability and deformed shape for auxetic and non-auxetic metal tubes. Introduction of damage and failure in FE models can lead to further accurate prediction of material behavior. Therefore, FE models can be employed as design and analysis tools capable of predicting behavior in the elastic and plastic domain. Deformation response and auxetic effect can also be reproduced accurately with the FE models.

- Simplistic strength equations based on equilibrium are reasonably accurate and can be employed as basic design tools to predict design strength based on cell geometry and empirical strain values.

- Existing literature is limited when it comes to structural applications of three-dimensional metallic auxetic cellular solids due to difficulty in large-scale manufacturing. Laser cutting is a proven, cost-effective process to manufacture and subsequently test metal auxetics on a large scale with an aim to gather experimental data.

6.3. Recommendations for Future Research

Based on the conducted research presented, knowledge of the following areas can be expanded:

- Studying the effect of a change in porosity by varying cell number and size. Observe changes in strength, Poisson's ratio and energy absorption for a given DR value in metal auxetic tubes.
- Experimental investigation of other non-auxetic tubular structures, such as solid tubes, to objectively quantify the differences in the mechanical characteristics and energy-absorbing capability of non-auxetic and auxetic structures.
- Investigating the effect of tube thickness on material behavior in metal auxetic tubes.
- Refining FE models to include material damage and failure to replicate experimental results.
- Conducting parametric analysis to optimize tube topology and geometry for maximizing energy absorption and global auxetic behavior.
- Study the effect of using metallic foams as filler material on energy absorbing capability of metal tubes.
- Further research into impact and high strain-rate response of ductile metal auxetics.
- Further research into the effect of monotonic loading protocol on auxetic response.
- Investigation of increased shear-resistance in metal auxetic structures.

References

(ARC), A. R. (n.d.). *ARC MISSION*. Retrieved from Advanced Research Computing: https://arc.vt.edu/about/mission/

Aalberg, A., Langseth, M., & Larsen, P. (2001). Stiffened aluminium panels subjected to axial compression. *Thin-Walled Structures, 39*(10), 861-885. doi:10.1016/s0263-8231(01)00021-0

Alderson, A. (n.d.). *Auxetic Polymeric Materials: Expanding Materials and Applications.* Retrieved from Institute of Materials, Minerals and Mining: https://www.iom3.org/sites/default/files/news-documents/alderson.pdf

Alderson, A., & Evans, K. E. (1995). Microstructural modelling of auxetic microporous polymers. *Journal of Materials Science, 30*(13), 3319-3332. doi:10.1007/bf00349875

Alderson, A., Alderson, K., Attard, D., Evans, K., Gatt, R., Grima, J., & Zied, K. (2010). Elastic constants of 3-, 4- and 6-connected chiral and anti-chiral honeycombs subject to uniaxial in-plane loading. *Composites Science and Technology, 70*(7), 1042-1048. doi:10.1016/j.compscitech.2009.07.009

Alderson, A., Alderson, K., Chirima, G., Ravirala, N., & Zied, K. (2010). The in-plane linear elastic constants and out-of-plane bending of 3-coordinated ligament and cylinder-ligament honeycombs. *Composites Science and Technology, 70*(7), 1034-1041. doi:10.1016/j.compscitech.2009.07.010

Alderson, A., Rasburn, J., & Evans, K. E. (2007). Mass transport properties of auxetic (negative Poisson's ratio) foams. *physica status solidi (b), 244*(3), 817-827. doi:10.1002/pssb.200572701

Alderson, K. L., & Evans, K. E. (1993). Strain-dependent behaviour of microporous polyethylene with a negative Poisson's ratio. *Journal of Materials Science, 28*(15), 4092-4098. doi:10.1007/bf00351238

Alderson, K., Pickles, A., Neale, P., & Evans, K. (1994). Auxetic polyethylene: The effect of a negative Poisson's ratio on hardness. *Acta Metallurgica et Materialia, 42*(7), 2261-2266. doi:10.1016/0956-7151(94)90304-2

Almgren, R. F. (1985). An isotropic three-dimensional structure with Poisson's ratio = -1. *Journal of Elasticity, 15*(4), 427-430. doi:10.1007/bf00042531

Applied Technology Council. (1992). *ATC-24. Guidelines for cyclic seismic testing of components of steel structures for buildings.* Redwood City, CA: Applied Technology Council.

ARAMIS. (2019). *Standard Operating Manual of ARAMIS Professional*. Retrieved from https://www.gom.com/3d-software/gom-system-software/aramis-professional.html

Araújo, D., Carpio, F., Méndez, D., García, A., Villar, M., García, R., & Rubio, L. (2003). Microstructural study of CO2 laser machined heat affected zone of 2024 aluminum alloy. *Applied Surface Science, 208-209*, 210-217. doi:10.1016/s0169-4332(02)01375-2

ASME. (2019). BPVC Section VIII-Rules for Construction of Pressure Vessels Division 2-Alternative Rules. *BPVC-VIII-2 - 2019.* ASME. Retrieved from https://www.asme.org/codes-standards/find-codes-standards/bpvc-viii-2-bpvc-section-viii-rules-construction-pressure-vessels-division-2-alternative-rules

ASTM Int'l. (2016). Standard Test Methods for Tension Testing of Metallic Materials. *Designation: E8/E8M − 16a*. doi:10.1520/E0008_E0008M-16A.

ASTM Int'l. (2017). Standard Test Method for Poisson's Ratio at Room Temperature. *Designation: E132 − 17*. ASTM Int'l.

ASTM Int'l. (2019). Standard Specification for Carbon Structural Steel. *Designation: A36/A36M − 19*.

Baughman, R. H., Shacklette, J. M., Zakhidov, A. A., & Stafström, S. (1998). Negative Poisson's ratios as a common feature of cubic metals. *Nature, 392*(6674), 362-365. doi:10.1038/32842

Bertoldi, K., Boyce, M., Deschanel, S., Prange, S., & Mullin, T. (2008). Mechanics of deformation-triggered pattern transformations and superelastic behavior in periodic elastomeric structures. *Journal of the Mechanics and Physics of Solids, 56*(8), 2642-2668. doi:10.1016/j.jmps.2008.03.006

Bertoldi, K., Reis, P. M., Willshaw, S., & Mullin, T. (2010). Negative Poisson's Ratio Behavior Induced by an Elastic Instability. *Advanced Materials, 22*(3), 361-366. doi:10.1002/adma.200901956

Broeren, F. G., Van der Wijk, V., & Herder, J. L. (2019). Spatial pseudo-rigid body model for the analysis of a tubular mechanical metamaterial. *Mathematics and Mechanics of Solids, 25*(2), 305-316. doi:10.1177/1081286519875500

Bruggi, M., Zega, V., & Corigliano, A. (2016). Synthesis of auxetic structures using optimization of compliant mechanisms and a micropolar material model. *Structural and Multidisciplinary Optimization, 55*(1), 1-12. doi:10.1007/s00158-016-1589-9

Caddock, B. D., & Evans, K. E. (1989). Microporous materials with negative Poisson's ratios. I. Microstructure and mechanical properties. *Journal of Physics D: Applied Physics, 22*(12), 1877-1882. doi:10.1088/0022-3727/22/12/012

Carta, G., Brun, M., & Baldi , A. (2016). Design of a porous material with isotropic negative Poisson’s ratio. *Mechanics of Materials, 97*, 67-75. doi:10.1016/j.mechmat.2016.02.012

Chakrabarty, J. (2012). *Theory of plasticity.* Elsevier. doi:https://doi.org/10.1002/crat.2170240705

Chan, N., & Evans, K. E. (1998). Indentation Resilience of Conventional and Auxetic Foams. *Journal of Cellular Plastics, 34*(3), 231-260. doi:10.1177/0021955x9803400304

Chen, Y., Scarpa, F., Liu, Y., & Leng, J. (2013). Elasticity of anti-tetrachiral anisotropic lattices. *International Journal of Solids and Structures, 50*(6), 996-1004. doi:10.1016/j.ijsolstr.2012.12.004

Chetcuti, E., Ellul, B., Manicaro, E., Brincat, J., Attard, D., Gatt, R., & Grima, J. N. (2014). Modeling auxetic foams through semi-rigid rotating triangles. *physica status solidi (b), 251*(2), 297-306. doi:10.1002/pssb.201384252

Choi, J. B., & Lakes, R. S. (1992). Non-linear properties of metallic cellular materials with a negative Poisson's ratio2. *Journal of Materials Science, 27*(19), 5375-5381. doi:10.1007/bf02403846

Choi, J. B., & Lakes, R. S. (1992). Non-linear properties of polymer cellular materials with a negative Poisson's ratio. *Journal of Materials Science, 27*(17), 4678-4684. doi:10.1007/bf01166005

Choi, J. B., & Lakes, R. S. (1995). Analysis of elastic modulus of conventional foams and of re-entrant foam materials with a negative Poisson's ratio. *International Journal of Mechanical Sciences, 37*(1), 51-59. doi:10.1016/0020-7403(94)00047-n

De Lima, C. R., & Paulino, G. H. (2019). Auxetic structure design using compliant mechanisms: A topology optimization approach with polygonal finite elements. *Advances in Engineering Software, 129*, 69-80. doi:10.1016/j.advengsoft.2018.12.002

DIN. (2005). Hot rolled products of structural steels - Part 2: Technical delivery conditions for non-alloy structural steels. *DIN EN 10025-2*.

DIN. (2016). DIN EN 755-2. *Aluminium and aluminium alloys - Extruded rod/bar, tube and profiles - Part 2: Mechanical properties*.

Dirrenberger, J., Forest, S., & Jeulin, D. (2012). Effective elastic properties of auxetic microstructures: anisotropy and structural applications. *International Journal of Mechanics and Materials in Design, 9*(1), 21-33. doi:10.1007/s10999-012-9192-8

Dirrenberger, J., Forest, S., & Jeulin, D. (2012). Elastoplasticity of auxetic materials. *Computational Materials Science, 64*, 57-61. doi:10.1016/j.commatsci.2012.03.036

Dvorkin, E. N., & Bathe, K. (1984). A continuum mechanics based four-node shell element for general non-linear analysis. *Engineering Computations, 1*(1), 77-88. doi:10.1108/eb023562

Eiroa, D. S. (2015). *Characterisation of laser cutting process for materials used in aerospace industry.* MS Thesis, Cranfield University, School of Aerospace, Transport And Manufacturing. doi:10.13140/RG.2.2.33560.80641

Evans, K. E. (1991). Auxetic polymers: a new range of materials. *Endeavour, 15*(4), 170-174. doi:10.1016/0160-9327(91)90123-s

Evans, K. E., & Alderson , A. (2000, April 17). Auxetic Materials: Functional Materials and Structures from Lateral Thinking! *Advanced Materials, 12*(9), 617-628. doi:https://doi.org/10.1002/(SICI)1521-4095(200005)12:9<617::AID-ADMA617>3.0.CO;2-3

Evans, K. E., Nkansah, M. A., Hutchinson, I. J., & Rogers, S. C. (1991). Molecular Network Design. *Nature, 353*(6340), 124-125. doi:10.1038/353124a0

Farzampour, A., & Eatherton, M. R. (2019). Parametric computational study on butterfly-shaped hysteretic dampers. *Frontiers of Structural and Civil Engineering, 13*(5), 1214-1226. doi:10.1007/s11709-019-0550-6

FEMA. (2007). Interim Testing Protocols for Determining the Seismic Performance Characteristics of Structural and Nonstructural Components. *FEMA 461*. Federal Emergency Management Agency. Retrieved from https://www.fema.gov/media-library-data/20130726-1646-20490-4313/fema461.pdf

Fintel, M., & Ghosh, S. K. (1981). The Structural Fuse: An Inelastic Approach to Earthquake-Resistant Design of Buildings. *Civil Engineering—ASCE, 51*(1), 48-51.

Friis, E. A., Lakes, R. S., & Park, J. B. (1988). Negative Poisson's ratio polymeric and metallic foams. *Journal of Materials Science, 23*(12), 4406-4414. doi:10.1007/bf00551939

Fung, Y. (1965). *Foundations of solid mechanics.* Prentice Hall.

Gaspar, N., Ren, X., Smith, C., Grima, J., & Evans, K. (2005). Novel honeycombs with auxetic behaviour. *Acta Materialia, 53*(8), 2439-2445. doi:10.1016/j.actamat.2005.02.006

Gatt, R., Attard, D., Farrugia, P., Azzopardi, K. M., Mizzi, L., Brincat, J., & Grima, J. N. (2013). A realistic generic model for anti-tetrachiral systems. *physica status solidi (b), 250*(10), 2012-2019. doi:10.1002/pssb.201384246

Gatt, R., Caruana-Gauci, R., Attard, D., Casha , A. R., Wolak, W., Dudek, K., . . . Grima, J. N. (2014). On the properties of real finite-sized planar and tubular stent-like auxetic structures. *physica status solidi (b), 251*(2), 321-327. doi:10.1002/pssb.201384257

Ghaedizadeh, A., Shen, J., Ren, X., & Xie, Y. (2016). Tuning the Performance of Metallic Auxetic Metamaterials by Using Buckling and Plasticity. *Materials, 9*(1), 54. doi:10.3390/ma9010054

Gibson, L. J., & Ashby, M. F. (1999). *Cellular Solids: Structure and Properties.* England: Cambridge University Press.

GOM. (n.d.). *ARAMIS Adjustable*. Retrieved from https://www.gom.com/metrology-systems/aramis/aramis-adjustable.html

Grima , J. N., & Evans, K. E. (2006). Auxetic behavior from rotating triangles. *Journal of Materials Science, 41*(10), 3193-3196. doi:10.1007/s10853-006-6339-8

Grima , J. N., Chetcuti, E., Manicaro, E., Attard, D., Camilleri, M., Gatt, R., & Evans, K. E. (2011). On the auxetic properties of generic rotating rigid triangles. *Proceedings of the Royal Society A: Mathematical, Physical and Engineering Sciences, 468*(2139), 810-830. doi:10.1098/rspa.2011.0273

Grima, J. N., & Evans, K. E. (2000). Auxetic behavior from rotating squares. *Journal of Material Science Letters, 19*(17), 1563–1565. doi:10.1023/A:1006781224002

Grima, J. N., & Gatt, R. (2010). Perforated Sheets Exhibiting Negative Poisson's Ratios. *Advanced Engineering Materials, 12*(6), 460-464. doi:10.1002/adem.201000005

Grima, J. N., Alderson, A., & Evans, K. E. (2004). Negative Poisson's Ratios From Rotating Rectangles. *Computational Methods in Science and Technology, 10*(2), 137-145. doi:10.12921/cmst.2004.10.02.137-145

Grima, J. N., Farrugia, P., Gatt, R., & Attard, D. (2008). On the auxetic properties of rotating rhombi and parallelograms: A preliminary investigation. *physica status solidi (b), 245*(3), 521-529. doi:10.1002/pssb.200777705

Grima, J. N., Gatt, R., & Farrugia, P. (2008). On the properties of auxetic meta-tetrachiral structures. *physica status solidi (b), 245*(3), 511-520. doi:10.1002/pssb.200777704

Grima, J. N., Gatt, R., Ellul, B., & Chetcuti, E. (2010). Auxetic behaviour in non-crystalline materials having star or triangular shaped perforations. *Journal of Non-Crystalline Solids, 356*(37-40), 1980-1987. doi:10.1016/j.jnoncrysol.2010.05.074

Grima, J. N., Manicaro, E., & Attard, D. (2010). Auxetic behaviour from connected different-sized squares and rectangles. *Proceedings of the Royal Society A: Mathematical, Physical and Engineering Sciences, 467*(2126), 439-458. doi:10.1098/rspa.2010.0171

Grima, J. N., Zammit, V., Gatt, R., Alderson, A., & Evans, K. E. (2007). Auxetic behaviour from rotating semi-rigid units. *physica status solidi (b), 244*(3), 866-882. doi:10.1002/pssb.200572706

Hamming, R. (2012). *Numerical methods for scientists and engineers.* Courier Corporation.

Imbalzano, G., Linforth, S., Ngo, T. D., Lee, P. V., & Tran, P. (2018). Blast resistance of auxetic and honeycomb sandwich panels: Comparisons and parametric designs. *Composite Structures*, 242-261. doi:10.1016/j.compstruct.2017.03.018

Imblazano, G., Tran, P., Ngo, T. D., & Lee, P. V. (2016). A numerical study of auxetic composite panels under blast loadings. *Composite Structures, 135*, 339-352. doi:10.1016/j.compstruct.2015.09.038

Ingrole, A., Hao, A., & Liang, R. (2017). Design and modeling of auxetic and hybrid honeycomb structures for in-plane property enhancement. *Materials & Design, 117*, 72-83. doi:10.1016/j.matdes.2016.12.067

Jiang, Y., & Kurath, P. (1996). Characteristics of the Armstrong-Frederick type plasticity models. *International Journal of Plasticity, 12*(3), 387-415. doi:10.1016/s0749-6419(96)00013-7

Kaminakis, N. T., & Stavroulakis, G. E. (2012). Topology optimization for compliant mechanisms, using evolutionary-hybrid algorithms and application to the design of auxetic materials. *Composites Part B: Engineering, 43*(6), 2655-2668. doi:10.1016/j.compositesb.2012.03.018

Karnessis , N., & Burriesci, G. (2013). Uniaxial and buckling mechanical response of auxetic cellular tubes. *Smart Materials and Structures, 22*(8), 084008. doi:10.1088/0964-1726/22/8/084008

Khatib, I. F., Mahin, S. A., & Pister, K. S. (1988). *Seismic Behavior of Concentrically Braced Steel Frames.* Washington, DC: National Science Foundation. Retrieved from https://nehrpsearch.nist.gov/article/PB91-210898/XAB

Kim, K., & Ju, J. (2015). Mechanical metamaterials with 3D compliant porous structures. *Composite Structures, 132*, 874-884. doi:10.1016/j.compstruct.2015.06.060

Kshetrimayum, R. (2005). A brief intro to metamaterials. *IEEE Potentials, 23*(5), 44-46. doi:10.1109/mp.2005.1368916

Lakes , R. E., & Elms, K. (1993). Indentability of Conventional and Negative Poisson's Ratio Foams. *Journal of Composite Materials, 27*(12), 1193-1202. doi:10.1177/002199839302701203

Lakes, R. (1987, Feb 27). "Foam Structures with a Negative Poisson's Ratio". *Science, 235*(4792), 1038-1040. doi:10.1126/science.235.4792.1038

Lakes, R. (1987). Foam Structures with a Negative Poisson's Ratio. *Science, 235*(4792), 1038-1040. doi:10.1126/science.235.4792.1038

Lakes, R. (1991). Deformation mechanisms in negative Poisson's ratio materials: structural aspects. *Journal of Materials Science, 26*(9), 2287-2292. doi:10.1007/bf01130170

Lee, W., Jeong, Y., Yoo, J., Huh, H., Park, S., Park, S. H., & Yoon, J. (2019). Effect of auxetic structures on crash behavior of cylindrical tube. *Composite Structures, 208*, 836-846. doi:10.1016/j.compstruct.2018.10.068

Lees, C., Vincent, J. F., & Hillerton, E. (1991). Poisson's ratio in skin. *Bio-Medical Materials and Engineering, 1*(1), 19-23. Retrieved from https://www.ncbi.nlm.nih.gov/pubmed/1842507

Li, Y. (1976). The anisotropic behavior of Poisson's ratio, Young's modulus, and shear modulus in hexagonal materials. *Physica Status Solidi (a), 38*(1), 171-175. doi:10.1002/pssa.2210380119

Lim, T. C., Alderson, A., & Alserson, K. L. (2013). Experimental studies on the impact properties of auxetic materials. *physica status solidi (b), 251*(2), 307-313. doi:10.1002/pssb.201384249

Liu, W., Wang, N., Luo, T., & Lin, Z. (2016). In-plane dynamic crushing of re-entrant auxetic cellular structure. *Materials & Design, 100*, 84-91. doi:10.1016/j.matdes.2016.03.086

Livermore Software Technology. (2002). *LS-PRE/POST v1.0 manual*. Retrieved from LS-DYNA Support: https://www.dynasupport.com/manuals/additional/ls-pre-post-v1.0-manual

Livermore Software Technology Corporation (LSTC). (2018, October). *LS-DYNA® Keyword User's Manual*. Retrieved from LS-Dyna Support: https://www.dynasupport.com/manuals/ls-dyna-manuals/ls-dyna_manual_volume_i_r11.pdf

Love, A. E. (1944). *A Treatise on the Mathematical Theory of Elasticity.* New York: Dover Publications.

Lu, S. (2017). *Performance-based design prodedure for a novel semi-active cladding connection applied to blast mitigation.* Graduate Thesis, Iowa State University. Retrieved from https://lib.dr.iastate.edu/etd/16171

Malakoutian, M., Berman, J. W., & Dusicka, P. (2012). Seismic response evaluation of the linked column frame system. *Earthquake Engineering & Structural Dynamics, 42*(6), 795-814. doi:10.1002/eqe.2245

Masters, I., & Evans, K. (1996). Models for the elastic deformation of honeycombs. *Composite Structures, 35*(4), 403-422. doi:10.1016/s0263-8223(96)00054-2

Mizzi, L., Azzopardi, K. M., Attard, D., Grima, J. N., & Gatt, R. (2015). Auxetic metamaterials exhibiting giant negative Poisson's ratios. *physica status solidi (RRL) - Rapid Research Letters, 9*(7), 425-430. doi:10.1002/pssr.201510178

MTS. (n.d.). TestWorks®. Retrieved from https://www.mts.com/cs/groups/public/documents/library/dev_002046.pdf

Nazemi, N., & Ghrib, F. (2019). Strength characteristics of heat-affected zones in welded aluminum connections. *Journal of Engineering Mechanics, 145*(12), 04019103. doi:10.1061/(asce)em.1943-7889.0001647

Neale, P. J., Alderson, K. L., Pickles, A. P., & Evans, K. E. (1993). Negative Poisson's ratio of microporous polyethylene in compression. *JOURNAL OF MATERIALS SCIENCE LETTERS, 12*(19), 1529-1532. doi:10.1007/BF00277087

Perry, J., Perl, M., Schneck , R., & Haroush, S. (2005). The Influence of the Bauschinger Effect on the Yield Stress, Young’s Modulus, and Poisson’s Ratio of a Gun Barrel Steel. *Journal of Pressure Vessel Technology, 128*(2), 179-184. doi:10.1115/1.2172962

Philips, A. R., & Eatherton, M. R. (2018). Large-scale experimental study of ring shaped–steel plate shear walls. *Journal of Structural Engineering, 144*(8), 04018106. doi:10.1061/(asce)st.1943-541x.0002119

Popov, E. P., & Engelhardt, M. D. (1988). Seismic eccentrically braced frames. *Journal of Constructional Steel Research, 10*, 321-354. doi:10.1016/0143-974x(88)90034-x

Pozniak, A. A., & Wojciechowski, K. W. (2014). Poisson's ratio of rectangular anti-chiral structures with size dispersion of circular nodes. *physica status solidi (b), 251*(2), 367-374. doi:10.1002/pssb.201384256

Prall, D., & Lakes, R. (1997). Properties of a chiral honeycomb with a poisson's ratio of — 1. *International Journal of Mechanical Sciences, 39*(3), 10.1016/s0020-7403(96)00025-2. doi:10.1016/s0020-7403(96)00025-2

Qi, C., Remennikov, A., Pei, L., Yang, S., Yu, Z., & Ngo, D. T. (2017). Impact and close-in blast response of auxetic honeycomb-cored sandwich panels: Experimental tests and numerical simulations. *Composite Structures, 180,* 161-178. doi:10.1016/j.compstruct.2017.08.020

Rasburn, J., Mullarkey, P. G., Evans, K. E., Alderson, A., Ameer-Beg, S., & Perrie, W. (2001). Auxetic structures for variable permeability systems. *AIChE Journal, 47*(11), 2623-2626. doi:10.1002/aic.690471125

Ren, X., Das, R., Tran, P., Ngo, T. D., & Xie, Y. M. (2018). Auxetic metamaterials and structures: a review. *Smart Materials and Structures, 27*(2), 023001. doi:10.1088/1361-665x/aaa61c

Ren, X., Shen, J., Ghaedizadeh, A., Tian, H., & Min Xie, Y. (2015). Experiments and parametric studies on 3D metallic auxetic metamaterials with tuneable mechanical properties. *Smart Materials and Structures, 24*(9), 095016. doi:10.1088/0964-1726/24/9/095016

Ren, X., Shen, J., Ghaedizadeh, A., Tian, H., & Xie, Y. M. (2016). A simple auxetic tubular structure with tuneable mechanical properties. *Smart Materials and Structures, 25*(6), 065012. doi:10.1088/0964-1726/25/6/065012

Roberts, T. M. (1995). Seismic resistance of steel plate shear walls. *Engineering Structures, 17*(5), 344-351. doi:10.1016/0141-0296(95)00017-2

Scarpa, F., Smith, C. W., Ruzzene, M., & Wadee, M. K. (2008). Mechanical properties of auxetic tubular truss-like structures. *physica status solidi (b), 245*(3), 584-590. doi:10.1002/pssb.200777715

Schwerdtfeger, J., Heinl, P., Singer, R. F., & Körner, C. (2010). Auxetic cellular structures through selective electron-beam melting. *physica status solidi (b), 247*(2), 269-272. doi:10.1002/pssb.200945513

Schwerdtfeger, J., Schury, F., Stingl, M., Wein, F., Singer, R. F., & Körner, C. (2011). Mechanical characterisation of a periodic auxetic structure produced by SEBM. *physica status solidi (b), 249*(7), 1347-1352. doi:10.1002/pssb.201084211

Shandookh, A. (2018). Comparison Between Metal Cutting Types and its Effects on Mechanical. *Bilad Alrafidain University College 2nd Scientific Conference 2017.*

Shoeibi, S., Kafi, M. A., & Gholhaki, M. (2017). New performance-based seismic design method for structures with structural fuse system. *Engineering Structures, 132*, 745-760. doi:10.1016/j.engstruct.2016.12.002

Smith, C., Grima, J., & Evans, K. (2000). A novel mechanism for generating auxetic behaviour in reticulated foams: missing rib foam model. *Acta Materialia, 48*(17), 4349-4356. doi:10.1016/s1359-6454(00)00269-x

Spadoni, A., & Ruzzene, M. (2012). Elasto-static micropolar behavior of a chiral auxetic lattice. *Journal of the Mechanics and Physics of Solids, 60*(1), 156-171. doi:10.1016/j.jmps.2011.09.012

Stathers, P. A., Hellier, A. K., Harrison, R. P., Ripley, M. I., & Norrish, J. (2014). Hardness-tensile property relationships for HAZ in 6061-T651 aluminum. *Welding Journal, 93*(8), 301-311. Retrieved from https://ro.uow.edu.au/eispapers/2846/

Stournaras, A., Stavropoulos, P., Salonitis, K., & Chryssolouris, G. (2009). An investigation of quality in CO2 laser cutting of aluminum. *CIRP Journal of Manufacturing Science and Technology, 2*(1), 61-69. doi:10.1016/j.cirpj.2009.08.005

Taylor, M., Francesconi, L., Gerendás, M., Shanian, A., Carson, C., & Bertoldi, K. (2013). Low Porosity Metallic Periodic Structures with Negative Poisson's Ratio. *Advanced Materials, 26*(15), 2365-2370. doi:10.1002/adma.201304464

Tehranizadeh, M. (2001). Passive energy dissipation device for typical steel frame building in Iran. *Engineering Structures, 23*(6), 643-655. doi:10.1016/s0141-0296(00)00082-1

Timoshenko, S. P., & Gere, J. M. (1961). *Theory of elastic stability, 2nd Edition.* New York: McGraw-Hill.

Veronda, D., & Westmann, R. (1970). Mechanical characterization of skin—Finite deformations. *Journal of Biomechanics, 3*(1), 111-124. doi:10.1016/0021-9290(70)90055-2

Voigt, W. (1882). Allgemeine Formeln für die Bestimmung der Elasticitätsconstanten von Krystallen durch die Beobachtung der Biegung und Drillung von Prismen. *Annalen der Physik, 252*(6), 273-321. doi:10.1002/andp.18822520607

Wang, Y., Shen, M., & Liao, S. (2017). Microstructural Effects on the Poisson's Ratio of Star-Shaped Two-Dimensional Systems. *physica status solidi (b), 254*(12), 1770264. doi:10.1002/pssb.201770264

Williams, J. L., & Lewis, J. L. (1982). Properties and an Anisotropic Model of Cancellous Bone From the Proximal Tibial Epiphysis. *Journal of Biomechanical Engineering, 104*(1), 50-56. doi:10.1115/1.3138303

Yang, C., Vora, H. D., & Chang, Y. (2018). Behavior of auxetic structures under compression and impact forces. *Smart Materials and Structures, 27*(2), 025012. doi:10.1088/1361-665x/aaa3cf

Yang, L., Harrysson, O., West , H., & Cormier, D. (2015). Mechanical properties of 3D re-entrant honeycomb auxetic structures realized via additive manufacturing. *International Journal of Solids and Structures, 69-70,* 475-490. doi:10.1016/j.ijsolstr.2015.05.005

Yang, L., Harrysson, O., West, H., & Cormier, D. (2012). Compressive properties of Ti–6Al–4V auxetic mesh structures made by electron beam melting. *Acta Materialia, 60*(8), 3370-3379. doi:10.1016/j.actamat.2012.03.015

Yang, L., Harrysson, O., West, H., & Cormier, D. (2012). Compressive properties of Ti–6Al–4V auxetic mesh structures made by electron beam melting. *Acta Materialia, 60*(8), 3370-3379. doi:10.1016/j.actamat.2012.03.015

Yang, L., Harrysson, O., West, H., & Cormier, D. (2013). A Comparison of Bending Properties for Cellular Core Sandwich Panels. *Materials Sciences and Applications, 4*(8), 471-477. doi:10.4236/msa.2013.48057

Yang, S., Qi, C., Wang, D., Gao, R., Hu, H., & Shu, J. (2013). A Comparative Study of Ballistic Resistance of Sandwich Panels with Aluminum Foam and Auxetic Honeycomb Cores. *Advances in Mechanical Engineering, 5,* 589216. doi:10.1155/2013/589216

Zhang, X., & Yang, D. (2016). Mechanical Properties of Auxetic Cellular Material Consisting of Re-Entrant Hexagonal Honeycombs. *Materials, 9*(11), 900. doi:10.3390/ma9110900